Annealing for intrinsic point-defect control and enhanced solar cell performance: The case of H_2S and tin sulfide (SnS)

by

Katherine Hartman

B.S., Massachusetts Institute of Technology (2008)

Submitted to the Department of Material Science and Engineering
in partial fulfillment of the requirements for the degree of

Doctor of Philosophy

at the

MASSACHUSETTS INSTITUTE OF TECHNOLOGY

February 2015

Author ..... Signature redacted
Department of Material Science and Engineering
October 27, 2014

Certified by ..... Signature redacted
Tonio Buonassisi
Associate Professor
Thesis Supervisor

Accepted by ..... Signature redacted
Donald Sadoway
Chairman, Department Committee on Graduate Theses

Annealing for intrinsic point-defect control and enhanced solar cell performance: The case of H_2S and tin sulfide (SnS)

by

Katherine Hartman

Submitted to the Department of Materials Science and Engineering
on October 27, 2014, in partial fulfillment of the
requirements for the degree of
Doctor of Philosophy

Abstract

This thesis explores the possibility of tin monosulfide (SnS) as a new and promising solar cell absorber material. Out of many other Earth-abundant binary semiconductors, it was selected for study because it has a strong absorption coefficient, high majority carrier mobility, and a promising initial report of a 1.3 % solar cell. Tin sulfide does not have the toxicity or scarcity issues that will plague CdTe and CIGS thin film manufacturers as the PV industry grows toward the terawatt level.

Growth of SnS is explored using RF sputtering and thermal evaporation. Thermal evaporation yielded phase pure films and a SnS solar cell device stack was developed using a ZnO_xS_y film as the n-type buffer layer. It is hypothesized that annealing in H_2S/H_2 gas mixtures will improve film morphology, control majority carrier concentration and reduce sulfur vacancy mid-gap states.

Using the Kröger-Vink defect equilibria model of defect concentrations and DFT-calculated enthalpy of formations for intrinsic defects, predictions are made for how a particular anneal temperature and sulfur partial pressure will affect the carrier concentration in SnS. A custom H_2S/H_2 gas annealing furnace was built to explore the range of annealing parameters that are predicted to be promising for SnS photovoltaic development. Results have found that neither of these two models are adequate to explain the observed change in carrier concentration after annealing the thin films. However, results have shown the ability to manipulate majority carrier concentration in SnS thin films by up to 2 orders of magnitude with short (<1 hour) anneals. Certain annealing conditions are also found to greatly increase grain growth. The results of these improved annealing parameters and enlarged grains are seen in a 98.4 % relative efficiency improvement from as-deposited to annealed thermally evaporated SnS solar cells.

A new and unique experimental tool has been created and a framework established for further research of intrinsic point defects in SnS material. Research using these new tools will yield even greater efficiency increases for the Earth-abundant PV material, tin sulfide.

Thesis Supervisor: Tonio Buonassisi
Title: Associate Professor

Acknowledgments

They say "it takes a village" to raise a child, and I suspect the same is true for "raising" a graduate student. I am lucky to have "grown up" in the PV Lab village, where I have had the privilege of watching this lab grow and transform from an empty room with empty tables and empty cabinets to a packed, bustling, thriving environment with a small army of graduate students and postdocs. I have enjoyed the company of this lab over the past 7 years and know that I could not have done this research without their help.

Tonio Buonassisi: Your enthusiasm for solar is infectious and inspiring. Thank you for setting me on the solar path.

Raf Jaramillo: Your mentorship and guidance over the past 2 years has been of great help to me and a wonderful learning experience.

Jim Serdy: You've been helping me since I was a UROP student and it has been a privilege to work with you. I'm quite sure I wouldn't be writing this without your help.

The SnS team: Rupak Chakraborty, Alex Polizzotti, Vera Steinmann, Riley Brandt, Jeremy Poindexter, Jasmin Hofstetter, Niall Mangan. I've learned so much from all of you. What a great experience working as a team!

Thank you to PVLab members present: Amanda Youssef, Austin Akey, Mariela Castillo, Sergio Castellanos, Jonathan Mailoa, Mallory Jensen, Tim Kirkpatrick, Doug Powell, Hannes Wagner, Eric Johlin, Ashley Morishige, David Berney Needleman, Sin Cheng Siah, Patricia Yen, Sarah Sofia and anyone who's ever been my H_2S buddy!

Thank you to PVLab members past: Yun S. Lee, Mark Winkler, Yaron Segal, Mariana Bertoni, Bonna Newman, Christie Simmons, Joe Sullivan, David Fenning, Michael Lloyd, Max Powers, Torunn Ervik, Sebastian Castro, Michael Ising, Allyna Nguyen.

Thank you to Gordon group members: Professor Gordon, Helen H. Park, Chuanxi Yang, Leizhi Sun, Prasert Sinsermsuksakul.

Help around MIT: Kurt Broderick, Scott Speakman, Neel Chatterjee.

Help around University of Utah: Jeffery L. Johnson, Mike Scarpulla, Liz Lund, Loren Reith.

Thank you to friends: Michelle Tomasik, Alev Atalay. And during early grad school days: Sam Crawford, Johanna Engel, Rodolfo Camacho. Cheers to the awesomo crew!

Thank you to Marc for your love, support and comfort. Having you with me for the last few years has made me a better scientist. This wild ride would have been much less fun without you.

Mom and Dad: Thank you for pushing me and always believing in me.

Funding sources: Chesonis Family Foundation, Family of Doug and Barbara Spreng, U.S. Department of Energy (DOE) SunShot Initiative through the SERIIUS project and NextGen II DE-EE0005329, National Science Foundation (NSF) Graduate Research Fellowship, Intel PhD Fellowship. This work made use of the Center for Materials Science and Engineering at MIT which is supported by the NSF under award DMR-08-19762, and the Center for Nanoscale Systems at Harvard University which is supported by NSF under award ECS-0335765.

Contents

List of Figures

List of Tables

Chapter 1

Introduction

The story of how a particular material or invention becomes the incumbent technology is always an interesting one. Often, these stories of success are filled not only with many hours of hard work but also tales of great luck and happenstance. The realization of the role of luck in these dominant technologies leads to a huge "what if?"

In the case of solar photovoltaics (PV), *what if* silicon is not the best material for the job? The dominance of silicon in the photovoltaics industry is arguably fueled by huge amounts of research into silicon material, pushed by interest and profits from the integrated circuits industry. Silicon photovoltaics leans on 70 years of materials research. Likewise, CdTe and CIGS ($CuIn_xGa_{1-x}Se_2$) thin-film photovoltaics both have 30+ years of research driving their photovoltaic conversion efficiencies higher. Each of these materials has a few reasons why it makes a good solar cell, but yet each of these materials has pitfalls: reasons why they are not such a good PV material. What if there were a better PV material that we simply have not discovered yet? The number of materials that have yet to be meaningfully characterized is vast. The number grows even larger when one considers metastable materials, instead of just thermodynamically stable materials. As the field of materials science moves toward materials *design*, rather than just materials discovery, we use the application of photovoltaics as a case study. Given the current knowledge in the field of PV, how can we design and find a better PV material? What does that PV material look like

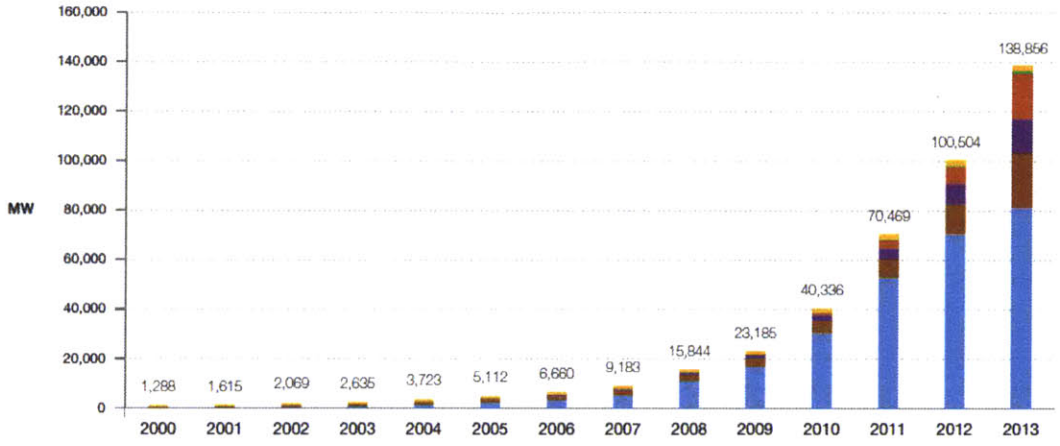

	2000	2001	2002	2003	2004	2005	2006	2007	2008	2009	2010	2011	2012	2013
RoW	751	807	887	964	993	1,003	1,108	1,150	1,226	1,306	1,590	2,098	2,098	2,098
MEA	n/a	n/a	n/a	n/a	1	1	1	2	3	25	80	205	570	953
China	19	24	42	52	62	70	80	100	140	300	800	3,300	6,800	18,600
Americas	21	24	54	102	163	246	355	522	828	1,328	2,410	4,590	8,365	13,727
APAC	368	496	686	916	1,198	1,502	1,827	2,098	2,628	3,373	4,951	7,513	12,159	21,992
Europe	129	265	399	601	1,306	2,291	3,289	5,312	11,020	16,854	30,505	52,764	70,513	81,488
Total	**1,288**	**1,615**	**2,069**	**2,635**	**3,723**	**5,112**	**6,660**	**9,183**	**15,844**	**23,185**	**40,336**	**70,469**	**100,504**	**138,856**

RoW: Rest of the World. MEA: Middle East and Africa. APAC: Asia Pacific.
Methodology used for RoW data collection has changed in 2012

Figure 1 - Evolution of global PV cumulative installed capacity 2000-2013

Figure 1-1: Cumulative Installed Global PV Capacity from 2000-2013, segregated by region of the world. Image from European Photovoltaic Industry Association, Global Market Outlook [7].

and how does it behave?

The photovoltaics industry is growing rapidly [7]. In the year 2008, when I began my thesis, the total cumulative global installed PV capacity was 15.8 GW. The most recent tally, from 2013, is a cumulative installed capacity 138.9 GW. This is almost an order of magnitude growth in just 5 years! While current silicon, CdTe and CIGS technologies are necessarily keeping pace with growth, this may not always be the case. If solar is ever to become a primary method of energy production, terawatts-worth of solar panels must be produced. The year 2013 saw 38.4 GW of new installed PV capacity [7]. In particular, CdTe and CIGS will face severe materials shortage issues and cannot be relied upon to make the jump from gigawatts to terawatts of capacity production. Silicon technology remains a good and viable

option for scale-up. However, the material does not absorb light strongly, requiring thicker absorption layers and greater materials usage than thin-film technologies. With light trapping, high quality silicon, appropriate cell architecture, and excellent surface passivation, silicon solar cells thicknesses may still need to be in the range of 20–110 μm to achieve the highest theoretical efficiencies [29, 74]. More strongly absorbing thin-film materials may only require 1–3 μm of material to achieve high efficiency. This is a 1–2 orders of magnitude reduction in materials utilization for the absorber layer.

Additionally, terawatt levels of PV production requires increasing the speed of solar cell production by several orders of magnitude. There is currently no technology or material today that can achieve this. With current silicon solar cell technology, the capital expenditure required to build a terawatt-sized silicon solar panel plant is too large to allow profitability. New research in this area is needed. If silicon solar cells cannot be manufactured rapidly and cheaply, then we must look to other materials.

1.1 Motivations for new solar cell materials

The existing commercial thin-film solar cell technologies, currently CdTe and CIGS, will likely run into serious supply issues in the near to mid-term future. Both CIGS and CdTe are limited to a total of 0.02 TWy energy production, based on known reserves of indium and tellurium, and known efficiency values [25]. Tellurium is considered a rare element and additionally, there are safety concerns when working with cadmium or cadmium containing compounds. Indium is also an extremely rare and expensive element. At the end of 2013, the average price of indium was $570-620 per kg [96]. Indium is also required as a key ingredient in transparent conducting oxides for the growing flat panel displays industry. Additionally, tellurium and indium are not elements which are directly mined. They are typically found as a by-product of copper, aluminum and zinc mining operations. As the CIGS solar panel industry grows, demand for indium will no doubt increase and one cannot hope to ever make cheap, low-cost solar cells while utilizing an element such as indium. These supply

issues will not be easily resolved. Thus, Earth-abundancy is selected as one of the primary selection criteria. This allows the potential for large scale-up to terawatt levels of production. Compared to indium in 2013, tin sold for approximately $22.23 - 29.54 per kg [96], which is an order of magnitude less than indium.

1.2 Defining Earth-abundance

Begin with the assumption that one day, all of the world's new energy capacity will come from photovoltaics. Admittedly, this assumption is strongly dependent on the development of grid-level storage. However, it is not outside the realm of possibility. With this assumption, we can calculate the area of solar panels needed to supply all of the world's growing energy capacity needs, assuming 15 % efficient panels. This efficiency value is roughly half of the theoretical efficiency limit of a single-junction solar cell with an ideal band gap value tuned to the most energy intensive area of the solar spectrum (around 1.0–1.5 eV), as seen in Fig. 1-2. 15 % is also a typical efficiency value for an average commercial crystalline silicon solar cell.

We assume the solar cell will be a thin film, not more than 2 μm thick, which is all the material one would need, assuming a direct band gap semiconductor and an absorption coefficient of $\alpha > 10^4$ cm^{-1} at the band edge. Using an average global irradiance of 200 W/m^2 and the U.S Energy Information Administration (EIA) projected world growth in energy and electricity requirements between 2009 and 2035, where an additional 10 terawatts of capacity will be needed [2], we can calculate the volume of solar cell material necessary to produce the required panel area.

Using U.S. Geological Survey data, a list of all elements with the required abundancy is compiled. The available elements are shown in the periodic table in Fig. 1-3. The elements on this list are used as a starting point for finding an Earth-abundant thin film solar cell material.

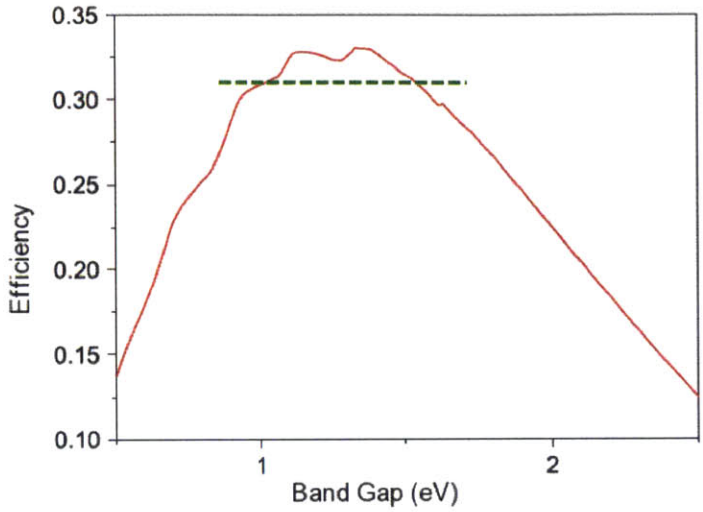

Figure 1-2: The maximum theoretical efficiency is calculated using the detailed-balance equations from Shockley and Queisser [82] and the AM1.5 solar spectrum from ASTM G173-03 Reference Spectra [23]. The green dotted line indicates a rough guideline used to focus on materials capable of higher theoretical efficiency based on their band gap. Where the green line intersects the red Shockley-Quisser efficiency line defines the bounds of interest for the band gap of a potential new solar cell material. Image modified from Siebentritt 2011 [83].

1.3 Criteria to select a new solar cell material

Outlined below are the material criteria (other than Earth-abundance) used for selecting tin sulfide as a promising single-junction solar cell material. The limitation of a single junction is made for ease and simplification of manufacturing. Fewer deposited layers means lower manufacturing and development costs. However, this limitation does not preclude a second junction from ever being developed. These criteria are the beginnings of a list that an "ideal" solar cell material might have. While this list is not complete and could be further discussed and expanded (particularly in light of the advancements in perovskite solar cells), it was used as the primary culling tool for eliminating the hundreds of possible semiconductor materials that could be made from the list of 29 elements shown in Figure 1-3.

With each criteria, the characteristics of SnS relating to this criteria is discussed.

1. Single or binary compound semiconductor.

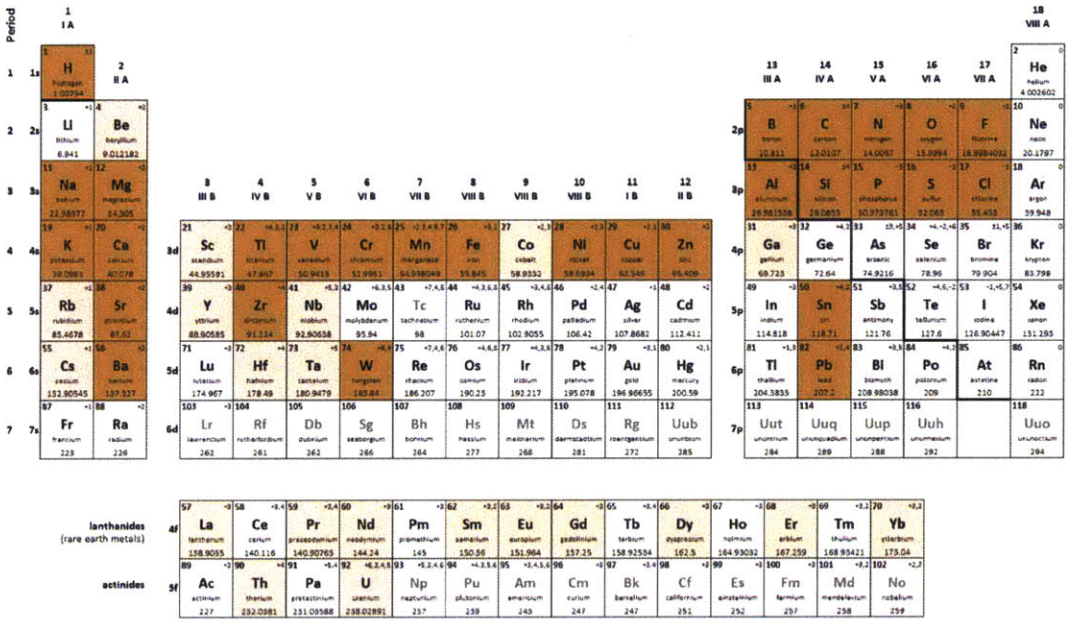

Figure 1-3: There are 50 elements with the necessary abundance to create all new solar panels from this material (marked in both light orange and dark orange) [1]. There are 29 materials with the existing manufacturing capacity that would enable rapid scale-up of solar panel production [95]. Analysis and image provided by Yun Seog Lee and Tonio Buonassisi.

Ternary and quaternary compounds, such as CIGS and CZTS (copper zinc tin sulfide, Cu_2ZnSnS_4) have a large number of binary and ternary phases. These phases can be detrimental to efficiency, especially when they possess different band gaps, resistivities and unit cell structures [104, 26, 49, 50]. The existing single-element semiconductor materials (Si, Ge, Sn) do not fulfill the selection criteria, so the search is expanded to binary semiconductors. The number of known phases in they binary system is also considered.

The Sn-S phase diagram, shown in Fig. 1-4 is relatively simple and shows three Sn-S phases: SnS, SnS_2 and Sn_2S_3. It is also interesting to note that SnS is believed to evaporate congruently. The SnS phase has a high vapor pressure [65] and the melting temperature of SnS, at 880 °C, is significantly lower than the T_{melting} of silicon at 1414 °C. SnS will require comparatively lower processing temperatures than silicon, CdTe or CIGS. This may also lead to cost savings

during manufacturing.

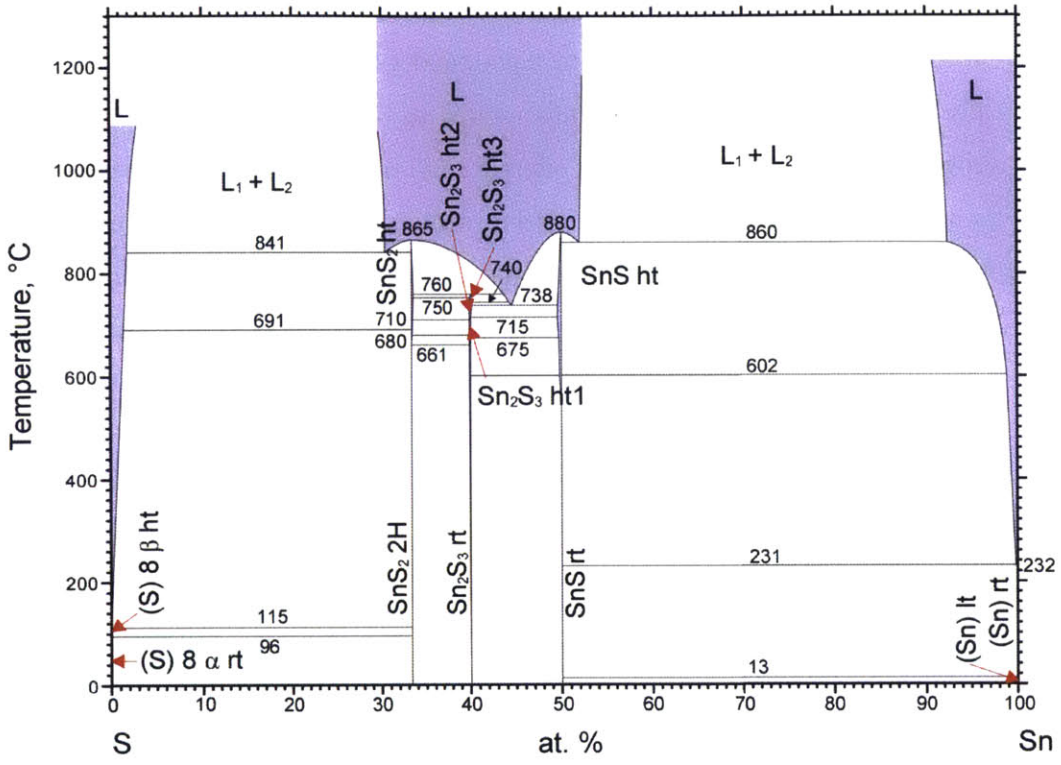

Figure 1-4: Sn-S phase diagram. There are three stable Sn_xS_y phases: SnS, SnS_2 and Sn_2S_3. Image from [79].

2. Band gap is in the region of peak theoretical Shockley-Queisser efficiency.

This region is roughly defined by the Shockley-Queisser efficiency limit and ranges from 1.0 eV to 1.5 eV. During the analysis of the numerous compounds that could be formed from the 29 most abundant elements, several categories emerged. Compounds with band gaps (i.e. semiconductors) tended to be either a phosphide, oxide, nitride, sulfide or silicide. Phosphides were eliminated due to the dangers of synthesis and working with phosphine gas. Several phosphide compounds are reactive with atmospheric water and are actively used as rat poison. One could argue that working with hydrogen sulfide gas, which is commonly necessary for sulfides research, is also dangerous. However, hydrogen

sulfide is generally less toxic and less spontaneously flammable than phosphine, but one must still be aware of safety risks.

On average, the silicides tended to have band gaps that were too small, typically below 1.0 eV. Oxide band gaps tended to be slightly too large, generally above 1.5 eV. Nitride compounds offered a reasonable range of band gaps and even some carrier mobility values were promising. However, at the time of the literature study, there were relatively few reports on nitride semiconductors. Existing reports conflicted and many were purely theoretical studies. Sulfide semiconductors had more promising experimental reports, band gaps within the desired range, and reports of high majority carrier mobilities. Also, two other chalcogenide thin films are in commercial production. The ability to leverage the learning of the CIGS and CdTe community was an additional factor in the selection of SnS and may prove instrumental to the development of this material. In principle, one could adopt the low-cost manufacturing infrastructure of a CIGS or CdTe solar cell plant and use it to produce SnS instead.

Reports of SnS band gaps are surprisingly varied. For the direct band gap, values range from 1.3–2.0 eV [48, 54, 21, 18]. For the indirect band gap, values range from 0.9–1.2 eV [107, 40, 5, 8]. Possible causes of this large range could be lack of phase purity (SnS_2 is thought to have a direct band gap around 1.6–2.3 eV [76, 18, 8]) or quantum confinement effects.

Theoretical calculations suggest that SnS is an indirect band gap semiconductor where $E_g = 1.0$–1.2 eV [41, 44]. A calculated band diagram is shown in Fig. 1-5. At the time of literature research, a majority of empirical papers cited a direct band gap at 1.3 eV [70, 87, 54, 69], which offers this material a 32 % maximum theoretical efficiency. Even with a 1.1 eV indirect gap, the material offers a similar Shockely-Quisser efficiency to silicon: 31 %.

Preliminary band gap and defect calculations by Lany *et al.* calculate an indirect band gap at 1.2 eV and state that tin vacancy defects do not lie near mid-gap. Instead, they lie just above the valence band, providing appropriate p-type

doping. [41, 101]

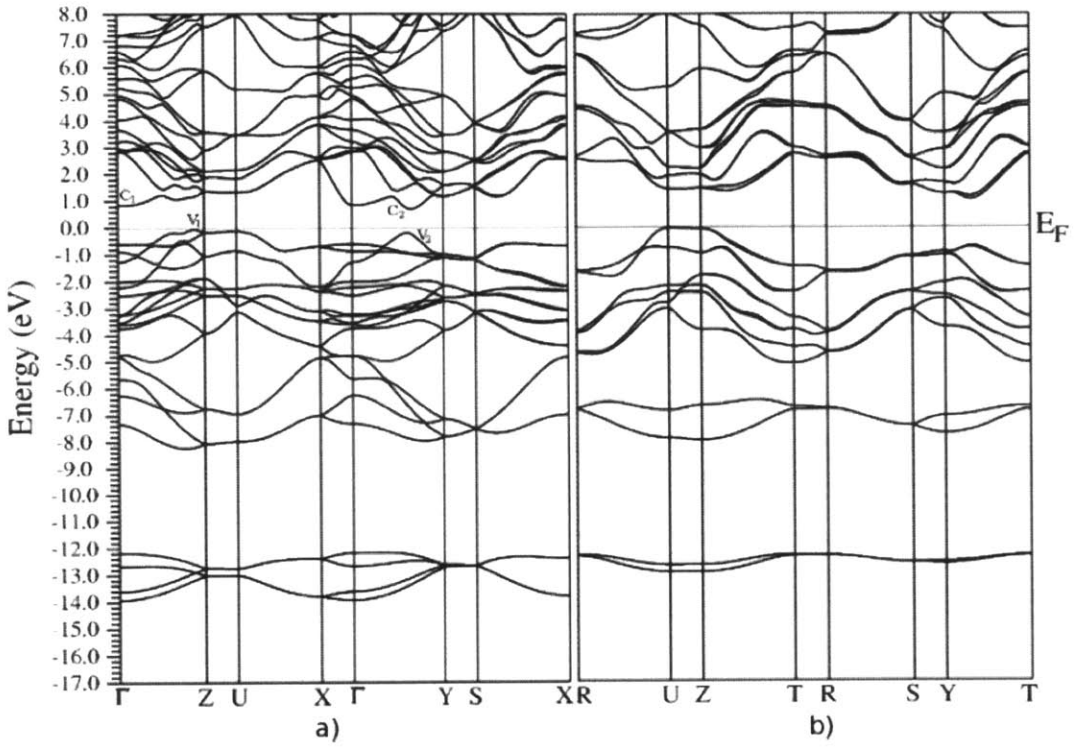

Figure 1-5: a) Calculated band structure of SnS in the most symmetrical path, b) Band structure calculated along a less symmetrical path in the first Brillouin Zone. Points C_1 and V_1 show the indirect band gap. Image from Makinistian *et al.* 2009 [44].

3. High absorption coefficient above 10^4 cm^{-1}.

The material must absorb light strongly to ensure only a few microns of material are required. Typically this implies the compound should be a direct band gap semiconductor, but does not preclude indirect band gap semiconductors, if absorption is high.

Regardless of the type of band gap reported, nearly all reports for SnS show an absorption coefficient above $10^4\,cm^{-1}$ at the direct band gap [54, 18, 87], as seen in Figure 1-6. Using Beer-Lambert's law and assuming we would like to absorb 90 % of incident light above the band gap, with $\alpha = 10^4\,cm^{-1}$, one would need approximately 1 μm of material.

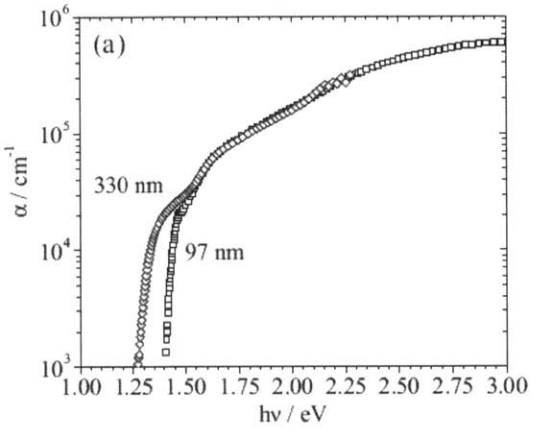

Figure 1-6: The absorption coefficient is plotted for two films, 330 nm thick and 97 nm thick, deposited by ALD (atomic layer deposition). Both films show absorption coeffients above $10^4\,\mathrm{cm}^{-1}$ at the band edge and increase into the $10^5\,\mathrm{cm}^{-1}$ range in the visible light region. Image from Sinsermsuksakul 2009 [87].

4. High minority carrier mobility.

Carriers must be able to move through the material to metal contacts. For solar cells, the relevant value is the minority carrier mobility. This is often a difficult value to determine, so for materials selection purposes, we rely on the majority carrier mobility, typically measured by the Hall effect. It is also useful to note, that due to the calculated curvature of the valence and conduction band edges in SnS, the minority carriers (electrons) are expected to have a higher mobility than the majority carriers (holes) due to reduced effective mass.

The highest reported majority carrier mobility is from Noguchi *et al.* 1994, with a *p*-type thermally evaporated SnS film with a Hall carrier mobility of 400–500 $\mathrm{cm}^2/\mathrm{Vs}$. This film also had a majority carrier concentration of 6.3×10^{14} – 1.2×10^{15} cm^{-3} [54]. However, due to the low carrier concentration of this film, the mobility numbers are slightly suspect. Another SnS film grown by spray pyrolysis is reported to have a Hall mobility of $128\,\mathrm{cm}^2/\mathrm{Vs}$ and a carrier concentration of 1.65×10^{15} cm^{-3} [70].

A 1961 study on single crystal SnS showed a hole mobility of approximately 90 $\mathrm{cm}^2/\mathrm{Vs}$ in the *b*-*c* plane, or perpendicular to the *a*-axis. Along the *a*-axis,

hole mobility is measured to be $18\,cm^2/Vs$ [5]. The strong anisotropy of carrier mobility is due to the orthorhombic crystal structure of SnS. The crystal structure of low temperature α-SnS is a distorted rock-salt orthorhombic configuration. The space group is *Pnma* (No. 62). At 602 °C, there is a second-order phase transition to β-SnS phase with space group *CmCm* (No. 63). The α-SnS phase at room temperature has a unit cell size of $a = 11.200\,Å$, $b = 3.987\,Å$, $c = 4.334\,Å$[24]. The material is layered, where each slab is two atoms thick. Each unit cell has two of these slabs oriented perpendicular to the *a*-axis. The Sn-S bonds within each slab are fairly short and strong (bond distance, $d = 2.627\,Å$) [24]. However, the bonds between planes are weak and longer ($d = 3.388\,Å$). The orthorhombic structure, without inter-plane bonds displayed, is shown in Figure 1-7.

The layered structure of SnS has important implications for carrier mobility and carrier collection potential. Albers *et al.* reported mobility within the *b*-*c* plane (as labeled in Figure 1-7) is 5× greater than mobility along the *a*-axis [5]. Also reported in Sinsermsuksakul *et al.* 2009, there is a 10× difference between the *a*-axis and *b*-*c* plane mobility [87]. To best utilize this anisotropic mobility, films should ideally be grown with the majority of grains oriented such that the *b*-*c* plane is perpendicular to the substrate. This allows high mobility through the thickness of the solar cell, and lower lateral mobility. This feature could reduce recombination by guiding carriers toward the top and bottom contacts.

It is notable that even high efficiency CIGS devices do not have particularly high minority carrier mobilities. A typical range for CIGS minority carrier mobility is 1–20 cm^2/Vs [47].

The existing literature has shown that SnS films can be grown with high majority carrier mobilities and appropriate doping densities. These results indicate there should not be a fundamental mechanism limiting the carrier mobility to low values. While it is certainly possible to grow SnS films with low mobility, it has been demonstrated that SnS has the potential for high minority carrier

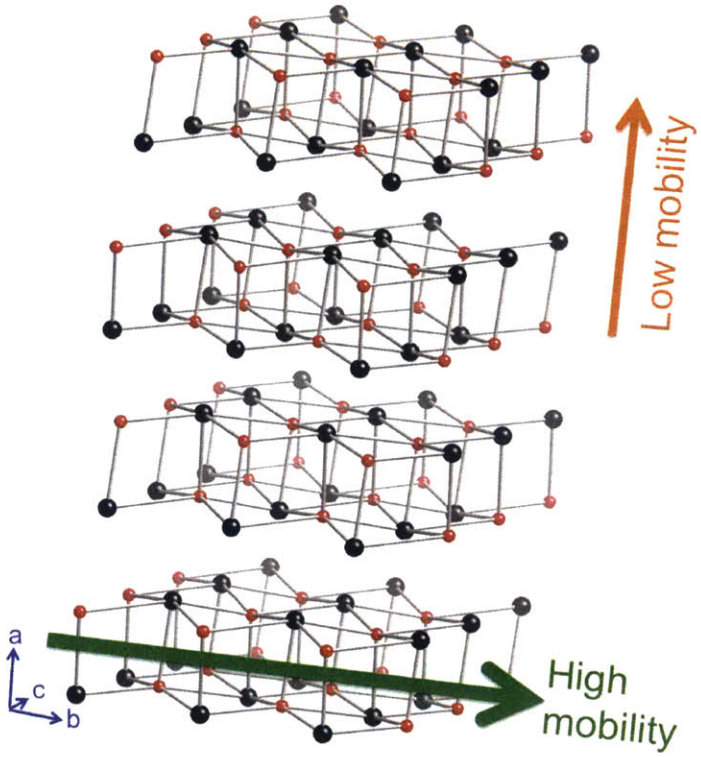

Figure 1-7: The orthorhombic nature of SnS is shown. The slab, or layer, structure contributes to highly anisotropic carrier mobility, where carrier transport along the slabs (in the b-c plane) is higher than through the slabs (a-axis direction). Black atoms are tin and red atoms are sulfur. The bonds between slabs are omitted in this image, to emphasize the layered structure.

mobility.

1.3.1 Diffusion length and $\mu\tau$ product

Minority carrier mobility and likewise minority carrier lifetime are crucial due to Equation 1.1, where L = diffusion length of minority carriers, τ = minority carrier lifetime and D = diffusivity of minority carriers:

$$L = \sqrt{D\tau} = \sqrt{\mu \frac{k_B T}{q} \tau} \tag{1.1}$$

Diffusivity is also defined by the Einstein relation (Equation 1.2), where μ =

minority carrier mobility, k_B = Boltzman constant, T = temperature in Kelvin and q = charge of the particle in Joules.

$$D = \mu \frac{k_B T}{q} \tag{1.2}$$

Increasing the $\mu\tau$ product is the key to increasing the diffusion length of minority carriers and thus increasing collection of carriers generated in the solar cell.

Collection length is one common way of describing a depth into the absorber where minority carriers can still be collected. The farther away a carrier is generated from the p-n junction, the more likely it is to recombine (depending on how the collection length is defined and determined). A simple way to estimate collection length is to assume 100 % collection of minority carriers in the depletion region of the absorber (at 0 V bias) and 100 % collection of minority carriers generated up to 1 diffusion length away from the depletion region. Thus collection length = depletion region width + diffusion length [35]. Increasing the collection length is a key way to improve solar cell performance by collecting more of the carriers that are generated by above-band-gap light. The importance of collection length is what generates the # 4 criteria for high minority carrier mobility. Minority carrier lifetime is notoriously hard to measure for known materials and even more difficult for less well-studied materials. Thus minority carrier mobility becomes the parameter to optimize, although it is also hard to measure. In the absence of a minority carrier mobility measurement, majority carrier mobility can be used as a proxy.

1.4 Previous research and deposition methods

In addition to the above criteria, we review the various methods of thin film deposition that have been previously explored, as well as any other research into SnS material. When working with new and less well-studied materials, the existing papers and research can be helpful, although frequently sparse and contradictory.

1.4.1 Deposition methods explored

Many different deposition methods have been tried and reported, with varying degrees of success. Phase purity and grain size tend to be difficult to control with many of the methods.

Thermal evaporation has been relatively popular and is a favorite of the Miles group in the U.K. [48, 57, 56]. This group has achieved fairly fast deposition rates of 25 nm/s. The first reported solar cell was grown by thermal evaporation and used a CdS buffer layer [54]. Phase purity for thermal evaporation has been a common problem and is frequently noted to change with the substrate and source temperature. It is suspected by this author that phase impurity may be caused by the use of impure source powder, which is a mixture of other sulfur-rich Sn-S phases (Sn_2S_3 and SnS_2).

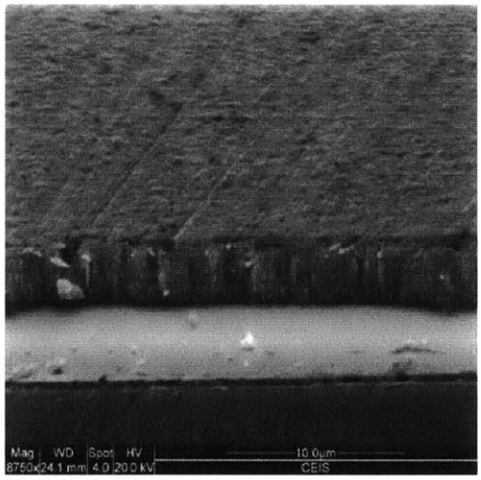

Fig. 1. SEM micrograph of a SnS layer deposited using a 300 °C substrate temperature, a 350 °C source temperature and a deposition time of 2 min.

Figure 1-8: An example of a rapidly deposited (25 nm/s) SnS film grown by thermal evaporation. The film is approximately 3 µm thick. Image from [48].

Other deposition methods include: chemical bath deposition [66], sulfurization of tin [93, 92], electrodeposition [97, 89], atmospheric-pressure CVD (chemical vapor deposition) [67], ALD [87], E-beam evaporation [98], spray pyrolysis [70], MBE (molecular beam epitaxy) [55] and close-spaced vapor transport [105].

RF sputtering from a Sn-S target was briefly reported by Guang-Pu *et al.* in a conference proceeding in 1994 [30]. Reactive sputtering using a Sn target and a

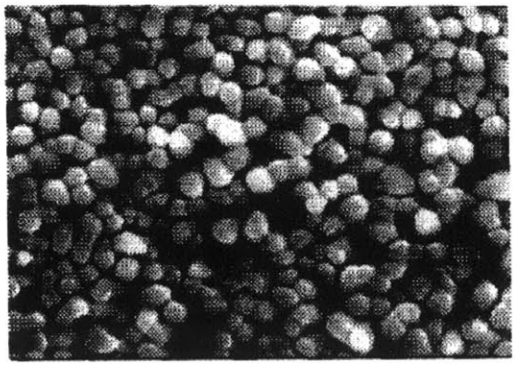

Fig.3. SEM picture of single phase SnS film.

Figure 1-9: An example of a SnS single-phase film deposited by spray pyrolysis. [38]

H_2S/Ar mix is also reported in a Japanese patent by Shinichi and Shigetoshi in 1996 [81].

Due to the few reports on RF sputtering and the possibility for industrial scale-up. RF sputtering of SnS was chosen as a method of choice for initial investigations. Later, as seen in Chapter 2.1.1, lab scale production proved to be difficult. Growth of SnS thin films was then transitioned to thermal evaporation. This method benefits from the sublimation or congruent evaporation property of SnS, reported by Piacente [65].

1.4.2 SnS single crystal studies

In the 1960s, there were several researchers investigating SnS single crystals and reporting on their fundamental properties, the Sn-S phase space and the effect of sulfur pressure on carrier concentration [5, 3, 71, 31, 4]. Single crystals fabricated by this team were never shown to be phase pure and were reported to have up to 10^{18}-10^{19} cm^{-3} concentrations of Pb, Fe, Al, Sb, Ni, Mn, Cu [4]. Antimony is suspected to be a n-type dopant, while Cu is suspected to be a p-type dopant.

However, there were extensive and informative experiments performed and these data can guide some of the experiments to be performed on thin films. Since the mid-60s there has been very little reporting on SnS single crystal studies. Only a

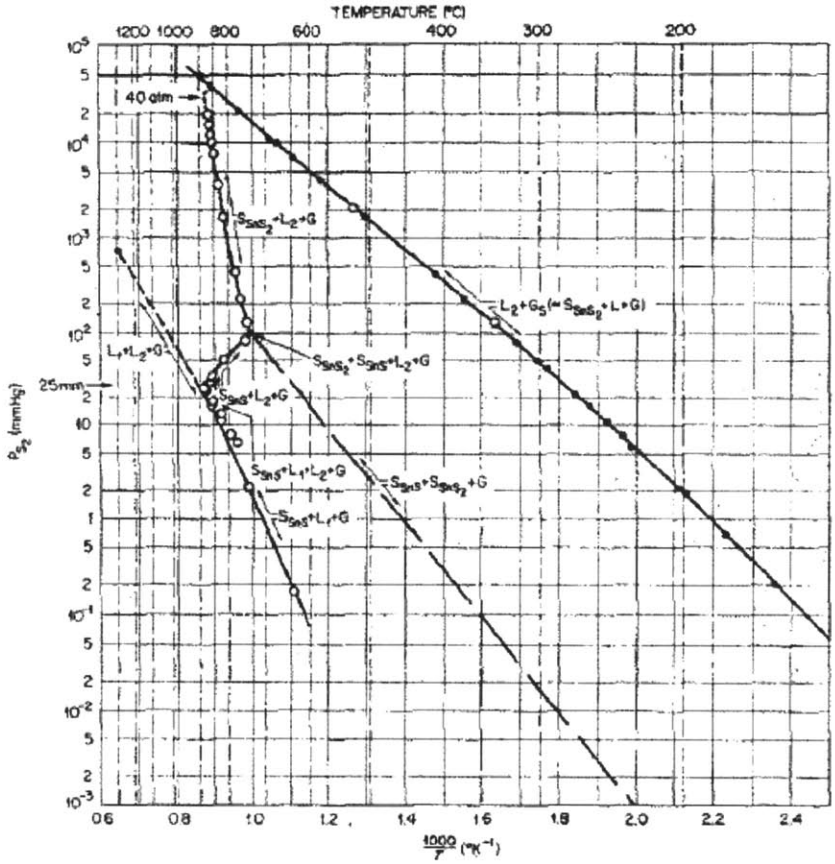

FIG. 3. The S_2 pressure, as a function of temperature, over various three-phase equilibria in the system Sn-S.

Figure 1-10: Sn-S phase diagram, P_{S_2} vs. $1000/T$. Image from [5].

handful have been published in the past 40 years [40, 15, 14, 52, 51].

These papers established the orthorhombic structure of SnS, the dependence of carrier mobility on crystal direction, absorption coefficient and an $\sim$1.1 eV indirect band gap. Crystal structure data is most commonly cited from Ettema *et al.* [24].

Using the infrared reflection spectrum, Haas and Corbey measured the index of refraction $n_0 = 3.6 \pm 0.1$ and the dielectric constant $\epsilon = 19.5 \pm 2$. However, these values have since seen adjustments and further research. Banai *et al.* used spectroscopic ellipsometry and HSE06-DFT to provide a thorough report of both the high frequency (ϵ_∞) and ionic (ϵ_{ionic}) contributions to the static dielectric constant ($\epsilon_0 = \epsilon_\infty + \epsilon_{\text{ionic}}$) for all three principal axes. Where $\epsilon_{\text{ionic}} = 22.72$, 37.64 and 21.36, $\epsilon_\infty = 11.85$, 14.02

and 12.70, and $\epsilon_0 = 34.57$, 51.66, and 34.06 for the a, b and c axes respectively [10].

Albers *et al.* began investigating low temperature Hall measurements, as well as annealing crystals, quenching, then measuring carrier concentration [5]. This paper also explores the phase space on a pressure vs. temperature diagram (Figure 1-10), where pressure is the sulfur (S_2) partial pressure. It is not ever stated in this paper how S_2 pressure is established or measured. Other related papers suggest S_2 pressure is established using a H_2S/H_2 mixture.

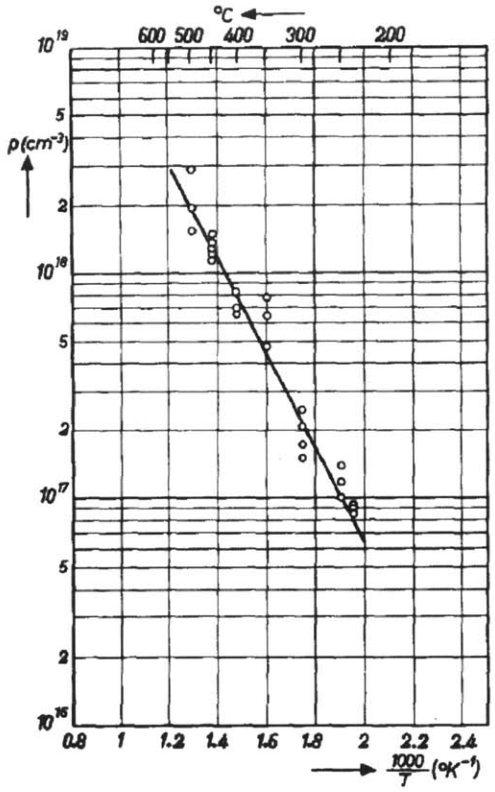

FIG. 7. The concentration of free holes in SnS measured at room temperature, after quenching, as a function of the temperature of annealing.

Figure 1-11: Carrier concentration vs. T_{anneal} of SnS single crystals. Single crystals were quenched and Hall measurements taken at room temperature. Gas pressure and composition information were not described in the paper. The paper hypothesizes the change in $[p]$ observed upon annealing is due solely to ionization and dissociation of tin vacancy pairs, not due to composition change generating more tin vacancies. Image from [5].

The results of an anneal and quench experiment on single crystals are shown in Figure 1-11. However, the details of this experiment are not well explained in the text. To the best determination of this author, the single crystals were annealed in a H_2S/H_2 atmosphere with a S_2 partial pressure maintained at the SnS/Sn_2S_3 phase transition, which is specific to each annealing temperature and could possibly be determined from Figure 1-10. The length of anneal and method of quenching were not revealed, leaving the results of this experiment difficult to interpret. One must assume equilibrium in the crystal was reached for each anneal temperature, and that the rate of quenching was fast enough to lock in properties of the anneal temperature. [5]

The Albers *et al.* 1961 paper states that the crystals did not change composition during annealing because the anneals at different temperatures could be repeated and the majority carrier concentration for that temperature was recovered. It is implied that this can only happen if stoichiometry is maintained during the anneals. However, examining the temperature range of anneals and comparing to Figure 1-10, there is nearly no region where it is possible to maintain SnS phase and exact stoichiometry. The temperature range of the experiments appears likely to cross a phase boundary unless the pressure was maintained at low P_{S_2}. However, the pressure and gas composition for these anneal + quench experiments is never stated. [5]

Additionally, the paper also states that because no change in composition is occurring, the change in carrier concentration must be due solely to ionization. They assume further that all SnS is sulfur-rich and there are so many tin vacancies that at lower temperatures they will associate. These associates can then dissociate and generate holes at higher temperatures:

$$2h^{\bullet} + 2V'_{Sn} \rightleftharpoons (V_{Sn}V_{Sn})^{\times} \tag{1.3}$$

$$4h^{\bullet} + 2V''_{Sn} \rightleftharpoons (V_{Sn}V_{Sn})^{\times} \tag{1.4}$$

When dissociated, each tin vacancy can either generate one or two holes, depend-

ing on its ionization state. The paper then uses the slope on a ln $[p]$ vs. $1/T$ graph to derive the association energy for each scenario in Equations 1.3 and 1.4, where slope $= E_{\text{assoc}}/4k_{\text{B}}$ or $E_{\text{assoc}}/6k_{\text{B}}$, respectively. The paper finds these values for singly and doubly ionized V_{Sn} acceptors at 1.4 eV and 2.1 eV. This author has repeated the calculation by digitizing the data and find these association energies to be -1.4 eV and -2.5 eV, respectively.

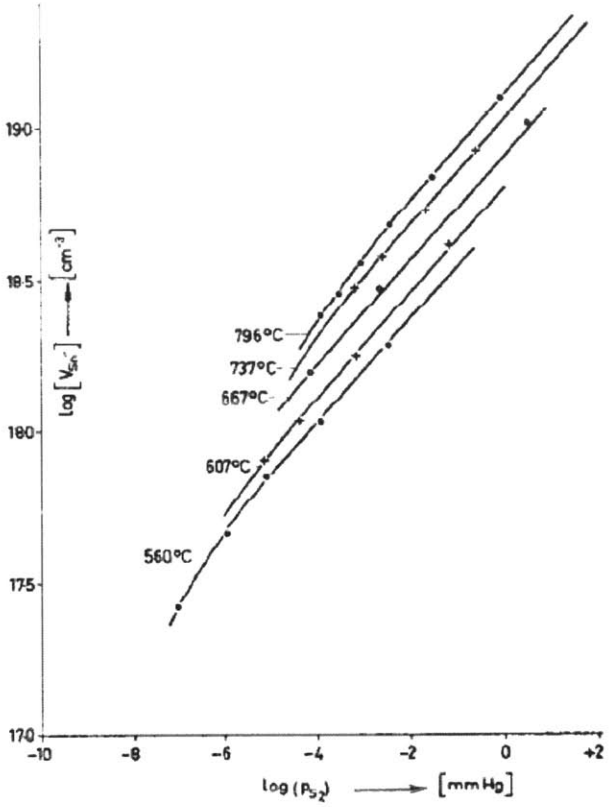

FIG. 4. Theoretical curves and experimental points if only V''_{Sn} exists.

Figure 1-12: Defect concentration vs. P_{S_2} of anneal for SnS single crystals annealed at various temperatures from 560 to 796 °C. Carrier concentration is measured *in-situ* during anneal and the result is converted to $[V''_{Sn}]$ by assuming $p = 2[V''_{Sn}]$. Image from [71].

In 1966, Rau performed studies on crystals where P_{S_2} and temperature were varied during annealing and carrier concentration measured *in-situ*, resulting in Figure 1-12. P_{S_2} was again generated with a H_2S/H_2 mixture and independently measured with

a home-built apparatus. However, the apparatus measured difference in S_2 pressure from one data point to the next, not absolute sulfur partial pressure. Thus the x-axis in Figure 1-12 could be shifted by some constant value. [71]

The data in Figure 1-12 shows that sulfur partial pressure can be used to generate holes in SnS by the creation of tin vacancies. It is interesting to note, however, that the data only extends down to 560 °C. Three of the experimental temperatures (796, 737, 667 °C) are above the α→β SnS phase transition at 602 °C. This point is not made in Rau's text and it is unclear what effect this may have on properties such as diffusivity of mobile species and formation energy of vacancies or other defects. The SnS βphase is also observed to have a small amount of solubility for excess sulfur or tin atoms, while the SnS α-phase is observed as a line phase [79].

1.4.3 Previously reported SnS solar cells

The earliest reported photovoltaic conversion efficiency for SnS is from Noguchi *et al.* 1994, at 0.29 % with a thermally evaporated SnS layer and a CdS buffer layer [54]. The structure was superstrate: glass/ITO/n-CdS/p-SnS/Ag. The cell had a V_{OC} of 0.12 V, a J_{SC} of 7 mA/cm^2 and a fill factor of 35 % under approximately 1 sun illumination.

In 1997, N. Koteswara Reddy *et al.* reported at the IEEE PVSC a 0.5 % cell again using a superstrate configuration: Al/n-CdS/p-SnS/Ag with an active area of 0.5 cm^2 [38]. This SnS was deposited by chemical spray pyrolysis and had a V_{OC} of 0.14 V, a J_{SC} of 8.4 mA/cm^2 and a fill factor of 38 % under approximately 1 sun illumination.

In 2006, K.T. Ramakrishna Reddy *et al.* reported a 1.3 % cell again using spray pyrolysis to deposit the p-type SnS and a n-type 2 % In-doped CdS layer by vacuum evaporation [70]. This cell is most notably grown in substrate configuration, although is probably still illuminated from the "back," or the glass side. The stack reported in order of deposition is: glass/SnO_2/SnS (600 nm)/CdS (600 nm)/In (400 nm). Compared to the previous cell, this device (active area = 0.3 cm^2) primarily showed improvement in V_{OC}=0.26 V and FF=53 %. The cell still had a low J_{SC} = 9.6 mA/cm^2. This cell showed particular promise and a significant increase in reported efficiency,

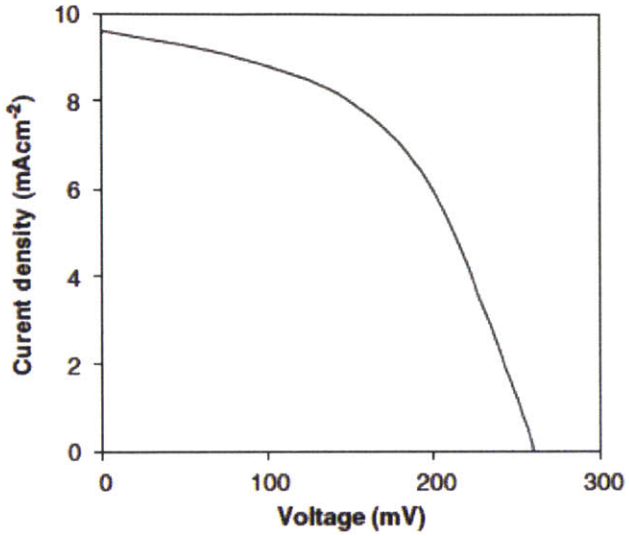

Fig. 3. Illuminated *I–V* characteristics of SnS/CdS device.

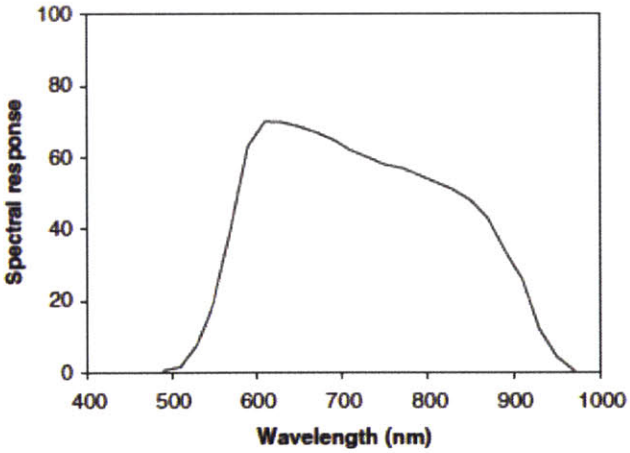

Fig. 4. Spectral response SnS/CdS solar cell.

Figure 1-13: SnS/CdS solar cell by spray pyrolysis, $\eta = 1.3\,\%$. This cell shows improved V_{OC}, while J_{SC} and FF still remain low. The quantum efficiency data in the lower panel suggests parasitic absorption from the CdS layer or poor front surface passivation. Image from [70].

V_{OC} and FF. It is suspected that if the CdS layer had not been so thick (600 nm), more current may have been observed. In CIGS cells, more common CdS buffer layer thicknesses range from 10–40 nm to avoid significant absorption above the CdS band

gap ($\backsim$ 2.4 eV).

This paper is also one of the first reports of annealing. The paper reports that the as-deposited SnS films were annealed in a sulfur atmosphere at 300 °C for 60 min, which "improved physical properties." No further information about the anneal is given. The anneal was said to further promote the (111) orientation the film and reduce the carrier concentration to $5.3 \times 10^{14}\,\mathrm{cm}^{-3}$. Figure 1-13 shows the JV curve and EQE of their champion cell.

The literature over the years has been sparse and significantly lacking in experimental details. Many of these findings would benefit from experimental reproduction and verification by another lab. However, new materials do not often garner the attention needed for such verification. Out of necessity, this author relies on the current state of SnS literature, while bearing in mind that new results may deviate from those previously reported.

1.5 Summary and goals of thesis

There is a need for a diversity of solar cell materials. No one material is perfect for all solar cell applications. By investigating other solar cell materials, we can learn how to engineer and design better solar cells. I have shown that for the outlined criteria of the properties of a high-performing solar cell material, tin monosulfide (SnS) is a promising solar cell material candidate. However, its solar cell efficiency is quite poor, last reported at 1.3 %. The outstanding question is "why?" Why should this otherwise promising solar cell material have such a low efficiency? Is it simply lack of funding or research interest? Or is there something more fundamental about the material? Is there a reason why its efficiency will never be 20 %? Fundamental materials analysis can begin to offer answers. This thesis begins to examine the details of the SnS system and learn about its defects.

For tin sulfide material, I use annealing in H_2S gas as the primary means of impacting the defect structure inside the thin film. It is my goal to use annealing to understand intrinsic and structural defects in tin sulfide, then apply this understand-

ing to be able to improve SnS conversion efficiencies.

1.5.1 Description of chapters

Chapter 1 explains the motivation and selection criteria used to select SnS as a promising solar cell material. It also explores the physical properties of SnS and reviews what was known at the time of selection. Some of the first SnS cells reported in literature are also reviewed.

Chapter 2 explores growth of SnS initially by RF sputtering, then by thermal evaporation. Initial solar cell results from thermally evaporated (as-deposited) SnS thin films are presented and the SnS device stack design is discussed. This stack design is later used to test annealed SnS films.

Chapter 3 is a motivation for annealing films in H_2S. Two different models for defect concentrations are explored and compared. Using data from FactSage (a thermodynamic calculation program), the necessary capabilities for a new H_2S furnace are outlined. These capabilities have been selected to allow a strong increase in SnS solar cell performance after parameter optimization.

Chapter 4 is a description of the design and building of the H_2S furnace. Design requirements were stringent due to the toxic and corrosive nature of H_2S gas. Selection of an RGA (residual gas analyzer) is discussed and the design of experiments used to calibrate the gas analyzer to be able to quantify the partial pressure of sulfur gases is also reviewed.

Chapter 5 describes the results of two rounds of annealing tests. In the first round, as-deposited films are annealed in H_2S/H_2 gas mixtures and a trend of increasing carrier concentration with an increase of an uncalibrated S_2 gas signal from the RGA is observed. The second round of experiments aims to reduce the impact of kinetics during annealing, so that the effect of thermodynamic parameters can be evaluated. An anneal temperature and sulfur partial pressure parameter sweep were both performed on material that had been "pre-annealed" to

increase grain size and reduce the impact of changing grain boundaries on mobility measurements. In the process of doing these anneals, solar cells with similar annealing parameters were made and found to have higher median efficiency than the current standard annealing procedure. The improvement primarily comes from an increased J_{SC} and fill factor.

Chapter 6 Conclusions

Chapter 2

Growth of SnS films and devices

2.1 RF sputtered SnS films

Prior to beginning this research, only one conference proceeding existed on the sputtering of SnS [30]. Because sputtering is an industrially scalable deposition method, I took this opportunity to explore the use of RF sputtering for SnS thin film deposition. It was the goal to create a Structure Zone Model for SnS thin film growth by sputtering. It is generally believed that target power, argon pressure, gas flow rate and substrate temperature can all be used to make minor adjustments in film stoichiometry and morphology.

Non-reactive sputtering was initially selected because working with H_2S gas can be dangerous and expensive due to safety equipment. Non-reactive sputtering ideally requires a SnS target with a stoichiometric ratio of Sn/S = 1.00 (50 % Sn and 50 % S), assuming no preferential sputtering of the Sn or S atom.

2.1.1 Effects of argon pressure

A nominally SnS target was purchased from Plasmaterials, for use in a sulfide sputtering system at the University of Utah. The 3-inch diameter Plasmaterials target was pressed and sintered from 99.5 % pure SnS powder. However, during the sintering process, the stoichiometry was altered. XRF measurements revealed the target to

actually be 38.7 % atomic Sn and 61.3 % atomic S. This is much closer to the Sn_2S_3 phase, rather than the SnS phase.

Experimental

SnS thin films were deposited on soda-lime glass microscope slides. All substrates were manually scrubbed using detergent, then rinsed in deionized water, acetone, methanol, and isopropyl alcohol and finally, exposed to ultraviolet-generated ozone for 2 minutes. All samples had a deposition time of 60 minutes, a substrate rotation of 18 rpm, a base pressure of $1\text{–}6\times10^{-7}$ torr, and an initial unheated substrate temperature of 25 °C. Reflected power was maintained within a 0–2 W range. Four SnS thin films were created with varying argon pressures (5–60 mtorr) and an approximately constant power. At this power level, the substrate experienced a temperature increase to at least 80 °C over the 60 minute deposition.

Characterization

Films were characterized by XRD, SEM, profilometry, WDS (calibrated by RBS), four-point probe, and UV-Vis spectrophotometry (reflection and transmission). The error associated with RBS (Rutherford backscattering spectrometry) results range from 0.2-0.5 at. % for tin and 0.2-1 at. % for sulfur. Standard matrix (ZAF) corrections were made for the WDS (wavelength-dispersive spectroscopy) results, however these films do not conform very well to these assumptions. They are neither flat nor homogeneous. Thus error from WDS measurements may be larger than 1–2 at. %.

Results

A summary of deposition parameters and main characteristics is shown in Table 2.1

X-ray diffraction data for four SnS thin films are shown in Figure 2-1. All peaks in samples A through C are matched to the orthorhombic phase of SnS, using International Centre for Diffraction Data (ICDD) PDF card # 00-039-0354 (space group: *Pbnm*; a = 4.329 Å, b = 11.192 Å, c = 3.984 Å). These samples are confirmed to be SnS.

Sample Label	A	B	C	D
Argon pressure (mtorr)	5	10	30	60
Power (W)	150	160	150	150
Film thickness (μm)	1.58	1.06	0.46	0.23
Indirect band gap (eV)	1.18	1.12	1.08	-
Sn/S ratio	1.07	1.08	1.10	1.02
Grain length (nm)	198	195	100	30
Resistivity (Ω-cm):	1,100	13,900	97,000	33,000

Table 2.1: Sputtering deposition parameters (upper) and measured material characteristics (lower) for four tin sulfide thin films. Sputtering time was 60 minutes.

The relative intensity of the (002) peak decreases from Sample A to C, indicating a change in the preferential growth orientation of these films.

In sample D, the shift of the two main XRD peaks away from SnS peaks (101) and (111) indicate that this film may contain a different phase. The sample D peak at 30.9° 2θ matches well to the (310) peak in the Sn_2S_3 phase (ICDD PDF card # 00-014-0619). Sample D also exhibits a broadened peak at 31.4° 2θ, which correlates to the decreased lateral grain size, as observed in the SEM image (Figure 2-2).

In samples A–C, SnS films exhibit an elongated grain shape when imaged in plan-view at the film surface (Figure 2-2). The "rice-shaped" grains in these images appear to be comprised of elongated nanocrystallites less than 25 nm in thickness. The shape of these nanocrystallites closely follows that of the elongated grain. Grain length (Table 2.1), as measured along the long axis of the grains, is comparable to that of other SnS films produced by thermal evaporation with a substrate heating of 300 °C [22]. Note the maximum temperature experienced by the RF sputtered films during growth was approximately 80 °C.

An apparent trend of decreasing grain size with increasing pressure for samples A to C is observed in plan-view SEM images. Sample D exhibits a qualitatively distinct grain structure from the other films. Grains on the order of 30 nm lack the characteristic elongated shape of samples A–C, but maintain the sub-grain nanocrystallite structure.

Cross-sectional SEM images suggest the films are highly porous (Figure 2-3). The cross-sectional image of sample A, the thickest film, indicates two characteristic

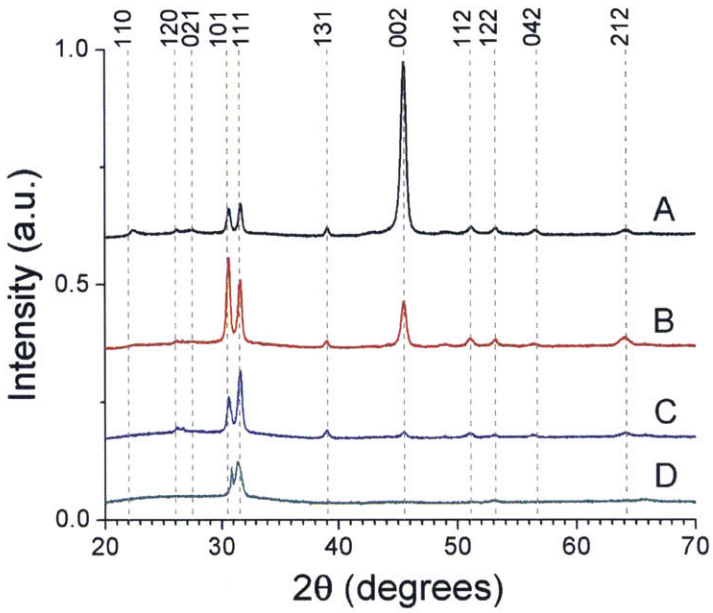

Figure 2-1: X-ray diffraction data for the four samples depicted in Table 2.1. Dashed lines represent SnS diffraction peak positions listed by ICDD PDF # 00-039-0354. The data indicate that samples A, B, and C are SnS, while sample D may be Sn_2S_3 (ICDD PDF card # 00-014-0619). Image from [33].

regions. The first region, within 200–300 nm from the SnS-glass interface, contains a prevalence of small grains (on the order of 25 nm in diameter). The second region contains the elongated grains, also seen in plan-view, several of which appear to extend through most of the film thickness. Gaps frequently appear between grains in this second region, indicating elevated film porosity.

The trend of decreasing grain size in samples A to C may not be due solely to increasing argon sputtering pressure. In our experiments, this growth parameter is convoluted with changes in film thickness and growth rate, two parameters known to affect grain size in other material systems. Typically, grain size decreases as film thickness decreases, which is also observed here.

For all samples, an absorption coefficient is observed in the 10^3–$10^4\,cm^{-1}$ range within a few hundred meV from the absorption onset (Figure 2-4b). Samples A through C exhibit qualitatively similar absorption coefficient vs. photon energy behavior, and the absolute value appears to increase from A to C. The absorption

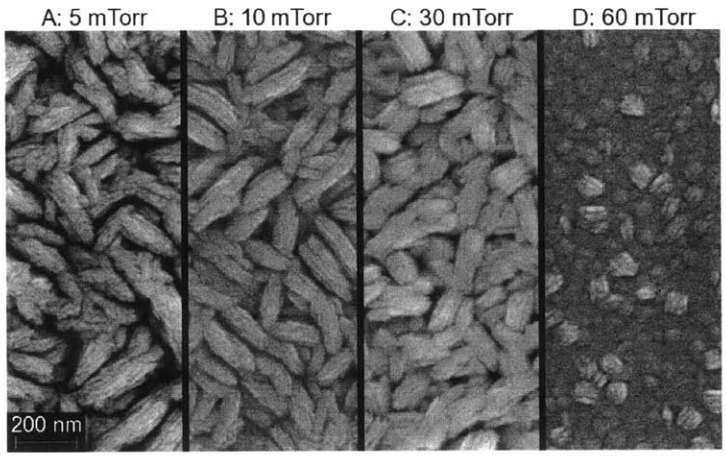

Figure 2-2: Plan-view SEM images of representative regions of four samples listed in Table 2.1. Samples A–C exhibit an elongated grain morphology with evident porosity, while Sample D exhibits a less porous, equiaxed structure. Intragranular nanocrystallites are also observed. Image from [33].

coefficient behavior for sample D is distinct from that of samples A–C. This is consistent with observed departures from trends in XRD signature, grain morphology, stoichiometry, and resistivity.

Standard models for extracting band gap energy and character rely on fitting energy-dependent absorption coefficient data. For direct band gap transitions, the straight-line portion of the α^2 vs. photon energy plot corresponds to the parabolic shape of the E vs. k diagram near the conduction band minimum [27, 58]. For indirect band gap transitions, a $\alpha^{1/2}$ vs. photon energy plot is used.

In Figure 2-4a, a linear portion for samples A–C is apparent, indicating that the indirect band gap relation is applicable. Indirect band gap values are listed in Table 2.1. A satisfactory linear fit for a direct band gap estimation cannot be made for any sample plotted on a α^2 vs. photon energy diagram, i.e., no straight line can be drawn for a significant portion (> 0.1 eV) of the energy scale. The absorption coefficient vs. photon energy of sample D does not conform to either direct or indirect band gap fitting. If sample D is a multi-phase mixture, as suggested by XRD and stoichiometry measurements, then one could not expect to observe simple behavior.

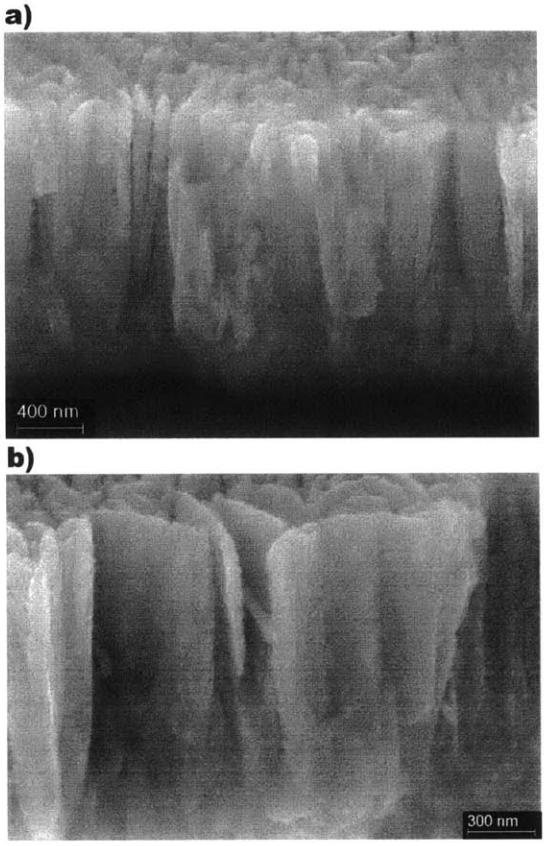

Figure 2-3: Cross-sectional SEM images of sample A acquired at 45 ° relative to the surface, illustrating: a) the entire film thickness, and b) and the region closest to the film surface. Within 200–300 nm from the substrate, a high-density, small-grained morphology can be observed. Above 300 nm from the interface, directional grain growth can be observed, albeit with considerable porosity. Image from [33].

Discussion

Despite a Sn-poor target, the films deposited were slightly Sn-rich. In samples A–C, a trend of increasing Sn/S ratio with decreasing thickness is observed. A similar trend has also been observed for SnS films deposited by thermal evaporation at 300 °C [22]. The high resistivities and possible lack of phase purity suggest that growth by sputtering has not yet been optimized. High resistivity may be caused by the decrease in film thickness, interface scattering along the surface and grain boundaries, percolation effects, or off-stoichiometry.

The morphology of these films is interesting and surprising. Typically, crystalline

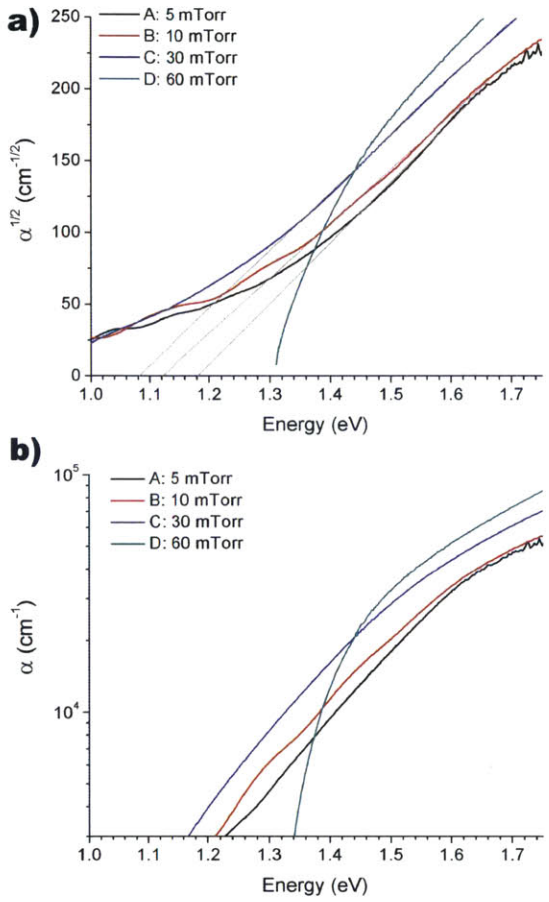

Figure 2-4: Optical absorption measurements: a) a plot using the indirect band gap model, proportional to $\alpha^{1/2}$, b) absorption coefficient vs. photon energy. Samples A, B, and C have indirect band gaps, while sample D does not conform to either a direct or indirect band gap. Image from [33].

films do not tend to grow at room temperature. These results were repeatable using the same target and deposition system. However, when a new target from a different provider was used, the same results could not be obtained. It is suspected that differences in target stoichiometry, as well as changes to the deposition system, are responsible.

RF sputtered SnS has now been characterized with respect to varying argon pressure. Larger grains are needed for improved conductivity and carrier collection. The stoichiometry of the sputtered films should continue to be closely monitored because this off-stoichiometry is suspected to strongly impact electrical properties. It is inter-

esting to note the small-grained region observed near the glass/SnS interface (Figure 2-3b) is also observed in 370 nm thick ALD-grown SnS films [87].

2.1.2 Exploring effects of substrate temperature

A sputtering system at MIT, utilizing a 2-inch diameter target, was used for this study (the sputtering system in Utah did not have a substrate heater). A 2-inch diameter target was purchased from SemiWafer Inc. The original powder was 99.9 % SnS and was also pressed and sintered. The resulting target composition, measured by WDS, was 32 % Sn and 68 % S. This composition is very near the Sn_2S_3 phase, but different from the first SnS target purchased (Chapter 2.1.1). The target used for the substrate temperature studies was more Sn-poor than that used for the argon pressure study.

Experimental

SnS thin films were deposited on soda-lime glass microscope slides (1 mm thick). All substrates were manually scrubbed using detergent, then rinsed in deionized water, acetone, methanol, and isopropyl alcohol. Substrates were pre-cleaned for 1 minute using an argon-oxygen gas plasma at 3 mtorr and 25 W power. Deposition time varied slightly, between 80–90 minutes, to deposit the same thickness of film for each sample. The deposition rate ranged from 2.1–2.6 Å/s for the five samples. Substrate rotation was 19 rpm and base pressure was at least 2×10^{-5} torr. All substrates sat in the chamber for at least 20 minutes, while the substrate heater ramped up to temperature and equilibrated. RF power applied during deposition was 90 W and the argon pressure was always maintained at 3 mtorr. Reflected power was maintained within a 0–1 W range. Samples were allowed to cool within the chamber, with no argon flowing, for at least 20 minutes or until the substrate temperature was below 100 °C.

Results

Figure 2-5 shows the plan-view SEM images of five films deposited at different temperatures: room temperature (RT), 74 °C, 130 °C, 201 °C and 351 °C. The homologous temperature, defined as $T_{\text{substrate}}/T_{\text{m,SnS}}$, and average grain length are also included. The five films had an average thickness of $1.23\,\mu\text{m} \pm 0.1$.

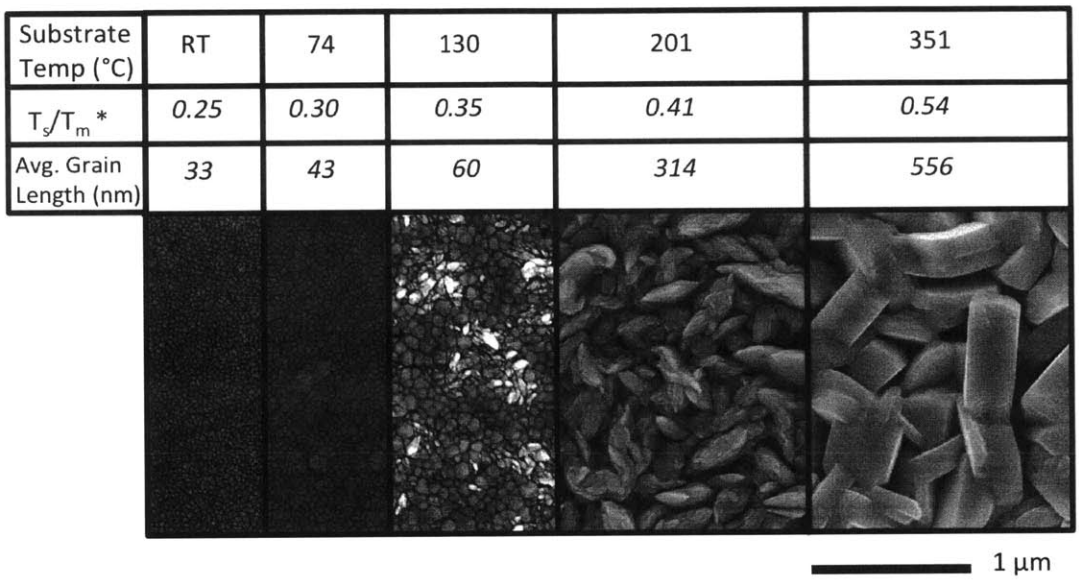

Figure 2-5: Plan-view SEM images are shown for five RF sputtered SnS films of approximately the same thickness. The substrate temperature, homologous temperature and average grain length are listed above each image. Grain size increases as substrate temperature increases.

Profile SEM images (Figure 2-6) also show the films are dense, with no voids. This is a significant change from the previous depositions of Chapter 2.1.1. In samples deposited at 201 °C and 351 °C, through-thickness grains are observed.

XRD results are plotted in Figure 2-7 and described in Table 2.2. The RT and 74 °C sample are completely amorphous, while the next three show varying degrees of crystallinity. As shown in Table 2.2, the phase purity is in question for all samples. Additionally, the α-SnS phase that best matches the peak positions is a pattern collected at 427 °C (ICDD PDF card # 04-004-3833). This suggests there may be an impact on unit cell size when depositing at elevated temperatures. Alternatively,

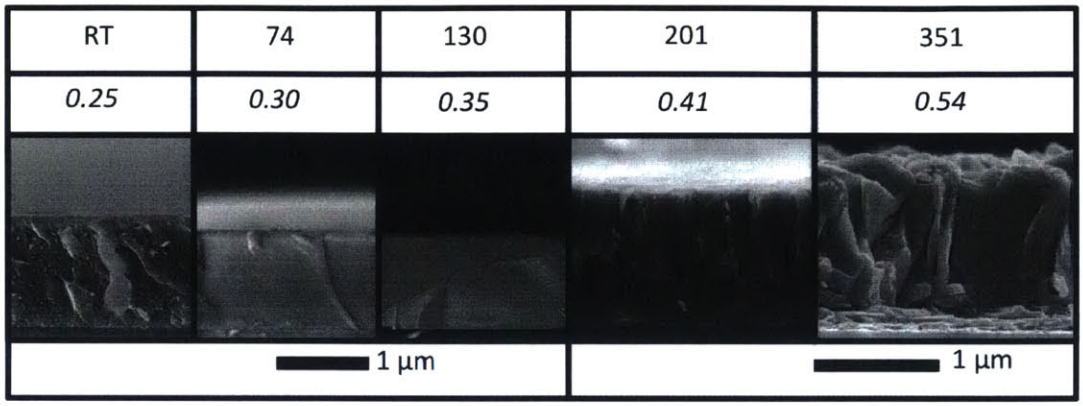

Figure 2-6: Profile SEM images are shown for five RF sputtered SnS films. The substrate temperature (°C) and homologous temperature are listed above each image. Note the change in scale between the left three images and right two images.

there may be induced strain, due to differences in thermal expansion coefficients.

Temp (°C)	Resistivity (Ω-cm)	Sn/S ratio	Crystallinity
RT	10^4+	0.88	Amorphous
74	10^4+	0.75	Amorphous
130	10^3+	0.82	Two broad peaks. Sn_2S_3 possible.
201	7.3	0.79	Possible mixture of β-SnS, α-SnS, and Sn_2S_3.
351	124	1.03	α-SnS, with Sn_2S_3 minority phase.

Table 2.2: For each SnS film deposited at a different substrate temperature, the resistivity, stoichiometry and phase purity (from XRD results) is listed. Although the 351 °C sample is mostly α-SnS, its pattern matches most closely with ICDD PDF card # 04-004-3833, which was taken at 427 °C.

Optical absorption results are presented for the 351 °C sample (Figure 2-8). According to XRD and Sn/S ratio data, this sample is the closest to pure SnS. However, in Figure 2-8a the absorption never drops off below the band gap. This suggests that the film may be degenerately doped. An attempted Hall measurement also supports this hypothesis. The Hall voltage was very low, suggesting a high majority carrier concentration. A linear fit on a $(\alpha h\nu)^2$ vs. photon energy plot suggests a direct band gap at 1.24 eV.

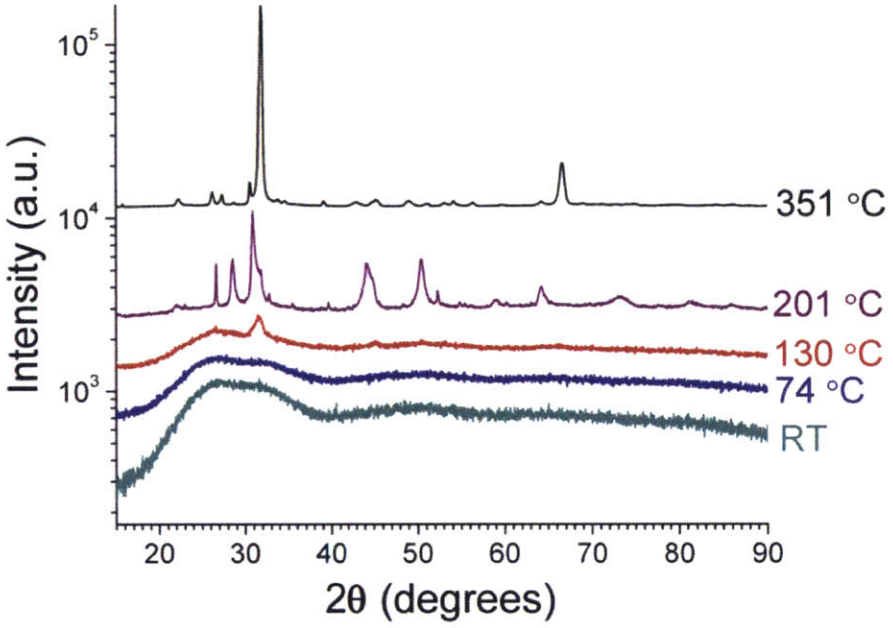

Figure 2-7: XRD results of five SnS thin films with varying substrate temperature. The RT and 74 °C are both amorphous, while the three higher-temperature samples have varying degrees of crystallinity and phase purity, described further in Table 2.2.

Discussion

The trend of increasing grain size with increasing substrate temperature is observed. The 351 °C sample displays columnar, or nearly equiaxed, grains. This sample also has a stoichiometry ratio close to 1.0. This is supported by the XRD study, where the majority of the film is SnS. It is observed in thermal evaporation studies, that a substrate temperature around 350 °C yields the most stoichiometric films [48]. This sputtering data supports that finding. The general trend of increasing Sn/S ratio as substrate temperature increases is also observed in Devika *et al.* 2006, although the absolute Sn/S ratios differ [21]. The Sn/S ratio contains a large degree of error, stemming from the use of EDS and WDS to determine atomic ratios. This amount of error is doubled when calculating the Sn/S ratio.

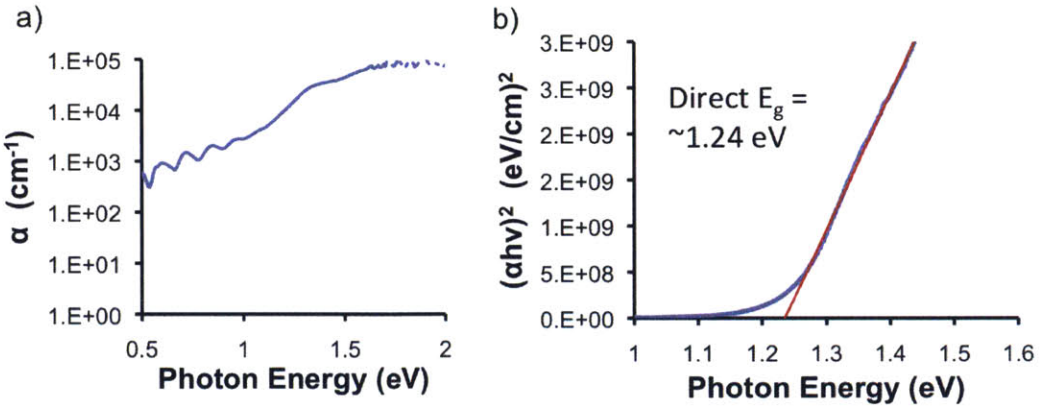

Figure 2-8: Using reflection and transmission data, α was calculated for the sample deposited at 351 °C. a) The absorption coefficient is above $10^4\,\mathrm{cm}^{-1}$ near the band edge, b) this film is found to have a direct band gap at 1.24 eV.

2.1.3 Effects of substrate type: Gold and platinum

These initial experiments were performed to explore back contact metals for SnS films. Gold and platinum are typically known as good Ohmic contact metals, due to their large work functions.

Experimental

Soda-lime glass substrates were manually scrubbed using detergent, then rinsed in deionized water, acetone, methanol, and isopropyl alcohol. Substrates were pre-cleaned for 1 minute using an argon-oxygen gas plasma at 3 mtorr and 25 W power. The Au or Pt film was DC sputtered in the same chamber, before SnS deposition, at room temperature. The metal films are approximately 100–200 nm thick.

After depositing the Au or Pt, and prior to beginning the SnS deposition, the chamber was opened to the air to allow loading of additional substrates and the addition of a mask to the glass/metal stack. The target used for these SnS depositions is the same as discussed in Chapter 2.1.2. SnS deposition time for the glass/Au stack was 90 minutes and for the glass/Pt stack was 108 minutes. Substrate rotation was 19 rpm and base pressure was at least 2×10^{-5} torr.

All substrates sat in the chamber for at least 20 minutes, while the substrate heater

ramped up to 201 °C and equilibrated. RF power applied during SnS deposition was 90 W and the argon pressure was always maintained at 3 mtorr. Reflected power was maintained within a 0–1 W range. Samples were allowed to cool within the chamber, with no argon flowing, for at least 20 minutes or until the substrate temperature was below 100 °C.

Results and discussion

Deposition on the gold thin film yielded surprising results. As shown in Figure 2-9, the glass/Au/SnS stack has a distinctly different grain morphology than films deposited with the same parameters but without the gold layer (Chapter 2.1.2, Figure 2-5). The film is dense with equiaxed grains approximately 800–1000 nm in diameter. The film has flat portions, approximately 800 nm thick, and certain grains which protrude from the flat areas another 200 nm. It is suspected these protruding grains may have a different grain orientation.

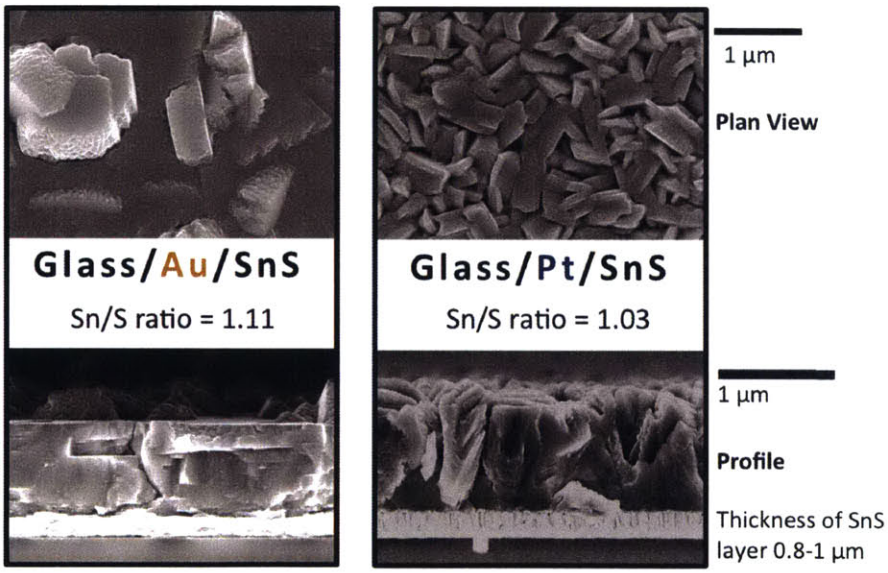

Figure 2-9: Left: SEM views of an SnS film sputtered onto gold at 201 °C. The film has a distinct morphology, with dense and equiaxed grains. Right: SEM views of an SnS film sputtered onto platinum at 201 °C. Grains are slightly larger than those in films without platinum.

The XRD diffractogram on the glass/Au/SnS stack is shown in Figure 2-10. The

gold peaks are indicated and all other peaks are SnS. A few small peaks may be Sn_2S_3, suggesting a small minority phase. The XRD data also indicate a strong orientation preference. Peaks near 32° 2θ and 66° 2θ are traditionally not strongly preferred, but in this film, they dominate. The Sn/S ratio of this film is 1.11, suggesting a Sn-rich phase. Note that other SnS films on glass, with the same deposition parameters, have a Sn/S ratio in the 0.7–0.8 range.

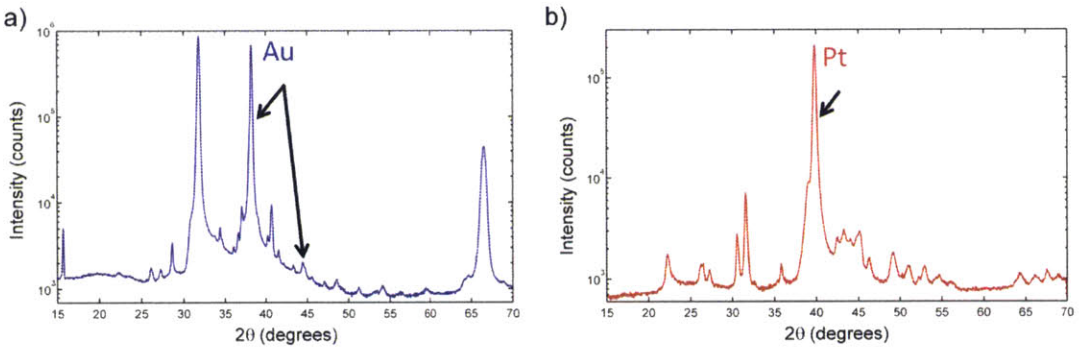

Figure 2-10: a) XRD results of SnS on gold. The film shows a strong orientation preference and a possible Sn_2S_3 minority phase. b) XRD results of SnS on platinum. The film does not show a strong orientation preference. It also contains a Sn_2S_3 minority phase.

Deposition of SnS on platinum show an altered grain morphology. However, the change is not as dramatic as the gold case. Compared to films grown at 201 °C without platinum, the grains are in the 500–700 nm range and more plate-like. The profile SEM reveals a dense film with columnar grains (Figure 2-9). The Sn/S ratio is 1.03, which is ideal when compared to the Sn-poor films deposited without platinum. The XRD data does not strongly suggest a preferred orientation, however a Sn_2S_3 minority phase is present.

We observe that the substrate, in particular gold, can have a strong impact on grain growth and morphology. This phenomenon is not understood and is worthy of investigation.

2.2 Thermally evaporated SnS films

2.2.1 Motivation for thermal evaporation

Alternative methods of growth were investigated due to phase impurities in the RF sputtered films. Thermal evaporation takes advantage of the property of congruent evaporation, unique to the SnS phase. Vaporization and vapor pressures over the following condensed phases of the Sn-S system are explored in Piacente *et al.* [65] and Wiedermeier *et al.* [103]. Three vaporization equations explored by Piacente *et al.* are listed below [65]:

$$SnS_2(s) \rightarrow {}^1/_2Sn_2S_3(s) + {}^1/_4S_2(g) \tag{2.1}$$

$$Sn_2S_3(s) \rightarrow 2SnS(s) + {}^1/_2S_2(g) \tag{2.2}$$

$$SnS(s) \rightarrow SnS(g) \tag{2.3}$$

As written, Equation 2.3 can be termed as "congruent evaporation." Cadmium telluride (CdTe) is another common solar cell material that congruently evaporates. However, for this material, the Cd vapor and Te vapor evaporate independently and their pressures are measured separately as P_{Cd} and P_{Te}. At the evaporation temperatures used during production, Cd and Te have the same vapor pressures, P_{Cd} and P_{Te}. It is indicated by Equation 2.3, that SnS sublimates as an SnS *dimer molecule*, thus easily maintaining stoichiometry. Partial pressure, P_{SnS}, is therefore related to the deposition rate during thermal evaporation.

CdTe is one of the cheapest solar cell materials currently produced on the market. In 2014, First Solar's estimated cost is \$0.57 per watt or \$72/m^2. One of the reasons for their low cost is the deposition method used: close-spaced sublimation (CSS). This is a high speed, high temperature, fast deposition rate method where the source and substrate are within millimeters of each other. This method takes advantage of the

fact that CdTe also congruently evaporates and stoichiometry is easily maintained.

Should the efficiency of SnS solar cells become high enough for commercial production of solar cells, close-spaced sublimation would be a prime candidate for industrial scale production. It could leverage a large body of industry knowledge already established for CSS of CdTe.

2.2.2 SnS powder pre-treatment

Examining Equations 2.1 and 2.2, it is also seen that heating of Sn_2S_3 and SnS_2 releases sulfur vapor, or $S_2(g)$. During thermal evaporation, this excess sulfur would end up in the SnS film, possibly creating sulfur-rich phases. It has also been found by XRD that many commercially purchased SnS powders (e.g. from Alfa Aesar and Testbourne Ltd) are in fact Sn_xS_y powder, or a mixture of SnS, Sn_2S_3, and SnS_2 phases. Putting such a purchased powder into a thermal evaporation chamber may lead to a sulfur-rich film with an uncontrollable sulfur content. Upon first heating, the powder typically releases a large amount of sulfur gas, as the Sn_2S_3 and SnS_2 phases decompose into $SnS(s)$ and $S_2(g)$.

An analysis of XRD data (black curve, Figure 2-11) from Alfa Aesar $\geq$ 99.5% purity metals basis (Lot K17U030) SnS powder reveals a phase mixture of approximately: 43 % SnS, 55 % Sn_2S_3 and 2 % of SnS_2. This analysis was a semi-quantitative analysis by normalized RIR (Relative Intensity Ratio) method, performed in HighScore Plus.

To obtain phase pure powder, it is annealed at 500 °C for 1 hour in vacuum (approximately 15 mtorr base pressure). Figure 2-11 shows that this is enough time to allow all observed sulfur-rich phase peaks to decrease below the detection limit of XRD. Various times and temperatures, such as 400 °C and 450 °C and 3 or 15 min were also tried. The more effective annealing treatments are shown. After 500 °C for 1 hour (blue curve), no peaks from the Sn_2S_3 or SnS_2 phases are observed. The sensitivity of this XRD measurement puts an upper limit of 0.2 % on the Sn_2S_3 phase fraction.

SnS powder purchased from Sigma Aldrich (Lot MKBK7886V) does not initially

show any sulfur-rich phase contamination by XRD analysis. However, the pre-anneal treatment is still performed, to reduce sulfur content that may be below the detection limits of XRD and also to reduce process variability. After Sigma Aldrich (purity $\geq$ 99.99 %) powder is annealed at 500 °C for 1 hour in vacuum, it is loaded into the thermal evaporator crucible. Depositions of SnS are then repeatable until the powder is expended, leaving a small amount of SnO_x powder in the bottom of the crucible.

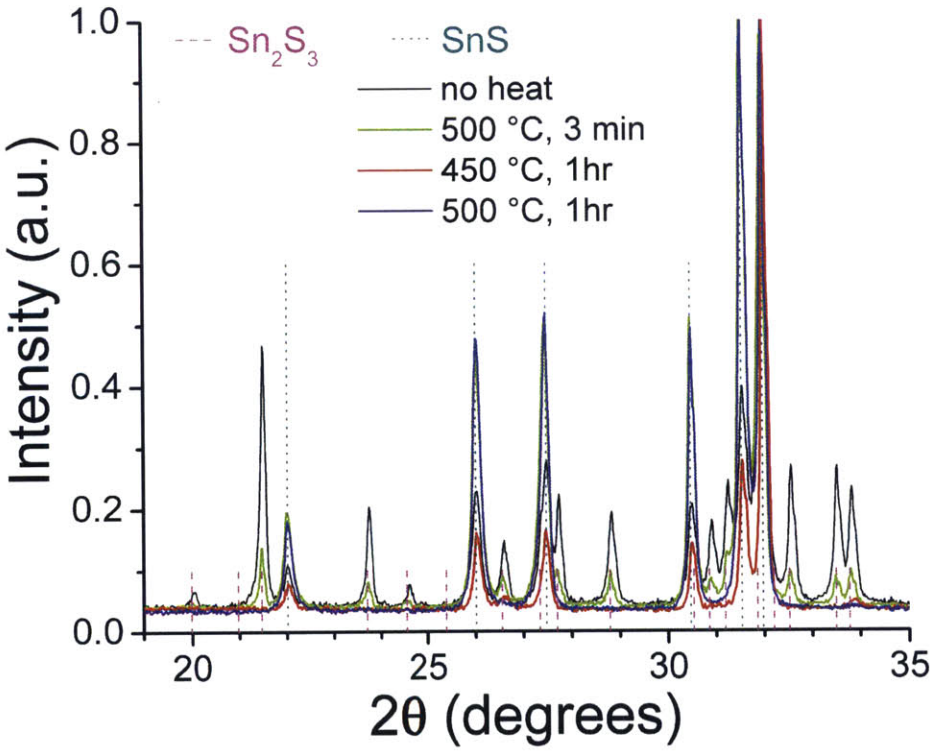

Figure 2-11: XRD data for untreated Alfa Aesar Sn_xS_y powder is plotted in black. Significant contamination by Sn_2S_3 is observed (PDF card # 04-007-0816 – magenta, long dashes). The Sn_2S_3 peaks become weaker with various heat treatments, such as annealing at 500 °C for 3 min (green), or 450 °C for 1 hour (red), or 500 °C for 1 hour (blue). After annealing at 500 °C for 1 hour, the XRD pattern matches only with SnS PDF card # 00-039-0354 (teal, short dashes), indicating phase pure powder.

2.2.3 Film deposition

Conditions for a "standard deposition" of SnS thin films are listed in Table 2.3. Common substrates are silica (Corning Eagle XG glass or a silicon wafer with a grown thermal oxide) and molybdenum (a thin film deposited onto Corning XG glass or silicon/SiO_2. Silicon wafers with a thermal oxide are are mostly used because the oxide surface is cleaner than the glass surface. Wafers are coated in photoresist to protect against dust, then diced into the appropriate size (1" × 1" for devices or 8.17 mm × 8.17 mm for film studies). Substrates are then sonicated in warm (65 °C) DI water, then twice in acetone, once in ethanol, once in IPA, then dried with an N_2 gun. Each solvent bath is also heated by a 65 °C external water bath. During the cleaning and drying process, substrates are held in custom-made quartz boats. Substrates are used immediately or stored in an N_2 glove box. After samples are deposited, they are again stored in an N_2 glove box until further processing.

Molybdenum thin films are deposited on Si/SiO_2 substrates using a two-layer technique. The first layer is an adhesion layer and the second is a conductive layer [77]. The film is typically 750 nm thick. $Si/SiO_2/Mo$ substrates are also stored in an N_2 glove box until SnS is deposited on them. No further cleaning of the Mo thin film is performed before depositing SnS.

Parameter	Value
Base pressure (torr)	$\leq 1 \times 10^{-7}$
Substrate temp (°C)	240
Source temp (°C)	550–620
Deposition rate (Å/s)	1
Source-to-substrate distance (cm)	10
Rotation (rpm)	8

Table 2.3: Typical SnS thermal evaporation parameters. These are referred to as "standard deposition" parameters.

2.2.4 Typical film results

Depending on the length of the deposition, films range between 500–1000 nm thick. A thickness of 1000 nm is enough to absorb 83 % of above band gap light that hits

the film. Films 100 nm or less tend to be a dark brown/red in color and slightly transparent. Films thicker than 100 nm tend to be dark to light gray.

Grain morphology and orientation

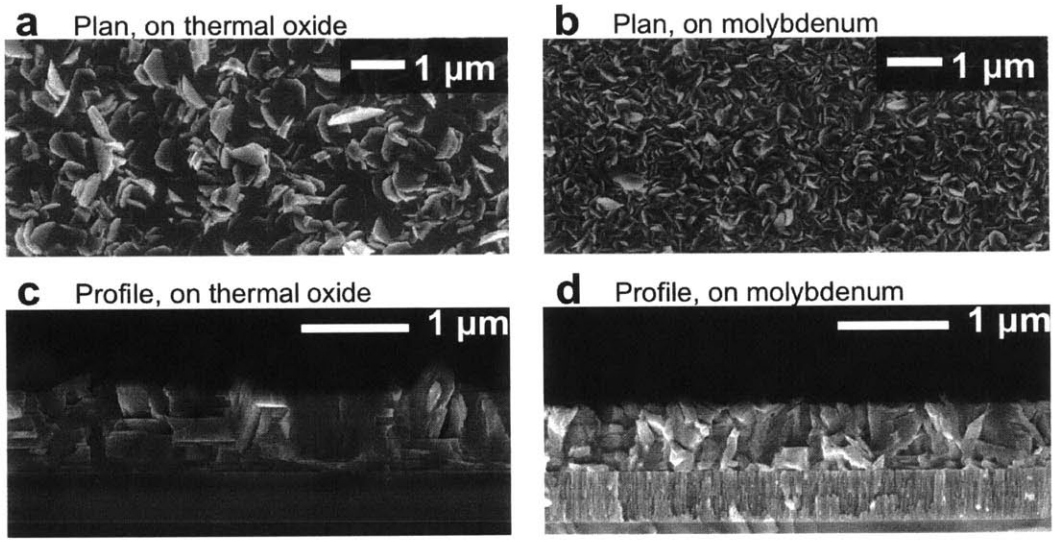

Figure 2-12: SEM images of thermally evaporated SnS on thermal oxide (a,c) and molybdenum (b,d). Films were deposited using the parameters listed in Table 2.3.

Plan and profile SEM images of a typical SnS thermally evaporated film with the aforementioned parameters (Table 2.3) are shown in Figure 2-12 for a Si/SiO_2 substrate and a $Si/SiO_2/Mo$ substrate. As-deposited grains tend to have a plate or slab-like structure, which leads to poor packing during growth, as grains start to impinge on each other. This slab-like shape is similar to the Wulff construction for SnS [91] and is derived from its orthorhombic crystal structure.

The profile images show that the slab-like shape of the grains yields considerable roughness, on the order of $\sigma_{\text{rms}} = 20 \pm 2$ for SnS on Mo substrates, based on AFM scans. This roughness can cause coverage issues for directional deposition methods, such as thermal evaporation.

XRD data taken in the Bragg-Brentano geometry for SnS on thermal oxide and Mo is shown in Figure 2-13. The dominant orientation varies significantly depending on substrate and may account for some difference in apparent roughness. Films are

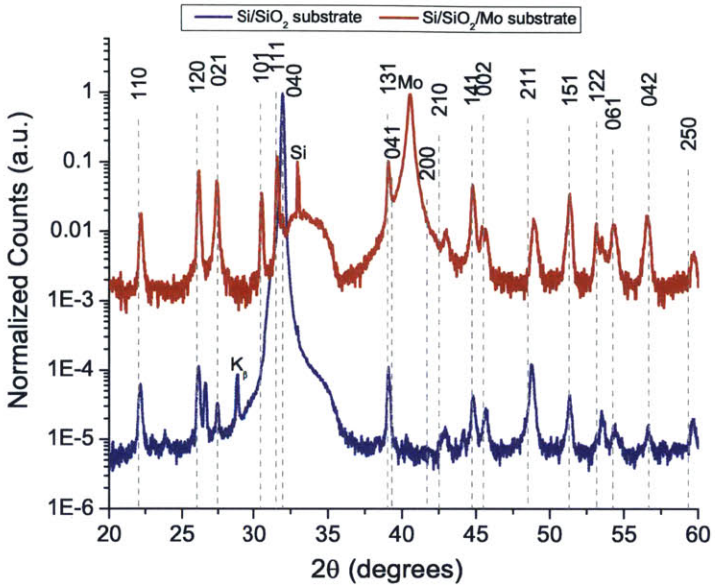

Figure 2-13: Normalized XRD data for thermally evaporated SnS films on Si/SiO_2 (blue) and $Si/SiO_2/Mo$ (red). The patterns match closely with SnS phase (JCPDS card # 00-039-0354), shown in gray. SnS on thermal oxide shows a strong preference for the (040), basal plane, orientation. SnS grown on Mo shows a much weaker preferred orienation, although the (111) direction is dominant.

phase pure and match JCPDS card # 00-039-0354. SnS films grown on thermal oxide tend to have a strong basal plane orientation (040) which are aligned parallel to the substrate. SnS on Mo shows a much weaker preferred orientation, although the (111) direction is often dominant.

TEM images of an as-deposited SnS film (by thermal evaporation) clearly show many defects within the grains and also extending from the Mo back contact layer. Figure 2-14a shows a profile of an SnS film grown on molybdenum. The two layers of the molybdenum deposition are easily seen. Above it, highly defective SnS material is observed, with some defects extending from the molybdenum into the SnS. Figure 2-14b is a higher magnification TEM image of the same material. It highlights the many kinds of structural defects present, such as stacking faults, twin boundaries, dislocations and grain boundaries (TEM sample preparation and imaging were performed by Austin Akey).

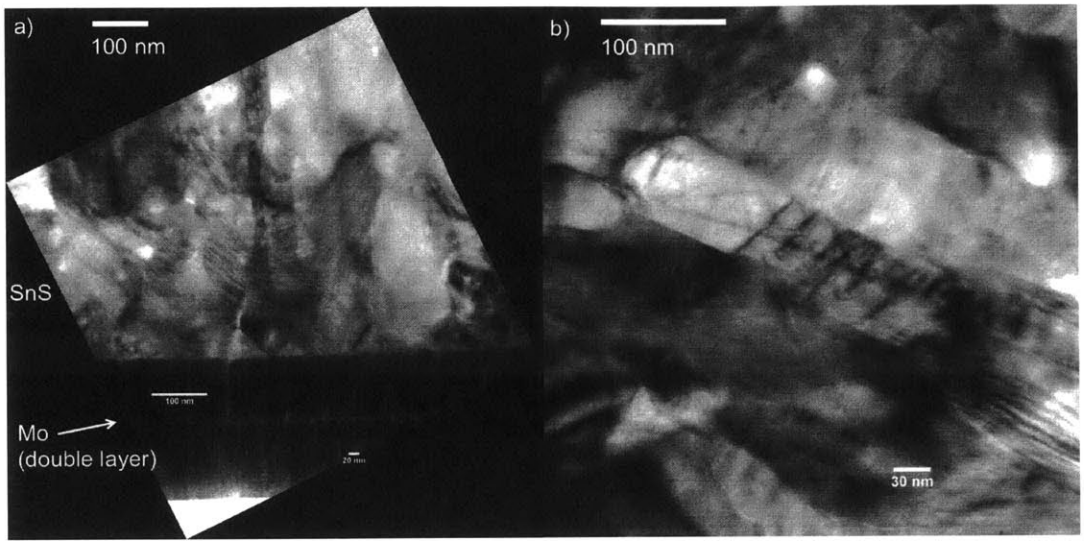

Figure 2-14: TEM images of as-deposited SnS by thermal evaporation. a) SnS/Mo interface is shown. SnS layer contains many defects, some of which begin in the Mo layer and continue into the SnS layer. b) a higher magnification image of the SnS film, showing many structural defects, such as stacking faults, twin boundaries and dislocations. Sample prepared by focused ion beam milling (FIB) and imaged by Austin Akey.

Electrical and optical

Films on thermal oxide tend to have a resistivity of 100–300 Ω-cm, a *p*-type carrier concentration range of 1–6 $\times 10^{15}$ cm^{-3} and a mobility range of 7–15 cm^2/Vs, as measured by van der Pauw and Hall technique, using a square sample with 20 nm Ti/ 200 nm Au contacts in the corners. An average of 6 standard deposition samples with a typical thickness of 1000–1200 nm on thermal oxide yielded an average majority carrier concentration of 4.2×10^{15} cm^{-3}, average majority carrier mobility of 9.2 cm^2/Vs, and average resistivity of 193 Ω-cm. Typical Hall data is shown in Figure 2-15. Hall measurements for as-deposited films tended to be difficult to measure and tended to show as-yet unexplained temporal changes in resistivity.

The absorption coefficient for as-deposited SnS thin films is calculated using Equation 2.4 from transmission and reflection data on two films (425 nm and 97 nm thick), grown on Corning Eagle XG glass. α vs. energy is plotted in Figure 2-16a. This data is a combination of α at the lower energies, measured from the thinner 97 nm film and

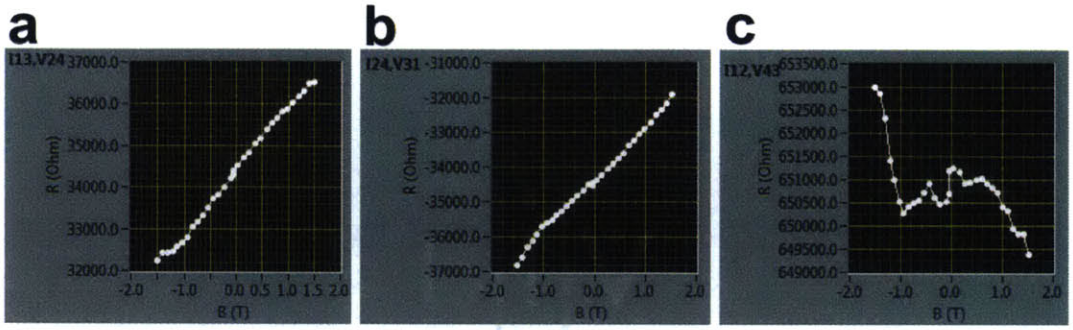

Figure 2-15: Hall measurements for an as-deposited SnS thin film. a) and b) show data for two cross-configuration Hall channels. Data is approximately linear, although some non-linear effects are seen. Panel c) shows these non-linear effects, which is a change in resistance of the sample as magnetic field changes (as measured through a van der Pauw channel).

α at the higher energies, measured from the 425 nm film. The two films had a deposition rate of 8 Å/s and a substrate temperature of approximately 300 °C. The typical band gap is 1.3 eV direct (Figure 2-16b) and 1.1 eV indirect (Figure 2-16c), derived similarly as in Chapter 2.1.1. (Data collection and analysis by Jeremy Poindexter, Raf Jaramillo, Riley Brandt and Max Powers).

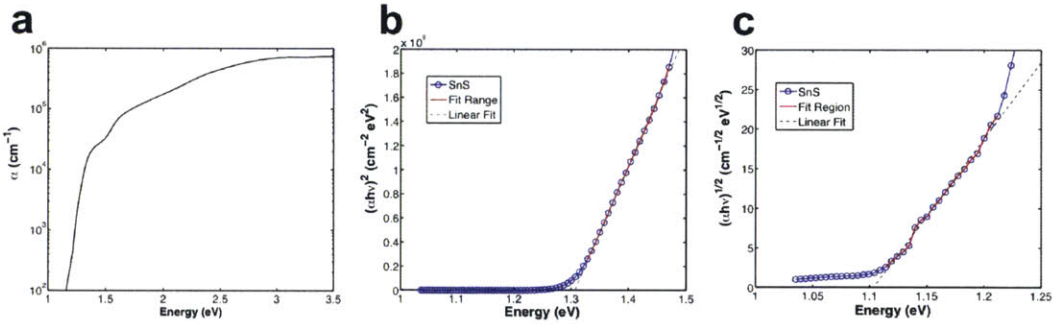

Figure 2-16: Optical data for SnS as-deposited films. a) Transmission and reflection data from two SnS films were measured and absorption coefficient was determined. b) The direct band gap is determined to be 1.3 eV using a plot of $(\alpha h\nu)^2$ vs. photon energy. c) The indirect gap is estimated to be 1.1 eV using a plot of $(\alpha h\nu)^{\frac{1}{2}}$ vs. photon energy.

$$\alpha = \frac{1}{d} \ln \left(\frac{1 - R}{T} \right) \tag{2.4}$$

2.3 SnS solar cells by thermal evaporation

2.3.1 Stack design

The typical stack used for SnS solar cells is described in Sinsermsuksakul *et al.* 2013 [86] and shown in Figure 2-17. Molybdenum was chosen because it is a common back-contact material for chalcogenide solar cells. Transmission line experiments also suggest molybdenum is an Ohmic contact material for SnS.

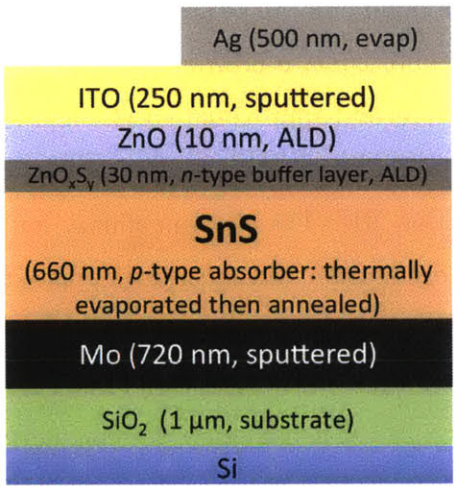

Figure 2-17: A standard SnS solar cell stack was established to be: Si (substrate) / SiO_2 (1 μm) / Mo (720 nm) / SnS (500–1000 nm) / ZnO_xS_y (30 nm) / ZnO (10 nm) / ITO (250 nm) / Ag (500 nm)

The thickness of the SnS absorber layer deposited by thermal evaporation typically ranges from 500 nm to 1000 nm, while the buffer layer (atomic layer deposition, ALD) was optimized to be 30 nm thick with a 10 nm ZnO layer on top. Above that 250 nm of ITO is deposited by RF sputtering, with 500 nm thick silver fingers deposited by e-beam evaporation for metallization. The current finger pattern contains a 1 mm by 1 mm square pad for a double-tipped probe contact (copper-beryllium alloy) and two 25 μm wide fingers. The spacing on the fingers was selected based on the spot size of a Xenon lamp used in quantum efficiency measurements. This allows quantum efficiency measurements to be taken without the deleterious effect of reflection from the silver fingers. The total area of the cell is defined by the area of ITO deposition,

and is nominally 25 mm^2, or 8 mm by 3.3 mm [90].

2.3.2 Buffer layer design and optimization

A ZnO_xS_y buffer was selected for its optimal conduction band alignment. Thin film mixtures of ZnO and ZnS create phases that have a varying range of conduction band minimums (CBM), valence band maximums (VBM) and band gap [86, 61, 64], depending on the amount of sulfur or oxygen content. Figure 2-18 shows the extent to which the conduction band minimum can be adjusted, according to sulfur content [64]. This figure also plots the approximate positions of the SnS conduction and valence bands, relative to vacuum level and approximate position of the ZnO conduction band. In the figure, the electron affinity (χ) used for SnS is that of the (100) orientation, or the basal plane orientation [91]. The electron affinity for ZnO also varies slightly, depending on the surface orientation, but a common approximate value is used here.

If ZnO were used as the buffer layer material, the band alignment with SnS would create a Type II cliff structure and any device should suffer from poor V_{OC} [43]. As the sulfur content of the ZnO_xS_y layer is increased, the conduction band minimum shifts up (smaller electron affinity). When the layer becomes pure ZnS, the *p-n* junction becomes a Type II current-blocking structure. In this scenario, one expects to see a strong drop in J_{SC}, because the ZnS would block the flow of electrons out of the SnS toward the top contact. Somewhere between the ZnO and ZnS material is a mixture with an ideal band alignment. If the conduction band minimum of the ZnO_xS_y is slightly above the CBM of the SnS, a spike structure is created ($\Delta E_{CBM} = \chi_{SnS} - \chi_{ZnO_xS_y} < 0.4\,eV$). A small spike can be beneficial because it blocks recombination at the interface [53], however a large spike ($\Delta E_{CBM} > 0.4\,eV$) can cause current-blocking and reduce J_{SC}.

The ZnO_xS_y buffer layer and ZnO capping layer are grown by ALD by the Gordon Group at Harvard. With ALD, the composition of the ZnO_xS_y buffer layer can be tailored for optimum efficiency by adjusting they cycle ratio of ZnO:ZnS.

It has also been found that nitrogen doping of the ZnO_xS_y can reduce carrier concentration and can also have an efficiency-boosting effect. In particular the nitrogen

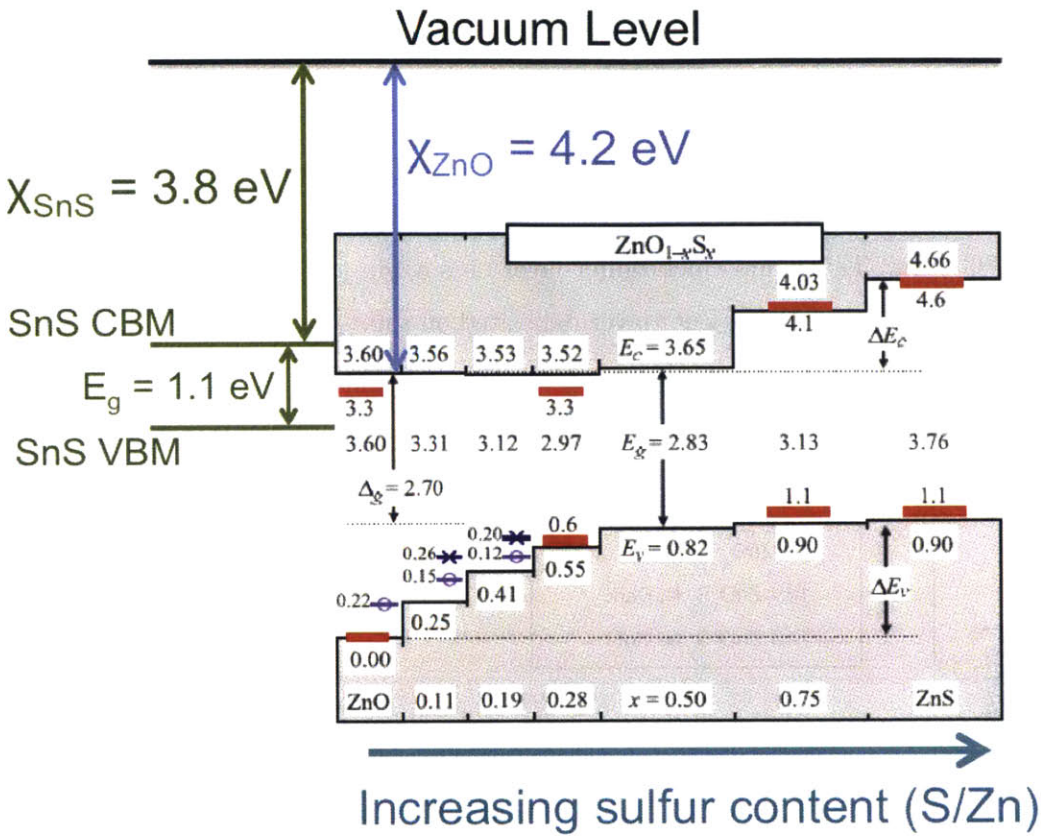

Figure 2-18: Diagram illustrates the change in band gap (smaller, then larger again) as a ZnO film increases sulfur content until it is a ZnS film. The conduction band minimum is also observed to shift up (also stated as a decreasing electron affinity). Left side plots approximate position of SnS conduction and valence band edges, for comparison to ZnO_xS_y buffer layer positions. The SnS CBM and VBM positions are drawn from the approximate electron affinity levels (χ) of SnS and ZnO. However, for both materials, the electron affinity changes depending on crystal orientation. Image modified from [64].

doped 14:1 cycle ratio often has the best performance. This buffer layer has a S/Zn atomic ratio of 0.14 and N/Zn atomic ratio of 0.05, as measured by RBS. [88]

2.3.3 Results

Initial SnS solar cells produced by thermal evaporation, using an ALD-deposited ZnO_xS_y buffer layer had a typical efficiency range of 1.6 to 3.0 %. An optimum buffer layer of ZnO_xS_y with a cycle ratio of 14:1 with nitrogen doping, was found by

depositing a range of different S/Zn buffer layer compositions and nitrogen doping compositions.

Two typical thermally evaporated SnS cells are shown in Figure 2-19. The red line shows a cell with a 650 nm thick SnS layer deposited with a rate of 0.8 Å/s. This SnS layer had a passivating SnO_x layer added by annealing in air for 30 minutes in a 200 °C oven. The 30 nm thick buffer layer uses a 14:1 cycle ratio, nitrogen doped ZnO_xS_y layer with a 10 nm ZnO layer deposited on top.

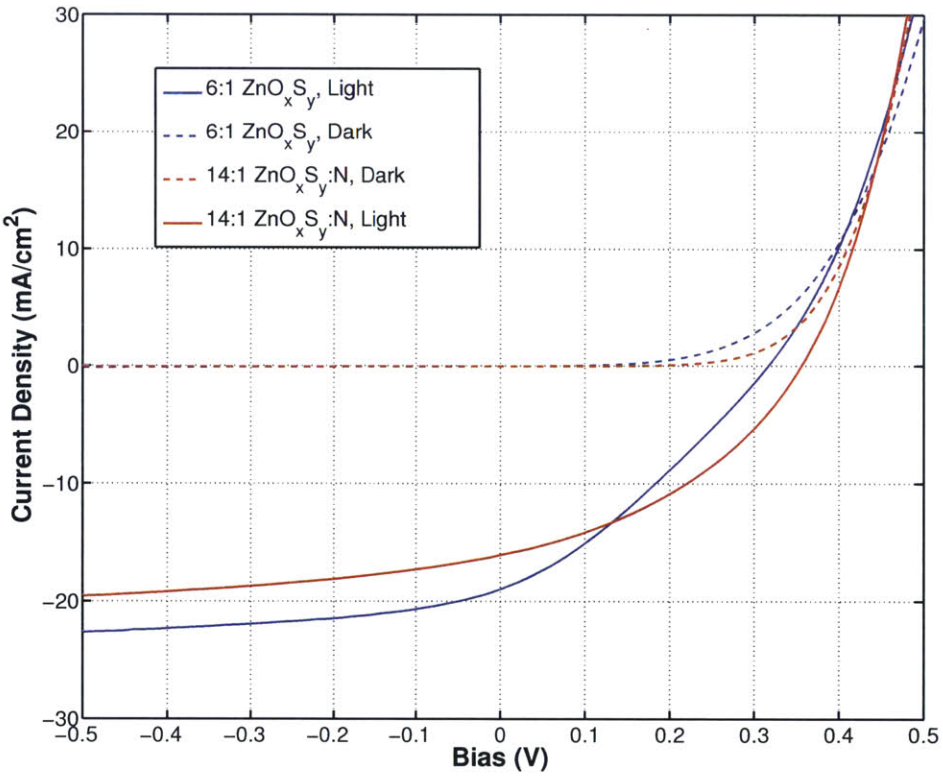

Figure 2-19: JV curves are shown for two as-deposited SnS solar cells. The blue dashed and solid curves show a typical best cell with an air-exposure generated passivation layer and a 6:1 cycle ratio ZnO_xS_y buffer layer. The red curves (dashed and solid) show a best cell with a heat-generated SnO_x passivation layer and a nitrogen-doped 14:1 ZnO_xS_y buffer layer.

The blue line shows another typical cell with a different passivation method and buffer layer composition. The SnO_x layer is created by exposure to air for 20 hours,

Parameter	6:1 ZnO_xS_y (blue)	14:1 ZnO_xS_y:N (red)
Efficiency (%)	1.84	2.19
V_{oc} **(mV)**	316	355
J_{sc} **(mA/cm²)**	19.0	16.1
Fill Factor (%)	30.7	38.5
R_{series} **(Ω) cm²**	3.34	0.94
R_{shunt} **(Ω cm²)**	308	943

Table 2.4: A comparison of vital solar cell statistics for two thermally evaporated SnS solar cells with different buffer layer compositions and passivation layer methods.

and the 30 nm thick buffer layer composition uses a cycle ratio of 6:1 for the ZnO_xS_y layer with no nitrogen doping, then a 10 nm thick ZnO layer is again deposited by ALD. The 6:1 cycle ratio leads to a ZnO_xS_y film with a S/Zn atomic ratio of 0.5 [60]. Without nitrogen doping, the buffer layer majority carrier concentration is estimated to be approximately $[n] = 10^{19}$ cm^{-3} [60], although this was measured for a 100 nm thick film. The films are currently suspected to be light-sensitive, with a changing resistivity and carrier concentration with different thickness and upon light exposure. Measured and calculated solar cell parameters are shown for comparison in Table 2.4.

Cells with the nitrogen-doped 14:1 ZnO_xS_y buffer layer have been found to consistently have higher efficiency. An air-exposed passivation layer has also been preferred, because the 200 °C anneal in air can some times over-oxidize the SnS layer, leading to a strong drop in J_{SC} due to current-blocking. Additionally, a "double-diode" effect can be seen in the blue (light) curve in Figure 2-19, leading to a poor fill factor. This behavior is less frequently observed when the nitrogen-doped 14:1 ZnO_xS_y buffer layer is used.

A cross-section SEM image of a thermally evaporated SnS device is shown in Figure 2-20. The back contact molybdenum layer is visible, as is the SnS layer and the ITO layer. The buffer layer(s) is too thin to be visible between the SnS and ITO. One observes that the as-deposited SnS grains in this device are not equiaxed and perhaps not columnar or through-thickness either.

Figure 2-20: SEM cross-section of a typical SnS solar cell. Glass is visible at the bottom, then Mo, SnS and ITO. The ZnO_xS_y/ZnO buffer layer is not visible between the SnS and ITO.

Comparison to ALD-grown SnS devices

SnS grown by ALD and thermal evaporation have shown very similar results [86]. ALD-grown SnS devices were reported in Applied Physics Letters with a record efficiency of 2.04 %. These films were the first to use a mixed composition ZnO_xS_y/ZnO buffer layer. The SnS layer was 1.5 μm thick and had no annealing or SnO_x passivation step. Figure 2-21a shows two devices with two different buffer layer compositions. Figure 2-21b shows the NREL certified device and parameters.

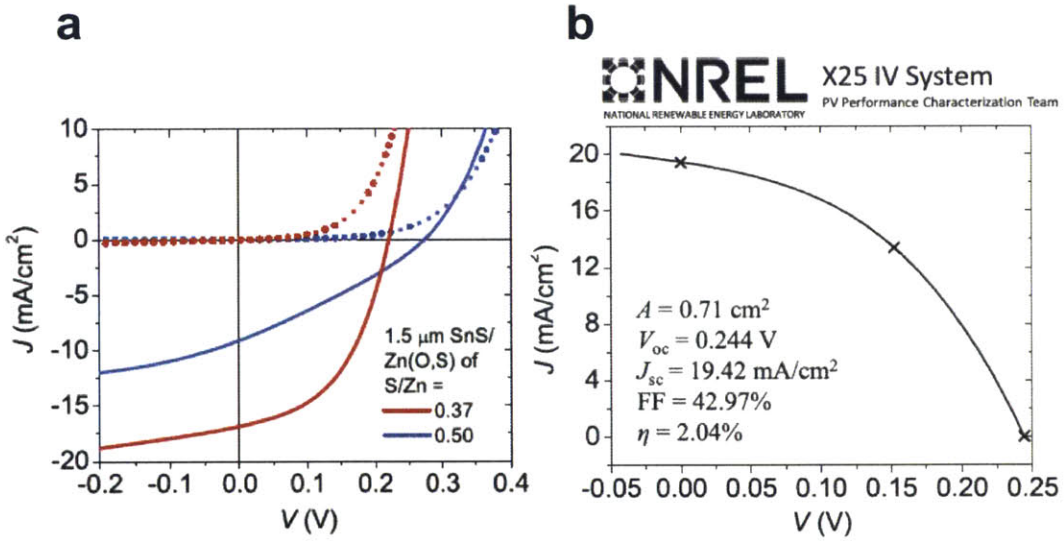

Figure 2-21: SnS solar cells grown by ALD demostrate the effectiveness of the ZnO_xS_y buffer layer (a). It is shown that a buffer layer with a S/Zn atomic ratio of 0.37 is most effective for ALD-grown SnS devices. A new record for SnS is set, with the NREL-certified cell shown in (b). These ALD films were grown with a substrate temperature of 200 °C and were not annealed. Image from [86].

Chapter 3

Motivation for annealing SnS

While annealing has been mentioned in the SnS literature, it has not been frequently met with success. Various gaseous atmospheres have been tried, such as air (O_2/N_2), pure nitrogen, argon and sulfur-containing (both H_2S and evaporated sulfur gas). Annealing has been observed to increase grain size and adjust carrier concentration, which is common of many annealing steps in laboratory and industry processes. The change in majority carrier concentration suggests a dependence on a particular defect, which is impacted during annealing. The exact cause of the change in defect behavior is often not known precisely. However, they are typically affected either by temperature, gaseous atmosphere, or both [17]. It is clear that the area is ripe for exploration and optimization.

An as-deposited SnS thin film, made by RF sputtering or thermal evaporation, can make an operational solar cell (seen in Figure 2-19), but there is much to be improved about these films, leading to increased efficiency. Below is a list of film properties that can be modified by annealing and in this chapter we will discuss why each property is important.

1. Phase
2. Grain morphology (or grain boundary density)
3. Majority carrier concentration
4. Mid-gap intrinsic point defects

The above film properties are important because of how they impact solar cell device parameters. More broadly, points 1 and 2 can be considered structural defects. The presence of another phase can change absorption characteristics, create recombination at the interface of two phases, change carrier concentration, etc. But even in the absence of another phase, grain boundaries in solar cells are often detrimental.

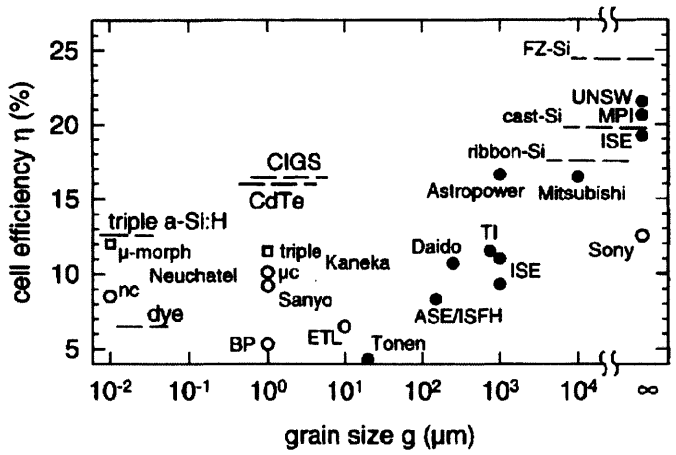

Figure 3-1: Cell efficiency vs. grain size for silicon technologies. The general correlation shows that as grain size in silicon wafers gets larger, the efficiency tends to increase as well. Image from Bergmann *et al.* [11].

Figure 3-1 shows a correlation of cell efficiency vs. grain size in silicon solar cells. Generally, smaller grains lead to lower efficiencies. This usually happens because grain boundaries tend to be recombination active, which lowers minority carrier lifetime. Grain boundaries also increase the number of scattering sites for carriers, which reduces carrier mobility. Recombination also leads to an increased dark current (I_0), which reduces V_{OC} according to the following equation:

$$V_{\mathrm{OC}} = \frac{Ak_{\mathrm{B}}T}{q} \ln\left(\frac{I_{\mathrm{L}}}{I_0} + 1\right) \tag{3.1}$$

where A = ideality factor and I_{L} = illuminated current.

Points 3 and 4 are broadly related to intrinsic point defects. Majority carrier concentration is believed to be caused by the doubly-ionized tin vacancy ($\mathrm{V}''_{\mathrm{Sn}}$). Thus controlling the number and ionization state of this defect will impact $[p]$, or N_{A}. An

increase in N_A, to a certain level (before Auger recombination becomes predominant), will also increase V_{OC} according to the following:

$$V_{OC} = \frac{Ak_BT}{q} \ln\left(\frac{(N_A + \Delta n)\Delta n}{n_i^2}\right) \tag{3.2}$$

where n_i = intrinsic carrier density, N_A = acceptor (or doping) density, and Δn = excess carrier concentration upon illumination.

Mid-gap states can also increase Shockley-Read-Hall recombination, thereby reducing carrier lifetime and mobility, if found in high enough concentrations. Some DFT point-defect calculations find the sulfur vacancy ($V_S^{\bullet\bullet}$) lies mid-gap. The impact of this prediction will be discussed later in the chapter.

Points 1–4 all have some effect on minority carrier mobility or minority carrier lifetime. These two material parameters ultimately impact the collection length in a solar cell device: $L \propto \sqrt{\mu\tau}$. If minority carrier mobility and lifetime can be improved by annealing, we should see this improvement through increased device efficiency. While some increase in in V_{OC} is possible, we will most likely see an improvement in J_{SC}. As the minority carrier diffusion length improves, fewer carriers are lost before they are collected, leading to a direct improvement in J_{SC}.

In heterojunctions, V_{OC} and efficiency can also be improved by finding an optimal n-type band alignment for the p-type absorber layer. Because this is a property of the buffer layer, not the absorber, this topic is not explored in this thesis. The topic of buffer layers and band alignment is a promising and active area of research. For this study, a single buffer layer composition is used for all experiments and it is assumed that this is an "optimal" buffer layer. In reality, the optimal buffer layer for a high-efficiency SnS cell has not yet been found.

Several exploratory experiments designed to test initial annealing conditions were performed first and are discussed below. These results were used to decide which parameters of annealing seem most promising to pursue.

3.1 Preliminary annealing experiments on RF sputtered films

Initial experiments on RF sputtered SnS films were performed. These experiments were designed to test the large parameter space of annealing thin films. There are several reports of SnS annealing in vacuum, air, and sulfur environments [70, 72, 106]. Some of these were replicated to see which directions might be most promising.

3.1.1 *In-situ* annealing: Results and discussion

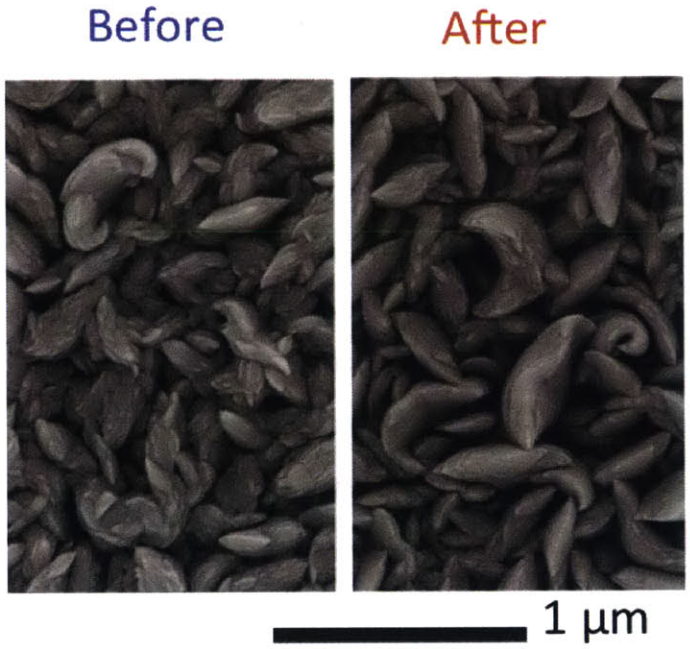

Figure 3-2: Left: Plan-view SEM of an SnS film sputtered at 201 °C. Right: Plan-view SEM of an SnS film sputtered at 201 °C and then *in-situ* annealed at 201 °C for 1 hour.

An RF sputtered SnS thin film, deposited at 201 °C was allowed to remain in the sputtering chamber at 201 °C for 60 minutes. No argon gas was flowing into the chamber and the base pressure remained at or below 4.6×10^{-6} torr. This was effectively an anneal in vacuum. This film is compared to a prior deposition with the

same deposition conditions, but no annealing. The plan-view SEM image comparison is shown in Figure 3-2. After the *in-situ* anneal, the Sn/S ratio is observed to shift slightly from 0.79 to 0.82. This is a small shift and is within the error of the WDS measurement. The resistivity shifted from 7.3 Ω-cm (as-deposited) to 9.6 Ω-cm (annealed).

Grain morphology is observed to change slightly. There appear to be fewer small grains, perhaps due to coarsening. Grain size did not change significantly and porosity seems to have increased slightly. The appearance of intragranular nanocrystallites is also diminished after the *in-situ* anneal.

Overall, it appears there is limited impact of *in-situ* vacuum annealing at 201 °C. Both the temperature and the atmosphere of the anneal should change. However, other annealing equipment is needed to accomplish annealing at higher temperatures and in other ambients.

3.1.2 *Ex-situ* anneal in 4 % H_2S gas: Results and discussion

The *in-situ* annealed sample from the previous section was then *ex-situ* annealed in an ALD chamber at 400 °C for 60 minutes with a 4 % H_2S gas ambient. The plan-view SEM images are shown in Figure 3-3. Several other as-deposited samples were also annealed at the same time. The SEM images show subtle differences in grain morphology, primarily increased porosity. There are slight increases in grain size and resistivity from 9.6 to 17.3 Ω-cm. Stoichiometry shows a more significant change, from Sn/S = 0.82 to 1.03. Two other films deposited with similar parameters, but not *in-situ* annealed, showed similar changes in stoichiometry after the *ex-situ* anneal. Both films were Sn-poor but became approximately stoichiometric (Sn/S ratio = 1.02 and 1.06). This suggests that H_2S may strongly impact stoichiometry but may not alter grain morphology. The combination of increased porosity and increased Sn/S ratio may also suggest that these annealing parameters encourage the evaporation of the Sn_2S and Sn_2S_3 phases, thus pushing the film to a more stoichiometric value. At this stage it is impossible to tell if this effect is due to the presence of H_2S or the higher annealing temperature.

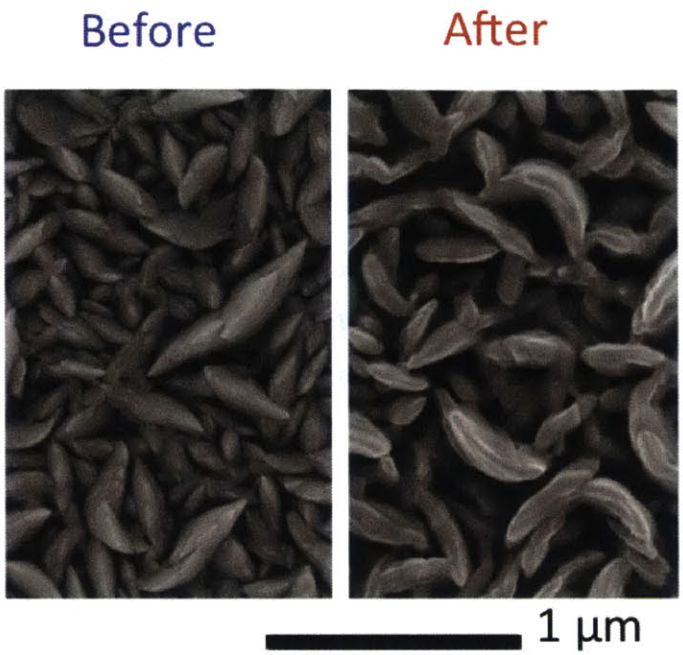

Figure 3-3: *Ex-situ* anneal at 400 °C in 4 % H_2S gas in an ALD chamber. Left: (before) Plan-view SEM of an SnS film sputtered at 201 °C and further *in-situ* annealed at 201 °C for 1 hour. Right: (after) Plan-view SEM of the SnS thin film *ex-situ* annealed at 400 °C for 1 hour in 4 % H_2S gas.

It is also necessary to mention that this anneal was performed in an ALD deposition chamber. The H_2S gas flow valves operate in pulse mode, where the chamber is filled to a pressure of 10 torr, held constant for 5 minutes, then the chamber is pumped down over 10 seconds and refilled again with gas to 10 torr. This cycle repeats for the entirety of the anneal time. The ramp and cool profile of this furnace is also somewhat slow, on the order of 30+ minutes, for both the ramp and cool. This pulsing mode means that the film was not constantly exposed to H_2S at 10 torr. Extending these results to a normal flow (non-ALD chamber) furnace will be difficult.

3.1.3 *Ex-situ* anneal in 100 % H_2S gas: Results and discussion

An as-deposited amorphous SnS thin film, deposited by RF sputtering, was annealed in the ALD chamber at 400 °C for 90 minutes with a 100 % H_2S gas ambient at pressure of 1 torr (in pulsing mode). The Sn/S ratio of the as-grown film was 0.87 and after annealing was 1.00. Grain size increased significantly from amorphous (or grains smaller than 10 nm) to grains in the range of 40–200 nm diameter. Resistivity of the before and after films remained too high to measure by four-point probe. The plan-view SEM images and annealed sample XRD data is shown in Figure 3-4. The XRD peaks in the annealed sample match to α-SnS.

With the existing data, the observed grain growth cannot be attributed to any one factor. This is because the starting films were amorphous. Secondary grain growth (or re-crystallization) can happen more rapidly in amorphous films, as compared to films which begin with 200 nm grains. However, it is also observed that the Sn/S ratio tended towards stoichiometry during the annealing. Regardless, one still cannot say whether it is the elevated temperature or the exposure to H_2S gas that causes this change in crystallinity and stoichiometry.

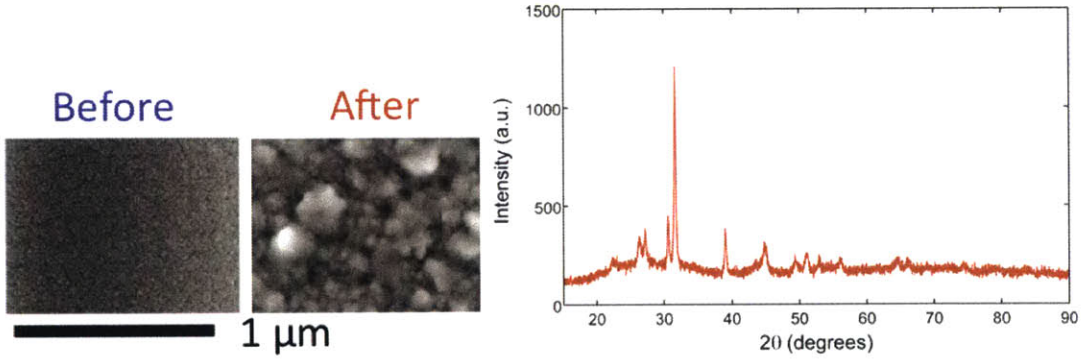

Figure 3-4: Left: Plan-view SEM of an SnS film sputtered at room temperature. The film is clearly amorphous, also supported by XRD data (not shown). Middle: Plan-view SEM of the amorphous SnS thin film after an *ex-situ* anneal at 400 °C for 1.5 hours in 100 %H_2S gas Right: XRD pattern for the annealed film shows crystalline peaks matching α-SnS.

3.1.4 Summary of preliminary experiments

From these few experiments, it is observed that films annealed with H_2S seem to attain phase purity as evaluated by WDS and XRD. While some of the porosity may be from sulfur loss, it is also possible that the total pressures used here (vacuum, 1 torr and 10 torr) and the cycling of gas pressure due to the ALD chamber may have also caused evaporation and material loss because the time-averaged total pressure and time-averaged sulfur partial pressure were too low.

It is apparent that 400 °C vs. 200 °C is more effective at grain morphology modification, although the effects of annealing are confounded by using an initially amorphous film. That higher temperature should impact grain size more effectively is to be expected. Grain growth tends to increase with temperature, due to increased atom mobility and diffusion [9].

3.2 Phase control

While the thermally evaporated SnS films show excellent phase purity, the RF sputtered films suffered from phase impurity. There were likely Sn_2S_3 and SnS_2 impurity phases present in the film. Preliminary annealing experiments in H_2S at 400 °C gas suggest these phases can be eliminated, due to a trend toward Sn/S = 1 stoichiometry after annealing.

Although no further annealing experiments with RF sputtered films were performed, it is still important to understand the Sn-S phase space as it relates to the temperature and pressures experienced during annealing. As phase-pure thermally evaporated films are annealed, it will be important to avoid formation of new sulfur-rich phases. Phase purity is a primary benefit of thermal evaporation when compared to RF sputtering. It would be unwise to lose this advantage during the annealing process.

Luckily, obtaining phase pure SnS films has been made easy by the decomposition reactions described by Piacente *et al.* [65]. The same principles that were applied to purify Sn_xS_y powder before thermal evaporation can be applied to thin films (Chapter

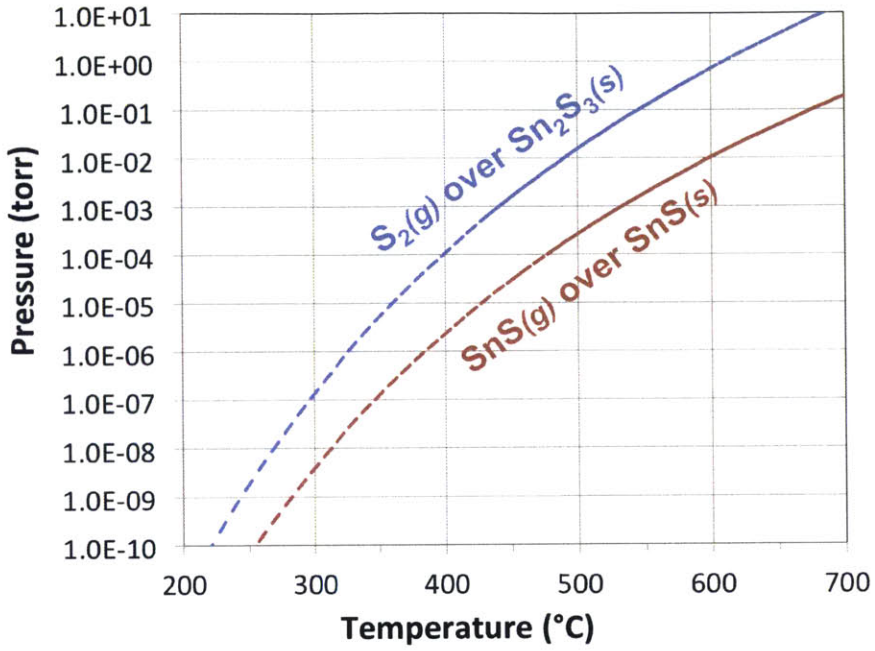

Figure 3-5: SnS and S_2 vapor pressure vs. temperature in Sn-S system. Solid lines represent the temperature range for which data used to write Equations 3.3 and 3.4 are valid. Dotted lines represent an extrapolation of these equations to a larger temperature range. Blue line plots the S_2 vapor pressure above Sn_2S_3 phase that is decomposing. Red line plots the SnS(g) vapor pressure above SnS(s) at a particular temperature.[65]

2.2.1). Both SnS_2 and Sn_2S_3 will degrade into SnS phase and release S_2 gas. SnS sublimates into gas phase SnS, although there are some reports that SnS can also lose sulfur vapor in small amounts [6, 19]. These reactions are described in Equations 2.1, 2.2, 2.3. Using data from Piacente *et al.*, listed in Equations 3.3 and 3.4, SnS gas pressure above SnS solid is plotted in Figure 3-5. For reference, the pressure of S_2 gas above decomposing Sn_2S_3 is also plotted. In the listed equations, P_{S_2} is in kPa, T is in Kelvin, and the heat of enthalpy is in kJ/mol.

$$\log_{10}(P_{S_2}) = (11.81 \pm 0.50) - \frac{(11.2 \pm 0.4) \times 10^3}{T}, \quad \Delta H^{\circ}_{298} = 112.0 \pm 2.0 \qquad (3.3)$$

$$\log_{10}(P_{\mathrm{SnS}}) = (9.40 \pm 0.10) - \frac{(10.7 \pm 0.1) \times 10^3}{T}, \quad \Delta H^{\circ}_{298} = 222.0 \pm 2.0 \qquad (3.4)$$

The blue line in Figure 3-5 is important because it describes the temperature and pressure of S_2 gas at which Sn_2S_3 breaks down into SnS and S_2. The reverse reaction is also possible at this temperature and P_{S_2}. This is when SnS, provided sulfur and high temperature, can turn into Sn_2S_3 phase. Crossing this line during annealing is to be avoided. This would convert SnS phase into Sn_2S_3 phase.

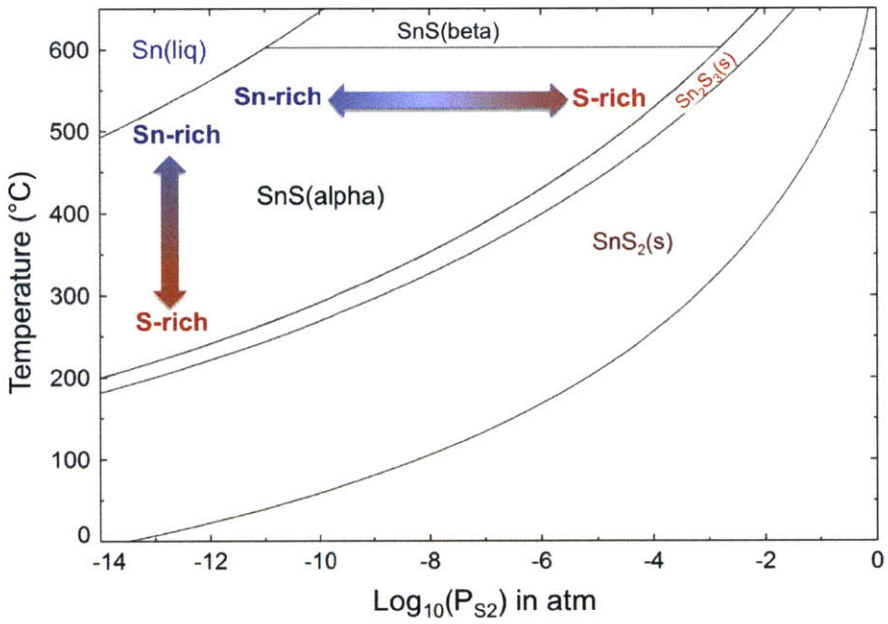

Figure 3-6: FactSage calculated Sn-S phase diagram. Temperature vs. P_{S_2} shows the existence regions for SnS(α), SnS(β), Sn (liquid), Sn_2S_3(s) and SnS_2(s). The blue/red arrows exhibits the space where stoichiometry could be modified to Sn-rich or S-rich.

A thermodynamic calculation software, FactSage, was used to further determine the phase space of the Sn-S system. Albers *et al.* 1961 plots a P vs. $1/T$ diagram for the Sn-S system [5], but more detailed phase space data is needed. Figure 3-6 shows an updated temperature vs. P_{S_2} phase diagram calculated by FactSage. The phase boundary between SnS and Sn_2S_3 is seen for various temperatures and sulfur partial pressures. From this diagram, one can determine the necessary sulfur partial

pressure to maintain while a SnS film is annealed at a particular temperature. The temperature and pressure must stay in the phase space to the left of the SnS/Sn_2S_3 phase boundary.

It must be stressed however, that Figure 3-6 is derived from thermodynamic calculations. Kinetics may still play a role in determining the phase of the annealed film.

It is hypothesized that a phase-impure film annealed at temperature and P_{S_2} conditions within the SnS(α) phase space, would become phase pure, as the other sulur-rich phases decompose during the anneal. An already phase-pure film annealed in conditions within the SnS(α) phase space should maintain phase purity. Shifting annealing conditions within this phase space should also adjust defect chemistry, discussed in Chapter 3.4. As one moves closer to the Sn(liq) phase space, the SnS material becomes more tin-rich. As one moves towards the Sn_2S_3(s) phase space, the SnS material becomes more sulfur-rich.

3.3 Grain morphology

Evaluating SEM and AFM data of as-deposited films (Figure 2-12), the surface roughness is pronounced and unusual when compared to CIGS or Si wafers [78]. Figure 3-7 shows a clearer view of the unusual surface features and protrusions observed in profile SEM.

Because the buffer layer is deposited by ALD, a highly conformal deposition method, the sharp protrusions are still likely covered in ZnO_xS_y. The impact of irregular shapes and protrusions on efficiency is suspected to be detrimental. Possibly causing shunts, areas of current crowding, or enhanced recombination due to the extended distance carriers in the bulk of the film might have to travel to reach the *p*-*n* junction. Surface roughness can also be beneficial for light trapping [12, 13], however these patterns are typically pyramidal in shape and densely packed, rather than flake-like and sparsely distributed, as seen in Figure 3-7.

Grain size has been difficult to determine or define, due to the anisotropic nature

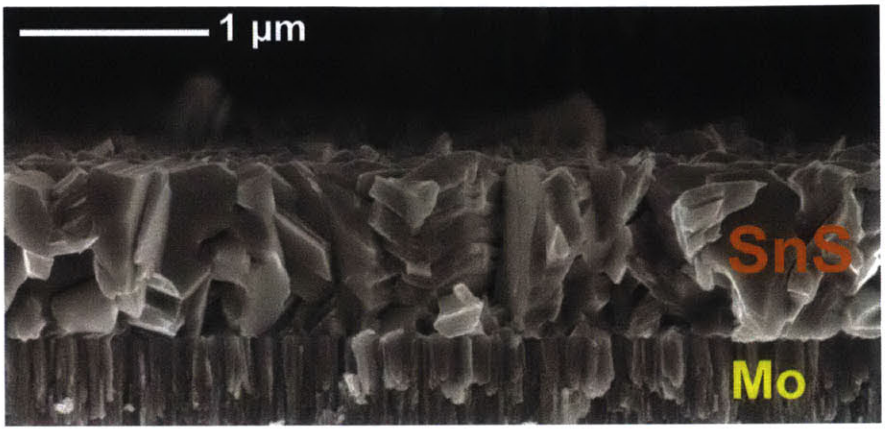

Figure 3-7: SEM profile view of as-deposited SnS (by thermal evaporation) on molybdenum. Note surface roughness and occasional grains in the background which protrude above the average suface plane height.

of the grains. XRD analysis for grain size is frequently confounded with micro-strain data, and also does not match the observed grain sizes (by SEM) even remotely. This is because the XRD-measured "grain size," as determined by line-width analysis and the Scherrer formula is more accurately described as a coherency length of X-rays in the crystal (or crystallite domain size). For SnS films, the XRD coherency length has always been smaller than the grain size/length observed in SEM, strongly suggesting the grains are defect-rich. The TEM images in Chapter 2.2.4 (Figure 2-12) also show a high density of defects in the SnS film. This supports the conclusion that grain size is not accurately determined by XRD line-width analysis. With so many defects, the XRD coherency length will be much smaller than the grain size observed by SEM.

Larger, columnar grains will likely increase the efficiency of SnS solar cells by reducing the density of structural defects (a.k.a. grain boundaries). A columnar or equiaxed grain structure is preferred, because electrons and holes, traveling through the thickness of the SnS film are less likely to encounter a grain boundary and recombine. Reaching an average grain diameter of 1 µm or larger would ensure an equiaxed structure for a 1 µm thin film. This size also makes other characterization methods easier, such as EBIC (electron beam induced current) or EBSD (electron backscatter diffraction).

3.4 Majority carrier concentration

Typical majority carrier concentrations for as-deposited SnS films have been in the range of $1\text{–}6 \times 10^{15}\,\text{cm}^{-3}$. With the proper buffer layer n-type carrier concentration, this can be an acceptable range for a solar cell. The "ideal" carrier concentration for the n-type layer is typically 1 or 2 orders of magnitude above that of the p-type layer, assuming there is an ideal 0.2 to 0.4 eV spike in the conduction band offset between the p-type absorber and the n-type buffer [53]. This difference between p and n-type populations creates an inversion layer in the SnS material, such that the electrical p-n junction (where Fermi level crosses mid-gap) is now in the SnS layer and not directly at the SnS/ZnO_xS_y interface. There are many defects at this interface and removing the junction from this area, even by a couple nanometers, can reduce recombination at the interface. The reduced recombination due to inversion is because the physical interface region is now in purely n-type environment, where there are fewer holes for the electrons to recombine with [53].

As one searches for other n-type buffer layer materials, the ability to control majority carrier concentration in the SnS layer becomes important. This control will allow us to optimize $[p]$ in SnS with a selected n-type buffer layer and associated carrier concentration. In our attempt to control majority carrier concentration, one should also understand the mechanisms by which one can alter the majority carrier concentration. Literature on the subject generally agrees that the p-type doping in SnS comes from tin vacancies (V''_{Sn}). However, there are multiple theories of how to treat intrinsic defects, discussed below.

3.4.1 Kröger-Vink defect theory applied to SnS

The single crystal studies carried out in the 1960s assume that SnS can be treated as an ionic material and apply defect chemistry principles, or Kröger-Vink theory [39] to derive a Brouwer diagram for SnS (seen in Figure 1-12 [71]). Such a model typically starts with an assumption of a dominant defect: Schottky (vacancy pair formation) or Frenkel (interstitial formation). None of the papers from the 1960s ever state an

assumption of dominant defect type, although there are efforts to try to fit the data using different assumptions.

As an exercise, let us assume that the dominant intrinsic defect is a Schottky vacancy pair and work through the defect equilibria formalism using Kröger-Vink notation ($X^{\bullet}$ = positive charge, X' = negative charge). The principle of defect equilibria theory is that the generation of defects are treated as chemical reactions, which must also maintain mass and charge balance. We assume there are no significant solutes or extrinsic impurities.

The equilibrium constant (K) for any reaction can be written as in Equation 3.5. This will be applied to each defect reaction.

$$K = \exp\left(\frac{-\Delta g}{2k_{\mathrm{B}}T}\right) \sim \exp\left(\frac{-\Delta h}{2k_{\mathrm{B}}T}\right) \tag{3.5}$$

Next, we write out the relevant reactions needed to determine the dependence of defect concentration on sulfur partial pressure.

1. Intrinsic defect is the Schottky defect (vacancy pair formation)

$$null = \mathrm{V}_{\mathrm{S}}^{\bullet\bullet} + \mathrm{V}_{\mathrm{Sn}}'' \tag{3.6}$$

$$K_{\mathrm{Schottky}} = \exp\left(\frac{-\Delta h_{\mathrm{Schottky}}}{2k_{\mathrm{B}}T}\right) = [\mathrm{V}_{\mathrm{S}}^{\bullet\bullet}]\,[\mathrm{V}_{\mathrm{Sn}}''] \tag{3.7}$$

2. Intrinsic electronic defect (electron-hole pair formation)

$$null = \mathrm{e}' + \mathrm{h}^{\bullet} \tag{3.8}$$

$$K_{\mathrm{intrinsic}} = N_{\mathrm{C}}N_{\mathrm{V}} \exp\left(\frac{-E_{\mathrm{g}}}{k_{\mathrm{B}}T}\right) = np \tag{3.9}$$

3. Sulfurization reaction

$$\frac{1}{2}\mathrm{S}_2(\mathrm{g}) + \mathrm{V}_{\mathrm{S}}^{\bullet\bullet} = \mathrm{S}_{\mathrm{S}}^{\times} + 2\mathrm{h}^{\bullet} \tag{3.10}$$

$$K_{\text{Sulfurization}} = \exp\left(\frac{-\Delta h_{\text{Sulfurization}}}{2k_{\text{B}}T}\right) = \frac{p^2}{(P_{\text{S}_2})^{\frac{1}{2}}\,[\text{V}_{\text{S}}^{\bullet\bullet}]} \tag{3.11}$$

4. Electroneutrality Condition

$$2[\text{V}''_{\text{Sn}}] + n = 2[\text{V}_{\text{S}}^{\bullet\bullet}] + p \tag{3.12}$$

For item 4 (the electroneutrality condition) there are four *possible* Brouwer approximations that one can make, to determine the dominant charge carrier for various regimes. Note that not each of these approximations will be physically meaningful for SnS.

Brouwer Approximations:

A. p-type behavior caused by tin vacancies

$$2[\text{V}''_{\text{Sn}}] = p \tag{3.13}$$

B. Intrinsic ionic defect balance

$$[\text{V}''_{\text{Sn}}] = [\text{V}_{\text{S}}^{\bullet\bullet}] \tag{3.14}$$

C. Intrinsic electronic balance

$$n = p \tag{3.15}$$

D. n-type behavior caused by sulfur vacancies

$$n = 2[\text{V}_{\text{S}}^{\bullet\bullet}] \tag{3.16}$$

We will focus only on approximation A, which is generally accepted in literature and is assumed by Rau *et al.* SnS films and crystals are nearly always reported as p-type [71]. There are only a few scattered reports of n-type SnS [30, 80], both of which likely contain a dopant material (Sb or Cl). Highly resistive, Sb-doped SnS has been reported by Sinsermsuksakul *et al.* [85]. This film showed increased resistivity

with Sb-doping, which is believed to be an n-type dopant. Although n-type behavior was not observed, it is suspected that Sb was able to compensate V''_{Sn} and create a low-doped p-type material or possibly intrinsic material.

Using Brouwer approximation A, we can determine the relationship between $[V''_{Sn}]$ (or $[p]$) and P_{S_2}. Rearranging Equations 3.7, 3.11, 3.13, we find:

$$[V''_{Sn}] = (0.25)^{\frac{1}{3}} K^{\frac{1}{3}}_{\text{Sulfurization}} K^{\frac{1}{3}}_{\text{Schottky}} P^{\frac{1}{6}}_{S_2} \tag{3.17}$$

This equation is very similar to Equation 5, given in Rau *et al.* [71]:

$$[V''_{Sn}] = (4)^{-\frac{1}{3}} K^{\frac{1}{3}}_{2} \exp\left(\frac{-E_2}{3k_B T}\right) P^{\frac{1}{6}}_{S_2} \tag{3.18}$$

Comparing Equations 3.17 and 3.18, it can be seen that:

$$K^{\frac{1}{3}}_{\text{Sulfurization}} K^{\frac{1}{3}}_{\text{Schottky}} = K^{\frac{1}{3}}_{2} \exp\left(\frac{-E_2}{3k_B T}\right) = A \tag{3.19}$$

where A is a constant for each temperature T.

A has been determined by Rau *et al.* for temperatures 560 °C through 796 °C. From these equations, we also expect a plot of $\log([V''_{Sn}])$ vs. $\log(P_{S_2})$ to have a slope of 1/6 and a y-intercept of $\log(0.25^{1/3}A)$. This is seen in Figure 4 of his paper (Figure 1-12, this manuscript).

Rau *et al.* also addresses the ionization state of tin vacancies (zero, single, or double). He states that the first ionization energy is very low and can be generally ignored, while reaching the 2nd ionization state requires a finite amount of energy. His data supports the theory that most tin vacancies are in the nd ionization state.

After the Rau *et al.* paper in 1966, very little was published on defects in SnS until researchers had new tools with which to investigate.

3.4.2 DFT (density functional theory) calculations

Several groups have published DFT calculations on SnS. The system is considered somewhat challenging due to its layered crystal structure. The bonding between layer

planes of the material are van der Waals type and can be difficult to model correctly. However, the spacing between these layer planes and the bonding character can have important consequences for the SnS band structure.

In the early 1990s, several papers were published with electronic structure calculations for SnS [84, 59, 28, 24]. Ettema *et al.* calculated Sn-S interatomic distances and strengths for both α and β-SnS. They also used XPS (X-ray photoelectron spectroscopy) and angle-resolved ultraviolet photoelectron spectroscopy (ARUPS) to corroborate their electronic structure calculations.

The past 5 years have seen a resurgence of DFT calculations on SnS [44, 101, 46, 99]. Makinistian *et al.* lists the contributing atomic orbitals for various density of states (DOS) peaks. The valence band maximum (VBM) is primarily composed of sulfur p-orbitals with some tin s-orbital character. The conduction band minimum (CBM) is primarily composed of tin p-orbitals [44].

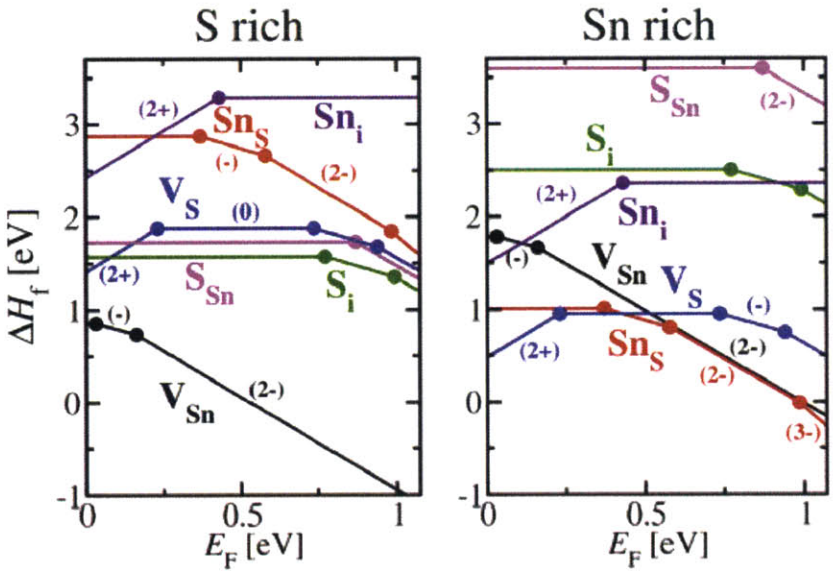

FIG. 3. (Color online) Calculated defect formation enthalpies for intrinsic defects in S-rich (left panel) and Sn-rich (right panel) limits in SnS.

Figure 3-8: Calculated defect formation energies for SnS intrinsic defects in the S-rich and Sn-rich limits. Image from [101].

Additional focus has been placed on using DFT to calculate defect formation

energies and their levels within the band gap. Vidal *et al.* provides the first calculation of various intrinsic defects in SnS, seen in Figure 3-8. Although published after the completion of this thesis, Malone *et al.* provides updated calculations on intrinsic defects and also calculates formation energies for many extrinsic defects suspected to be relevant to the SnS system [45].

Figure 3-8 plots defect formation energies (ΔH_f) on the y-axis vs. E_Fermi (which can also be read as position in the band gap, where $E_\mathrm{VBM} = 0\,\mathrm{eV}$). The dots indicate a transition in ionization or charge state, while a constant slope indicates a constant charge state. On this type of plot, defects of the same charge will always have the same slope. This diagram can give insight into some of the fundamental behaviors of SnS.

First, in the S-rich regime we notice that as the Fermi level position moves up through the band gap (a.k.a as the film be comes less p-type and more n-type), the $\mathrm{V}_\mathrm{Sn}^{(2-)}$ line continues downward, such that the formation enthalpy $\Delta H_\mathrm{f} < 0$. This suggests that even as one pushes an SnS film more n-type, tin vacancies may spontaneously form to compensate any charge donors. This might make n-type SnS difficult to form.

Second, note that the first ionization transition of the tin vacancy, from $\mathrm{V}_\mathrm{Sn}^{(0)}$ to $\mathrm{V}_\mathrm{Sn}^{(1-)}$ is very shallow and also that the second transition from $\mathrm{V}_\mathrm{Sn}^{(1-)}$ to $\mathrm{V}_\mathrm{Sn}^{(2-)}$ has a lower formation energy. Temperature-dependent Hall data from Sun *et al.* and femtosecond laser pump/probe ultraviolet photoelectron spectroscopy (fs-UPS) data also show that the activation energy for the dopant defect is 0.25 eV, while the Fermi level lies at 0.28 eV [94]. Vidal *et al.* predicts the activation of the $\mathrm{V}_\mathrm{Sn}^{(2-)}$ transition at approximately 0.2 eV [101]. These data suggest p-type doping predominantly comes from the doubly-charged tin vacancy, $\mathrm{V}_\mathrm{Sn}^{(2-)}$.

Third, the transition level of $\mathrm{V}_\mathrm{S}^{(2+)}$ to $\mathrm{V}_\mathrm{S}^{(0)}$ is lies approximately mid-gap (0.25 eV), but notably only somewhat above the $\mathrm{V}_\mathrm{Sn}^{(2-)}$ defect level. This has important consequences for the possibility of compensation of the $\mathrm{V}_\mathrm{Sn}^{(2-)}$ defect. The ionized $\mathrm{V}_\mathrm{S}^{(2+)}$ vacancy creates 2 electrons which could compensate acceptors generated by the $\mathrm{V}_\mathrm{Sn}^{(2-)}$ defect. However, this requires the full ionization of sulfur vacancies, which would

more easily occur if the $V_S^{(2+)}$ to $V_S^{(0)}$ transition level lay higher in the band gap, away from the Fermi level in the lower half of the band gap. Interestingly, in Malone *et al.*, the $V_S^{(2+)}$ to $V_S^{(0)}$ transition is found higher in the gap, suggesting compensation by $V_S^{(2+)}$ is very possible [45]. The position of the transition levels within the band gap do not change between the S-rich or Sn-rich regime. However, their formation energies (position along the y-axis) do change greatly.

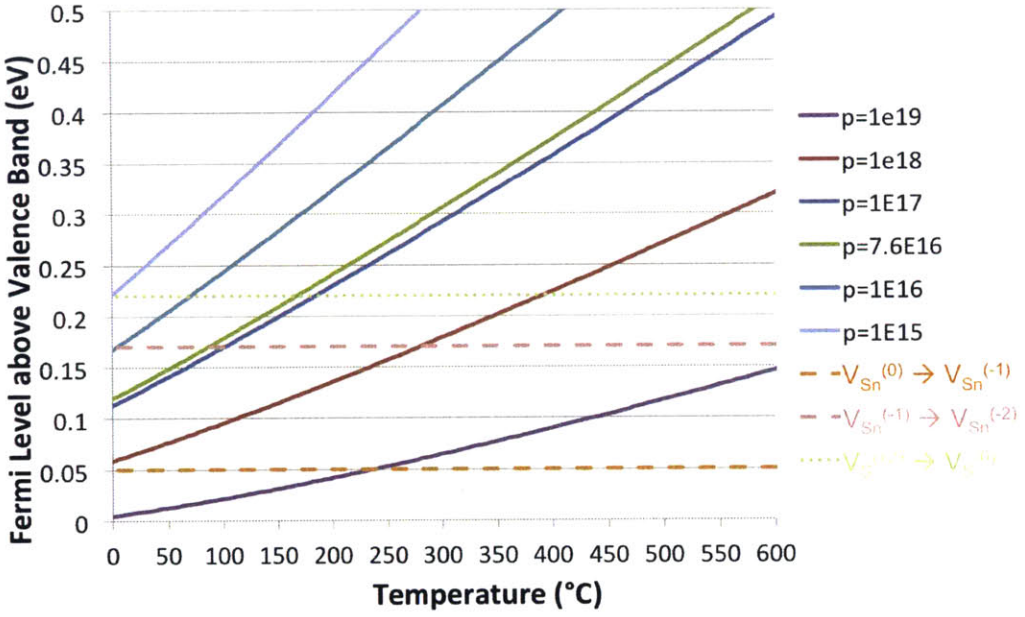

Figure 3-9: SnS Fermi level position calculated for different doping densities, using Equations 3.20 and 3.21. Defect level positions for $V_{Sn}^{(1-)}$ (orange), $V_{Sn}^{(2-)}$ (pink), and $V_S^{(2+)}$ (light green) are plotted from Vidal *et al.*

The position of these three transition levels are pictured in Figure 3-9 and plotted with the calculated Fermi level for various p-type carrier concentrations. The Fermi level is calculated from Equation 3.20:

$$E_f = E_v - k_B T \ln\left(\frac{p}{N_v}\right) \tag{3.20}$$

E_v (valence band position) is set to zero, while N_v = effective density of states at

the valence band edge is calculated from the approximation:

$$N_v = 2\left(\frac{2\pi m_h^* k_B T}{h^2}\right)^{3/2} \tag{3.21}$$

m_h^* is calculated as an average of the hole effective masses in the a, b and c directions (from Vidal *et al.*). Because of the mostly random grain orientation in the SnS films on molybdenum, a particular direction for effective mass was not chosen, instead an average of the 3 principal directions is used. Errors in the value chosen for hole effective mass (used for the density of states calculation) will cause greater error in the Fermi level position as $[p]$ increases or as T decreases. This plot offers a visualization of how Fermi level changes based on doping density in SnS and how it is changing relative to the defect levels of primary importance ($V_{Sn}^{(+1)}$, $V_{Sn}^{(+2)}$, and $V_S^{(+2)}$). When carrier concentrations in SnS thin films are measured by Hall effect, this plot can be useful to visualize where the Fermi level may reside.

The fourth interesting feature of Figure 3-8 are the formation energies of $V_S^{(2+)}$ and $V_{Sn}^{(2-)}$ defects. To calculate defect concentrations, we assume the film is in thermodynamic equilibrium and use the ΔH_f, read from Figure 3-8 for each defect in both regimes. In the S-rich regime (red in Figure 3-8), $\Delta H_{f,V_{Sn}^{(2-)}} = 0.75$ eV and $\Delta H_{f,V_S^{(2+)}} = 1.90$ eV. In the Sn-rich regime (blue in Figure 3-8), $\Delta H_{f,V_{Sn}^{(2-)}} = 1.70$ eV and $\Delta H_{f,V_S^{(2+)}} = 0.95$ eV. We use an Arrhenius equation for defect concentrations in equilibrium:

$$c = N_{sites} N_{config} \exp\left(\frac{-\Delta H_f}{k_B T}\right) \tag{3.22}$$

where c = concentration of defect per unit volume (typically cm^{-3}), N_{sites} = number of sites in the lattice (per volume) available for the defect ($1.04 \times 10^{22}\ cm^{-3}$ for either vacancy in SnS), N_{config} = number of equivalent configurations in which the defect can be incorporated. Here, assumed to be 1 because we are dealing with vacancy defects. [100]

Examining Figure 3-10, we see that in the S-rich regime (red lines), the $V_S^{(2+)}$ concentration is many orders of magnitude below the $V_{Sn}^{(2-)}$ concentration. However, as the material transitions to the Sn-rich regime (blue lines), the $V_S^{(2+)}$ defect dominates

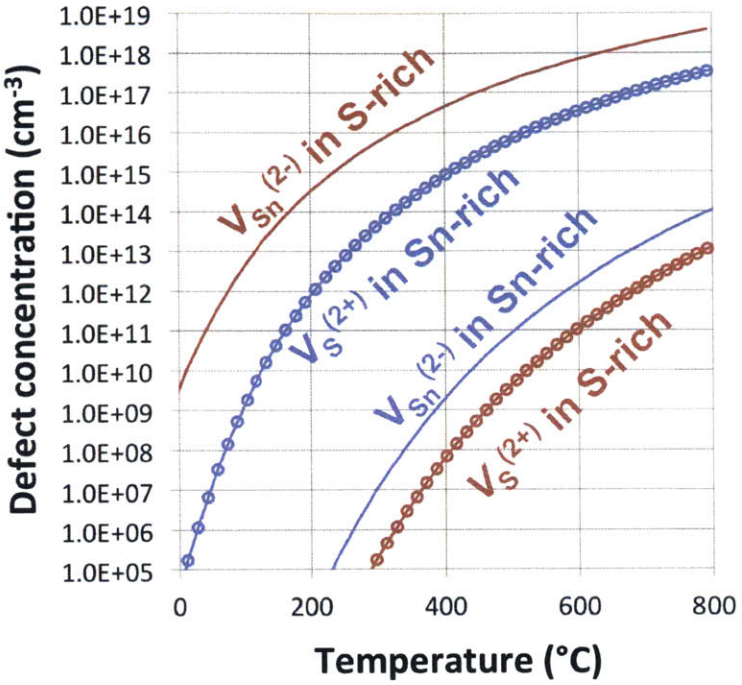

Figure 3-10: Defect concentrations calculated from the formation enthalpy of the indicated defects (ΔH_f calculated by Vidal *et al.*). The data shows that in S-rich films, the $V_{Sn}^{(2-)}$ defect dominates, creating *p*-type SnS. In Sn-rich films, the $V_S^{(2+)}$ defect should dominate, but *n*-type behavior is not typically observed.

by many orders of magnitude. Again, because of the position of the $2+ \rightarrow 0$ transition, not all V_S defects may be ionized. It does suggest though, that a compensation regime may exist somewhere between these two extremes of S-rich and Sn-rich SnS. The possibility of this regime depends on the exact position of the Fermi level relative to the positions of each defect. Furthermore, the formation energies used here are only from one source and could benefit from other supporting calculations.

Mid-gap defect states

The Vidal *et al.* paper also discusses the possibility of the $V_S^{\bullet\bullet}$ defect as a recombination center or trap state. This behavior is common of many mid-gap defects because the localized defect level enhances the probability of electrons and holes recombining from the conduction and valence bands (Shockley-Read-Hall recombination). As the

SnS film is pushed to a more S-rich state, the ΔH_f of $V_S^{(2+)}$ becomes larger and its equilibrium concentration is reduced. Recombination centers are known to reduce minority carrier lifetime, thus a reduction in the concentration of $V_S^{\bullet\bullet}$ is suspected to improve minority carrier lifetime and diffusion length.

To picture the levels of sulfur vacancies we might find in SnS, we can use Equation 3.7. Re-arranged, it can describe the concentration of $V_S^{\bullet\bullet}$ for a given temperature and measured $[V''_{Sn}]$ (assuming $[p] = 2[V''_{Sn}]$ and a material in equilibrium):

$$[V_S^{\bullet\bullet}] = \frac{A^2 \exp\left(\frac{-\Delta h_{Schottky}}{k_B T}\right)}{[V''_{Sn}]} \tag{3.23}$$

where A = number of sites for a sulfur or tin vacancy (a.k.a. $[S_S^{\times}]$ or $[Sn_{Sn}^{\times}]$ = $1.04 \times 10^{22}\,cm^{-3}$) and assuming $\Delta h_{Schottky} = \Delta h_{V''_{Sn}} + \Delta h_{V_S^{\bullet\bullet}} = 0.75\,eV + 1.9\,eV = 2.65\,eV$, from Vidal *et al.* DFT calculations.

From Figure 3-11, we observe that only at higher temperatures (+400 °C) does the $[V_S^{\bullet\bullet}]$ begin to approach levels where it might impact minority carriers. However, because the processing temperatures applied are 400 °C or higher, we cannot rule out the possibility that sulfur vacancies could impact minority carrier lifetime, even for a film at room temperature. The film could be metastable, or "trapped" in a higher-temperature equilibrium state (due to slow kinetics at lower temperatures). These calculations, as stated above, assume equilibrium. This will be addressed later in Chapter 5.2.3.

Drawing from experience in minority carrier lifetime in silicon, $10^{11}\,cm^{-3}$ is a rough cut-off value for which sulfur vacancy concentrations below this value would likely not affect minority carrier lifetime (this ignores the impact of capture cross-section of the defect). Making another rough assumption of $p \sim [V''_{Sn}]$, we examine the x-axis in the region of $10^{15}\,cm^{-3}$ to $10^{18}\,cm^{-3}$ (marked with grey dashed lines), which is common for SnS solar cells. In this region, up to temperatures of 450 °C, the equilibrium $[V_S^{\bullet\bullet}]$ as calculated from the Schottky formation energy is always below $10^{11}\,cm^{-3}$. While this does not prove that the concentration of $V_S^{\bullet\bullet}$ is low enough to not affect minority carrier lifetime, it raises the possibility that sulfur vacancies might not affect minority

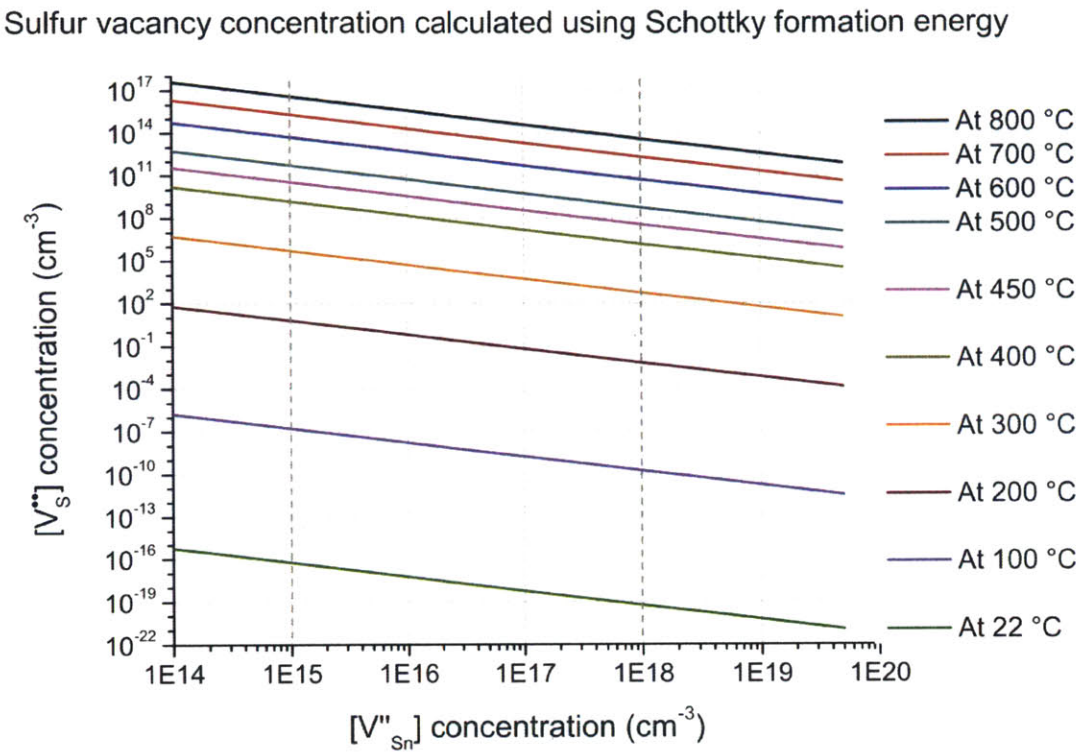

Figure 3-11: Calculated $[V_S^{\bullet\bullet}]$ concentration for a given $[V''_{Sn}]$ (x-axis) and temperature, using an estimated Schottky defect formation energy from DFT calculations, where $\Delta h_{\text{Schottky}} = 2.65\,\text{eV}$. Using these estimated values, the concentration of sulfur vacancies may only becomes detrimental to minority carrier lifetime at temperatures above 400 °C. However, this assumes film equilibrium, which is not likely. Grey dashed lines mark the majority carrier concentration regime common for SnS solar cells.

carrier lifetime.

At the start of this thesis and also at its completion, there is no known way to measure minority carrier lifetime. Photoluminescence proved difficult due to the indirect band gap and highly defective nature of as-deposited SnS. Exploration into a pump-probe THz spectroscopy method is currently underway. Regardless of the difficulties in directly measuring minority carrier lifetime, any reduction in Shockley-Read-Hall recombination centers should also cause an increase in minority carrier diffusion length ($L = \sqrt{D\tau}$). This should be observable as an increase in efficiency and in minority carrier collection in an SnS device (a.k.a. J_{SC}), all other things being equal.

3.4.3 Discussion of Kröger-Vink theory and modern DFT defect calculations

When these two methods of calculating defect concentrations are compared, they show some clear differences. The Kröger-Vink method requires several assumptions upfront, while DFT defect level calculations are from first-principles. A brief discussion of the merits of each method is discussed in Van de Walle *et al.* [100], although there is a clear preference for the modern methods of DFT calculation. For well-studied systems the Kröger-Vink model can predict behavior well. However, for new or less studied materials, many assumptions must be made to derive defect concentrations by the Kröger-Vink method. In these cases, perhaps DFT methods should be preferred.

Figure 3-12 is a comparison of Rau's data derived from the Kröger-Vink model [71] and Vidal *et al.* calculations by DFT [101]. Phase is also considered by using data from Piacente *et al.* [65].

The 8 solid parallel lines are derived from Rau, specifically using Equation 3.18. This equation has been used with a range of P_{S_2} values from 1×10^{-8} torr to 1×10^{-1} torr, and a range of temperatures that extend beyond his data set. These 8 lines represent the $[V''_{Sn}]$ calculated from Kröger-Vink theory. The $[V''_{Sn}]$ concentration plotted for different sulfur partial pressures (P_{S_2}) are connected by the dark green $\times$'s, which represent a "phase boundary" between SnS and Sn_2S_3. This "phase boundary" is also calculated using using Equation 3.18. The (T, P_{S_2}) coordinates used in Equation 3.18 belong to the SnS/Sn_2S_3 phase boundary derived from Piacente *et al.* and Equation 3.3. This line represents the highest $[V''_{Sn}]$ concentration thermodynamically possible for that temperature and pressure combination, while still maintaining SnS phase. To the left of the green-$\times$ line is SnS phase and to the right are (T, P_{S_2}) combinations where Sn_2S_3 is thermodynamically favored.

The blue line with diamonds is quenched single crystal data from Albers *et al.* 1961 (Figure 7), assuming $[p] = 2[V''_{Sn}]$ [5]. The experimental details are unclear, but suggest they were annealed at a temperature and P_{S_2} very close to the SnS/Sn_2S_3

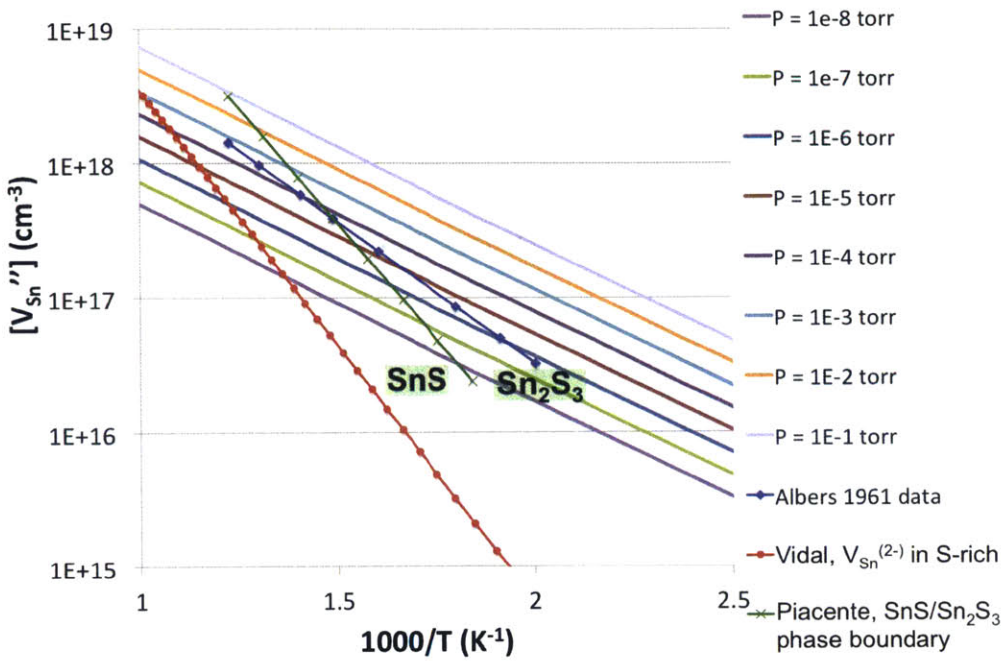

Figure 3-12: Comparision of $[V''_{Sn}]$ derived and measured by Rau (8 parallel solid lines) vs. defect concentrations calculated by Vidal (red with circles). Pressure (P) refers to sulfur partial pressure (P_{S_2}) as it is used in Kröger-Vink calculations. The blue diamond line represents a single-crystal quenching experiment performed by Albers *et al.* 1961. The green ×'s represent a "phase boundary" between SnS and Sn_2S_3, derived from Piacente *et al.* data and $[V''_{Sn}]$ equations from Rau. It represents the maximum possible $[V''_{Sn}]$ concentration in SnS, before Sn_2S_3 starts forming, as calculated from Rau's application of Kröger-Vink theory.

phase boundary. While the data do overlap, the slopes are not the same. This could point to experimental problems, such as slow quench rate, or a difference in mechanism of V''_{Sn} generation, discussed previously in Chapter 1.4.2 (dissociation and ionization vs. Schottky defect generation).

The red line with dots represent the $[V^{(2-)}_{Sn}]$ concentration calculated using the formation energy ($\Delta h_{V^{(2-)}_{Sn}}$) from Vidal *et al.* 2012. This formation energy was taken from the S-rich regime DFT calculation (Figure 3-8). This S-rich regime is at or near the SnS/Sn_2S_3 phase boundary. For any given temperature, Vidal's calculations are approximately an order of magnitude lower than that of the Piacente/Rau data combination (green ×'s). The reason for this is yet unclear, but merits further investigation. However, these two data sets (green ×'s and red dots) have approximately

the same slope.

3.5 Desired range of conditions for H_2S annealing

3.5.1 Temperature range for phase control

We refer back to Figure 3-6 and use this diagram to draw limits on temperatures needed for the furnace. For example it will not need to go above 602 °C, since there is a phase transition to β-SnS at 602 °C. The P_{S_2} should never need to go above $\log_{10}(P_{S_2})$ = -2.87 = 1.03 torr. Any P_{S_2} higher than 1.03 torr at 602 °C would create sulfur-rich phases (primarily Sn_2S_3). Ideally, the blue line in Figure 3-5 should be the same line on Figure 3-6, which is the phase boundary line between SnS and Sn_2S_3. However, examining the data at 602 °C, a slight difference of P_{S_2} = 0.77 torr is observed. This suggests there is both experimental and theoretical uncertainty in the exact position of this phase boundary. However, the two data sets are close enough to give a target range.

The upper limit on temperature is 602 °C, while the lower limit is less well-defined. Based on melting temperature alone, SnS will tend to have lower processing temperatures than CIGS, CZTS, CdTe or Si. In general, investigations of disorder can happen in a lower temperature range between 100–200 °C, with the order-disorder transition in CZTSe found to be 200 °C [73]. Also, because the operating temperatures of solar cells can reach 30–60 °C, it is desirable to have the cell material stable at these temperatures. Thus, one could roughly draw a lower limit at 200 °C.

3.5.2 P_{S_2} range for p-type carrier concentration control

As stated in the previous section, using Figure 3-6 we can see that the maximum P_{S_2} that should be needed is 1.03 torr, if we assume equilibrium conditions.

To determine the lower limit of requirements for P_{S_2} we first assume that the highest quality films of SnS will be made at a condition near the SnS/Sn_2S_3 phase boundary. This is the region where there should be fewest $V_S^{\bullet\bullet}$ that may cause re-

combination. Looking at the low temperature region on Figure 3-6 (near 200 °C), we see that the necessary P_{S_2} is $\log_{10}(P_{S_2})$ = -14 = 7.6×10^{-12} torr. The utility of annealing at such low temperatures such as 200 °C is probably low, since very little grain growth or diffusion is likely to occur. However, it would be best to attempt to design the furnace to reach as a low a P_{S_2} as possible.

A suggested method of controlling P_{S_2} is briefly described in the single-crystal studies from the 1960s [71]. This method involves mixing H_2S and H_2 gas. It relies upon an interaction between H_2S and H_2 and S_2 molecules. This reaction is the decomposition of H_2S:

$$2H_2S(g) \rightarrow 2H_2(g) + S_2(g) \tag{3.24}$$

Relating this reaction using the equilibrium reaction constant:

$$K_{eq,P} = \left(\frac{P_{H_2}}{P_{H_2S}}\right)^2 P_{S_2} \tag{3.25}$$

where P_{H_2}= partial pressure of H_2 gas and P_{H_2S}= partial pressure of H_2S gas. The equilibrium constant is fixed for each temperature, thus as the ratio between P_{H_2} and P_{H_2S} changes, the P_{S_2} will also change. This equation also shows that even if the total pressure of the gases changes, when the ratio P_{H_2}/P_{H_2S} is constant, the P_{S_2} remains fixed. When the ratio P_{H_2}/P_{H_2S} increases, the P_{S_2} must decrease, because $K_{eq,P}$ is fixed (assuming constant temperature). Similarly, as P_{H_2}/P_{H_2S} decreases, the P_{S_2} must increase. Rearranging Equation 3.25:

$$P_{S_2} = K_{eq,P}\left(\frac{P_{H_2S}}{P_{H_2}}\right)^2 \tag{3.26}$$

At the temperatures currently considered for SnS annealing experiments (200–600 °C), the kinetics of the decomposition reaction (Equation 3.24) become a concern [34, 36]. The forward rate reaction of H_2S decomposition becomes slow at temperatures below 700 °C. Because the samples will never experience 700 °C, this may effectively limit the range of P_{S_2} achievable without the intervention of a catalyst.

Other methods of introducing a P_{S_2} include evaporating sulfur powder or a com-

pound such as CS_2. However, both of these materials have a high P_{S_2} at comparatively low temperatures (<100 °C). Controlling the P_{S_2} at extremely low levels will be difficult using this evaporation method. In particular, evaporating sulfur powder creates a zoo of sulfur molecules S_x where $x = 1$–8. It is unclear what the effect of additional sulfur molecules would have on SnS.

Additionally, preliminary results have shown that H_2S itself may have a unique effect on SnS grain growth, rather than exposure to S_x vapor. This further supports the decision to use an H_2S/H_2 gas mixture as the source of sulfur in SnS annealing experiments.

3.5.3 Total pressure requirements

The lower pressure range of the furnace is simply decided by the base pressure of the pump and system. The upper range was decided based on the results of Chapter 3.1.3. This was a successful anneal that showed grain growth and stoichiometry adjustment. The parameters of this anneal were adjusted for the design criteria of the new furnace. The preliminary anneal used 100 % H_2S gas at 1 torr pressure. The same H_2S partial pressure can be obtained by using 4 % H_2S gas and multiplying the pressure by 25 to get 25 torr ($P_A = X_A P_{total}$, where X_A is the concentration of the gas species A).

SnS sublimation could be an issue at higher temperatures, causing loss of material. For this reason, higher total pressures are thought to be useful for preventing material evaporation. A practical upper limit is set at 1 atmosphere = 760 torr, primarily for safety reasons.

3.6 Summary of annealing motivations

Initial annealing experiments on RF sputtered SnS films showed the promise of annealing in H_2S. We have reviewed the goals for film changes and improvements that annealing can induce, such as reduced grain boundary density, phase control, carrier concentration control, and reduction of mid-gap defect states. Based on the models of Kröger–Vink/Rau and DFT calculations, these are achievable goals. P_{S_2} will be

controlled by a H_2S/H_2 gas flow ratio, and deviation thermodynamic behavior can be captured by an RGA (residual gas analyzer).

Chapter 4

Design and building of the H_2S furnace

In order to pursue the annealing of SnS in H_2S gas, I built a dedicated tool for these experiments. It was designed with maximal flexibility for design of experiments and as well for safety. The toxicity and corrosiveness of H_2S gas proved to be a large but surmountable challenge.

H_2S gas is flammable above 4 % concentration. For this reason it was decided that all experiments would use 4 % H_2S concentration or lower. However, the furnace was also designed for use with 100 % H_2S gas, if needed.

4.1 Materials and performance requirements

As outlined in the previous Chapter 3.5, the maximum temperature in the furnace will be 600 °C, the P_{S_2} gas range should ideally be 7.6×10^{-12} – 1 torr (as determined by the P_{H_2}/P_{H_2S} ratio and $K_{eq,P}$), and the maximum total pressure should be 760 torr. Temperature, sulfur partial pressure and total pressure are 3 necessary parameters for the adjustment of SnS thin film properties during annealing, but there are also other considerations:

1. **Purity** To minimize the introduction of impurities during annealing, materials (particularly in the hot zone) should be selected for their inertness at high

temperature. Purity is also why experiments occur in a vacuum chamber that has been purged of residual oxygen and water vapor.

2. **Size of samples** The current maximum sample size in the thermal evaporator is 1" by 1" (25 mm by 25 mm). The furnace tube was selected to be 50 mm OD (outer diameter) and 47 mm ID (inner diameter) so that it can accommodate several samples of various sizes.

3. **Temperature ramp/cool rates** In particular, the rate of cooling is known to be particularly important for control of defects. A fast cool (or quench) can lock-in defects at high temperatures, whereas a slow controlled linear cool can allow relaxation of a material [32]. Ramp rates should be fast, so that the ramp time does not contribute significantly to the overall annealing time.

4. **Flexibility** In the context of a new experimental tool, flexibility offers the opportunity to run many various types of experiments with different gas conditions, different materials, different cooling mechanisms, measuring electrical signals from the film *in-situ*, etc. The user should be able to modify the furnace safely while performing the desired new experiment.

5. **Safety** The furnace must pass a safety certification by EHS, but more importantly, should be safe for the operator and everyone in the lab. The system should include backups and failsafes, in case the main line of defense (air exhaust) is disabled. It should also have an easy way for every sub-system to be shut down, in case of emergency.

4.2 Discussion of materials selection

The materials usage options can broadly be drawn into three categories depending on the temperature of the application and certain functional requirements. A paper by Dasgupta *et al.* proved incredibly useful during the design stage [20].

1. **Inert at high temperatures** The requirement that a material withstand H_2S corrosion at temperatures of 600 °C is primarily driven by the hot zone. Corrosion by H_2S at high temperatures is rapidly accelerated, whereas corrosion at room temperature is very slow. The materials in the hot zone should also be of high purity, because they come in direct contact with the sample. Options include: *clear fused quartz, alumina, graphite.* Quartz was selected for the furnace tube material because of ease of cleaning/etching and ease of visibility into the hot zone. Quartz also easily maintains vacuum, while graphite must be specially treated to reduce porosity.

2. **Corrosion resistant but ductile** This requirement is primarily driven by the need for pipes to transport H_2S gas safely. According to Dasgupta *et al.* and many in the oil drilling industry, 300-series stainless steel (SS) is resistant to H_2S corrosion at room temperature. At elevated temperatures above 400 °C, corrosion does occur at a known rate. Generally, alloys with a high chromium content and little to no nickel content are preferred. Leffler records a corrosion rate of 1.5 mm/year for corrosion of 316 SS at 500 °C, during continuous exposure to 50 % H_2S/50 % H_2 at atmospheric pressure [42, 63]. This corrosion rate means that stainless steels should not be exposed to H_2S at elevated temperatures above 400 °C. Below 400 °C, there is little corrosion. With purity also in mind, several alloys are preferred: *316L, 316, and 304.* For cost reasons, 316 SS (instead of 316L) is primarily used, while 304 SS is occasionally used.

3. **Corrosion resistant sealants** This requirement is driven by the necessity for a vacuum seal. Not only should the furnace be cleared of air (oxygen, CO_2, water, argon), but H_2S cannot leak out. For cost reasons, an oil pump is being used. Oil pumps can be configured with low chemical reactivity oil, such as *Krytox*, a PFPE (perfluoropolyether) based substance. Metal-to-metal seals (Swagelok and VCR connections) were used when possible, made with 316 SS. But for valves and metal-to-quartz seals, an elastomer is needed. Elastomers resistant to H_2S gas at elevated temperatures include: *Kalrez, Chemraz and*

Markez, which are all perfluoroelastomers (FFKM). Kalrez has by far the best corrosion ratings and widest temperature application range [20, 75, 62]. Despite its high cost, Kalrez compound 7075 was used in all of the high temperature and high H_2S exposure areas (such as metal-to-quartz seals), and in any valve seats that are exposed to H_2S gas. Elastomers resistant to H_2S gas at room temperature include: *Aflas, teflon, and buna-N.* Aflas and teflon seals are used in room temperature areas where the H_2S gas content should be dilute.

4.3 Construction and diagrams

4.3.1 Temperature and hot zones

The furnace is built with a 32" long 47 mm ID/50 mm OD clear fused quartz tube. This tube can be replaced and/or cleaned using dilute hydrochloric acid (HCl) and dilute hydrofluoric acid (HF), allowing different materials to be used in the furnace. It contains 3 zones, two of which have nichrome heating elements surrounding the outside. These two zones are each 6" long and are separated by 2". Both of these zones also have a thin layer of alumina insulation surrounding the nichrome elements on the outside of the tube. The nichrome elements were assembled and wired in the lab, instead of purchasing a commercially designed furnace. This allows for less insulation and faster cooling of the hot zones. Two heated zones exist for added experimental flexibility. In the 2^{nd} zone (see Figure 4-1) a powder can be heated, while a sample sits in the 1^{st} zone (Main zone) thus creating a vapor transport experiment. Each zone is controlled independently by a PID controller and current is supplied by a solid state relay. Both zones can reach 600 °C in less than 5 minutes. A slightly slower ramp rate is usually used to prevent temperature overshoot.

The third zone is a 13" length of unheated tube. This extra space allows for options such as loading or quenching mechanisms. Using a heating blanket, it can also become a low-temperature heated zone.

There is also at least 2" of space between the hot zone and a metal-to-quartz

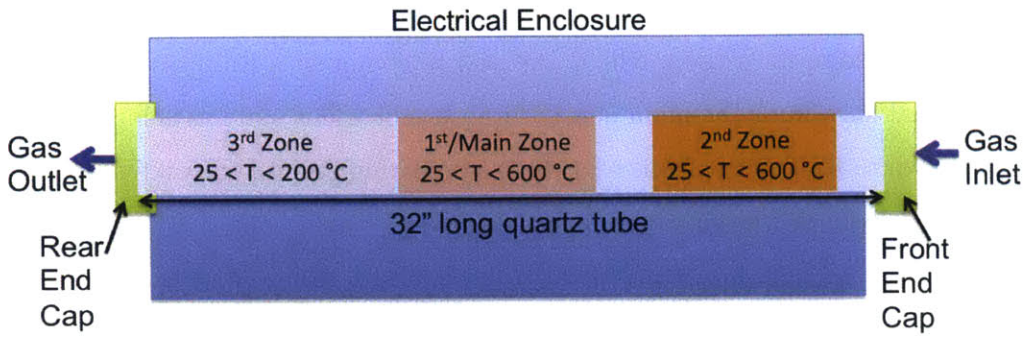

Figure 4-1: Basic view of the primary heating areas of the H_2S furnace. The 1st/Main zone is where samples are placed and the 2nd zone is for heating of powders. The 3rd zone usually is empty, but can also be used for quenching mechanisms. Direction of gas flow is from front (right) to rear (left). The quartz tube is 50 mm OD and 32" long.

Kalrez seal. This is to prevent overheating and failure of the Kalrez seal.

Measuring and recording temperature in both zones using a K-type thermocouple was a challenge due to the corrosive nature of the gas. A $\frac{1}{4}$" OD quartz tube was sealed at one end using a oxyacetylene or hydrogen torch, then attached to each end cap (one thermocouple for each hot zone). A thermocouple is then strung into the sealed $\frac{1}{4}$" quartz tube, until it reaches the center of each hot zone. In this way, the thermocouple can sit in the middle of the hot zone, but be unaffected by the gas composition. There is some thermal lag due to the quartz surrounding the thermocouple tip, but in steady-state conditions, this design yields a more accurate read of the sample temperature (as opposed to placing the thermocouple on the outside of the tube).

4.3.2 Gas flow

A vacuum-tight seal at each end of the quartz furnace tube is made with two custom-designed end caps. Commercial metal-to-quartz seals were not used due to space considerations and cost. Each end cap plate is a 316 or 304 SS plate with a $\frac{1}{4}$" OD 316 SS tube welded to it. This tube is where gas inlet/outlet connections are made using Swagelok double ferrule seals. Each end cap plate supports a $\frac{1}{4}$" diameter quartz tube for a thermocouple (one for each heated zone). The seal to this $\frac{1}{4}$" quartz tube

is made using a welded quick-disconnect joint and a small Kalrez o-ring [68]. The end cap plate has 4 holes for screws, which are used to compress a Kalrez o-ring into a metal seat that surrounds the main quartz furnace tube. This seal has achieved base pressures down to 6 mtorr, which is close to the operating limit of the oil pump. The end cap can be seen in Figure 4-2.

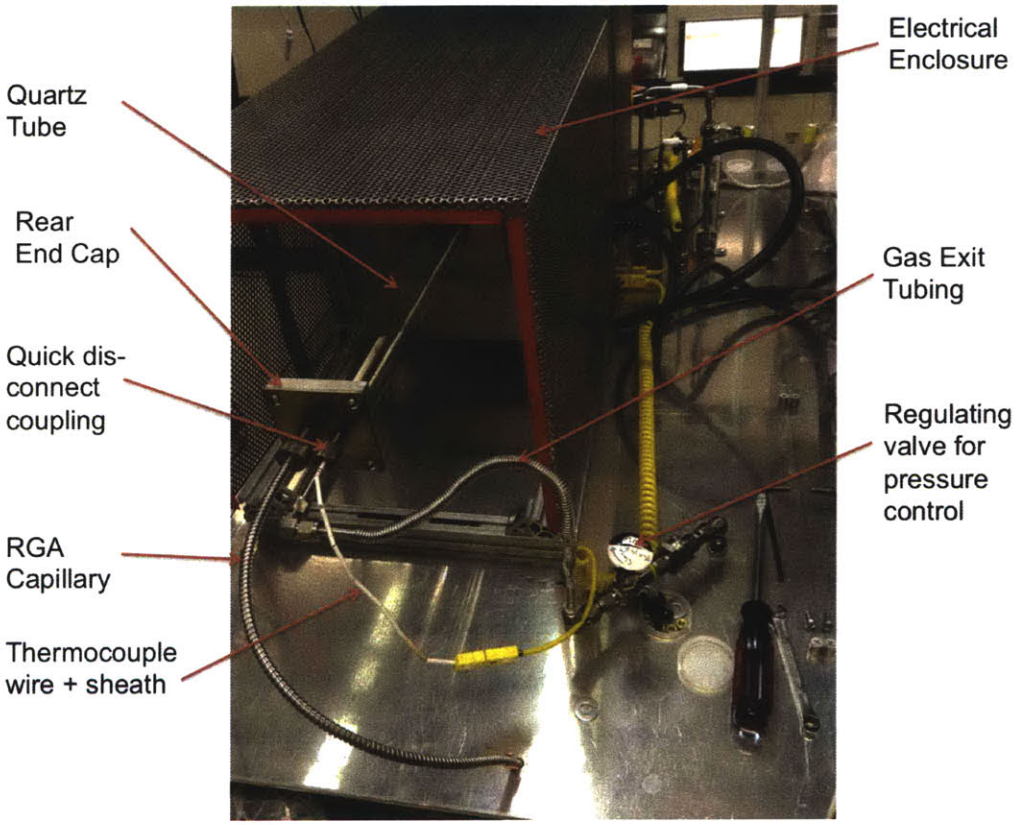

Figure 4-2: Photo shows the "exit" end of the gas furnace and 3rd zone. At "exit" end, gas leaves the quartz tube and some gas goes through the RGA capillary. The furnace end cap design and thermocouple placement is also shown.

Control of gases in the furnace is mainly achieved by mass flow controllers (MFC), valves and an oil pump. Four gas types were selected for use in the furnace: 4 % H_2S in 96 % N_2, 4 % H_2 in 96 % N_2, 99.999 % N_2, and 99.999 % Ar (all purchased from Airgas). The gases are segregated by corrosiveness. A small 4 % H_2S tank (Airgas size 33A) was purchased and mounted inside the solvents hood, to provide adequate ventilation. The other three tanks can be stored normally, inside the lab.

Two all-metal seal, multi-gas, multi-range, digital, normally-closed MFCs were purchased from MKS Instruments. These are both controlled by a Java script program on a laptop, connected by an ethernet cable. The MFC with a 1000 sccm full-scale range is used only to control H_2S gas flow. It is mounted inside the solvents hood, near the H_2S tank, so that it can act as a secondary shut-off valve during an emergency.

An MFC with a full scale range of 100 sccm is used to control the 4% H_2, N_2 and Ar. Plastic Tygon tubing ($\frac{1}{4}$" diameter) connected these three gases from their respective regulators to a gas manifold, where the gases merge pathways and enter the MFC. The plastic tubing was later replaced with $\frac{1}{8}$" diameter 316 SS tubing for improved vacuum base pressure and reduced leakage. The gas line from the H_2S tank regulator is $\frac{1}{4}$" diameter 316L SS and contains an in-line pneumatic safety valve before it reaches the MFC. Between the MFC (in the solvents hood) and the furnace, the H_2S piping must cross the room. This section of pipe is one continuous piece of tubing, which reduces the possibility of leaks at any metal-to-metal seals.

The full-scale range (1000 sccm) of the MFC which controls H_2S gas flow and the full-scale range (100 sccm) of the MFC that controls H_2 gas flow will together determine the maximum and minimum P_{H_2}/P_{H_2S} ratio that can be achieved in this furnace. Each MFC also has a low-flow limit, beyond which a stable flow cannot be maintained by the MFC. The range of practically achievable P_{H_2}/P_{H_2S} ratios is 0.09 to 10.0. When inverted, the P_{H_2S}/P_{H_2} ratio range is from 0.1 to 11.11.

Various valves (open/close and regulating) isolate specific ares of tubing and the furnace so that particular sections can be filled with gas or purged. These valves can be seen schematically in Figure 4-3 (top-view) and Figure 4-4 (front-view). They have an alpha-numeric label and are outlined in black boxes. Valves in areas that will be exposed to H_2S gas have Kalrez seals. The other valves have Viton seals, which are not corrosion resistant to H_2S. The primary method of pressure control is by adjusting a regulating valve at the gas exit of the furnace (marked in Figure 4-2 as RV17 and seen in Figure 4-2). Pressure can also be adjusted by changing the total flow into the furnace, which is determined by the MFC settings.

Gas flow proceeds from the tanks, through the MFCs, through the quartz tube,

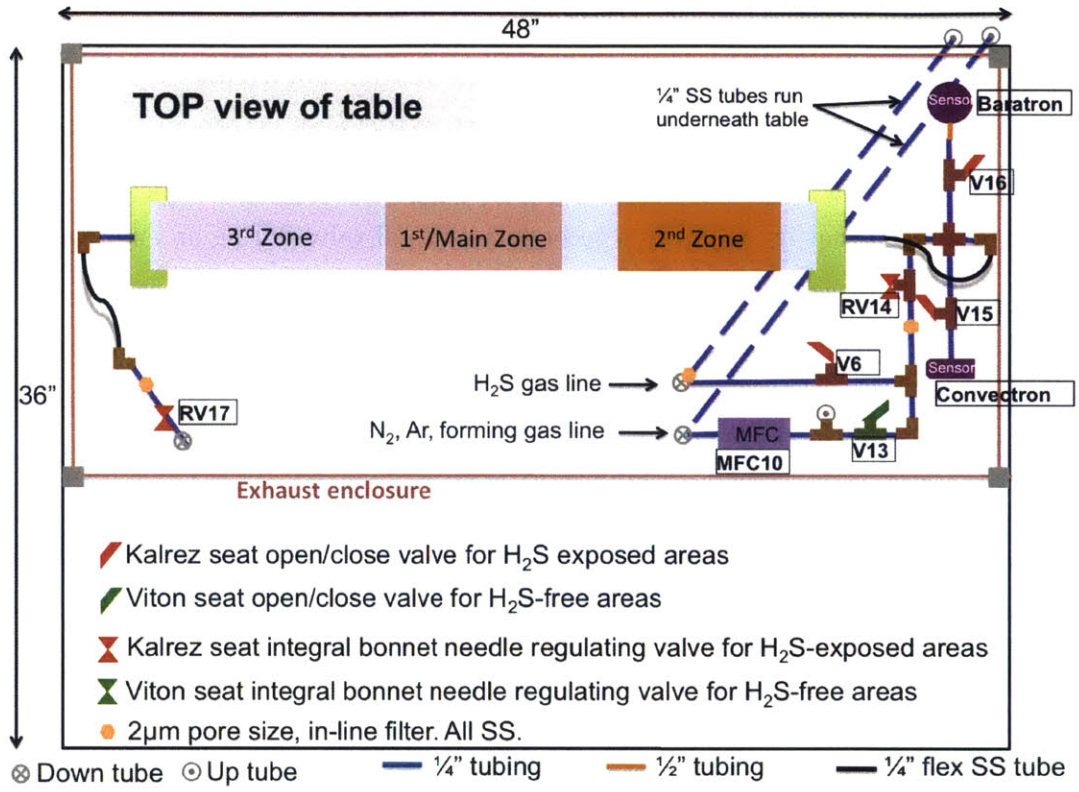

Figure 4-3: Furnace top-view diagram. Valves are labeled in black boxes. Different types of valves are also indicated by the legend. Two pressure sensors are labeled as Baratron and Convectron. Schematic is close, but not exactly to scale.

then through 2 gas traps. The first trap is an 8" diameter filter filled with a proprietary metal-oxide mixture called SulfaTreat SelectUltra. It was donated by MI Swaco, a subsidiary of Schlumberger. The material was developed to absorb H_2S gas from natural gas. It is typically sold by the palette, not the pound. This trap absorbs the majority of the H_2S that is released during an experiment. The gas then continues through a molecular sieve filter for reducing oil backstream diffusion, then through the oil pump and finally to the building exhaust system. Flexible metal tubing ($\frac{1}{4}$" and 1" diameter) and KF connections (with Kalrez or Aflas seals) are used for all sections of tubing after the quartz tube.

Total pressure is an important variable to measure during experiments. Unfortunately, measuring pressure at the hot zone is not possible due to the high temperature

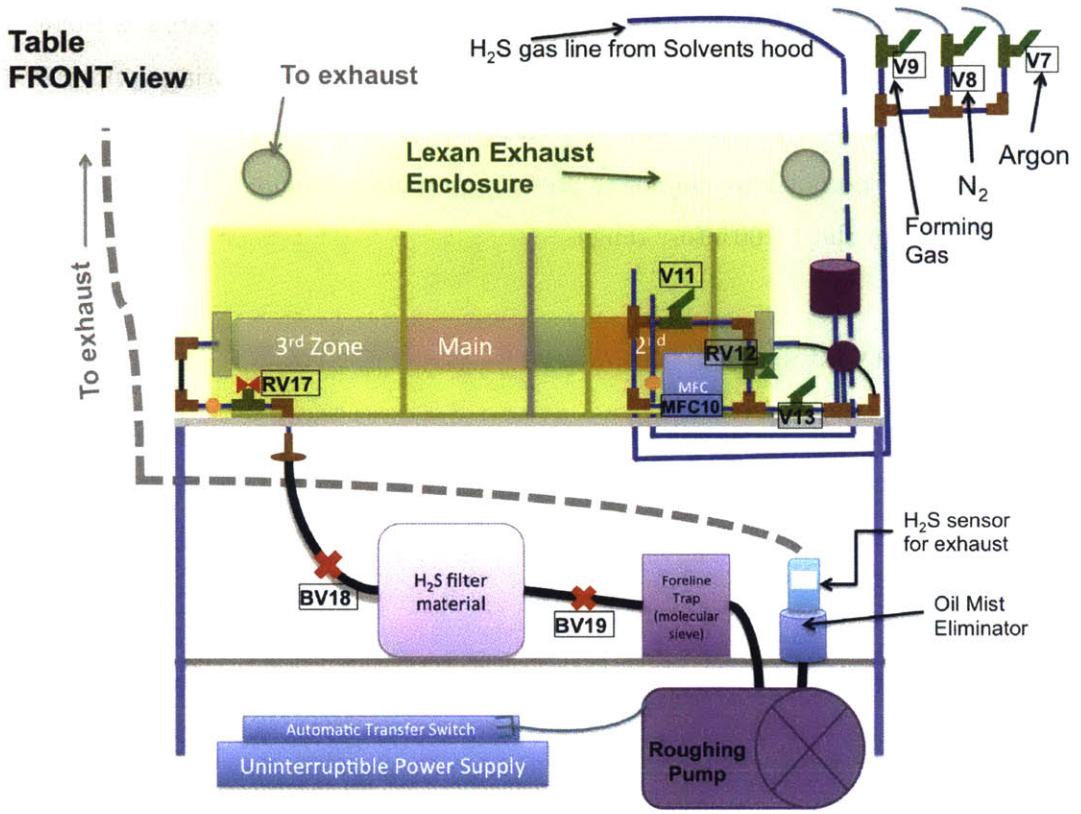

Figure 4-4: Furnace front-view diagram. Still using legend from previous figure. Yellow box around furnace is the electrical enclosure, while the green box indicates the exhaust enclosure.

and corrosive environment. The sensors are instead placed as close to the hot zone as possible. Two different sensors are used, primarily due to the corrosiveness of the H_2S gas. A capacitance manometer is one of the few gas-type independent measurement sensors available. It operates solely based on measuring the capacitance between two metal plates, one of which deflects due to changes in pressure. These sensors unfortunately have limited range and can damage easily from over-pressurization. A capacitance manometer (or Baratron, purchased from MKS Instruments) with a 100 torr range sensor is primarily used. A 1000 torr full-scale range capacitance manometer was also recently installed. To get a better idea of the furnace base pressure, a Kurt J. Lesker convectron is also installed. This pressure sensor has a range from 0.1 mtorr to 1000 torr. It cannot be used with H_2S gas because it would likely corrode the

filament inside, but N_2, Ar and H_2 are safe to measure. The convectron is isolated from H_2S gas by a valve. This pressure sensor is most useful for ensuring appropriate base pressure has been achieved and for leak testing. Capacitance manometers of the range used here do not have the lower pressure resolution required for base pressure measurements in the 1–100 mtorr range.

4.3.3 Safety systems

Here we review some of the safety systems design for this furnace. Further details of operation can be found in the tool SOP (standard operating procedure).

Enclosure

It is common practice for these types of systems to be located in a hood or other area of high exhaust flow. During a leak, rapid dilution of the toxic gas is the first line of defense. However, the solvents hood in the PV Lab is constantly in use and a large tube furnace would occupy the entire area. Instead, a vented external enclosure was built using $\frac{1}{4}$" thick clear Lexan (a thermoplastic polycarbonate) sheet. This plastic is frequently used for impact applications such as industrial safety glasses, machine guards and football helmets. When thick enough (1.25"), Lexan laminates can stop bullets. Although 4 % H_2S is not flammable, concentrations higher than this can ignite (autoignition temperature is 260 °C [20]). In the event of an over-pressurization scenario with flammable gas, the impact-resistant Lexan serves as a shield during an explosion event.

However, the primary function of the clear Lexan is simply as a vented enclosure. The rectangular enclosure sits over the furnace with enough space to work inside. It has two doors for access to each end of the quartz tube. These doors are removable for wider access (as is the roof), but during an experiment the doors must be kept closed or with an opening no wider than 8" for each door. This is to ensure approximately 100 cfm (cubic feet per minute) air flow at each door opening. The enclosure is not constructed to be air-tight. It is specifically designed to allow some air from the

lab into the enclosure. This ensures the enclosure is maintained at negative pressure compared to the room (like a chemical hood). In the event of a leak, the direction of air flow is from the room, into the enclosure, thus reducing the probability an H_2S leak would spread to the rest of the room.

There is also an electrical enclosure around the furnace heating elements, to prevent shock, electrocution or burns from the nichrome elements. The table surface that supports the furnace frame is made of $\frac{1}{4}$" thick aluminum sheet and is grounded.

Emergency shut-off

In the event of an H_2S leak, and particularly if the building exhaust also shuts down, people should leave the lab immediately. There may not be time to shut down the furnace properly, thus an external shut-off switch was installed. This switch is a circuit breaker that, when pressed, cuts power to specific circuits that run all systems of the furnace. The switch was installed in the anteroom of the lab, through which everyone must pass to exit the lab.

Activating the anteroom emergency shut-off switch cuts power to the furnace heating elements and also cuts power to a magnetic starter switch that controls H_2S flow. The mechanism which allows control of H_2S flow by an electrical circuit required several intermediate switches and valves. The separation of the electrical circuit from the area of H_2S gas flow is a priority for flammable gases.

A pneumatically operated open/close valve is used to physically control the flow of H_2S gas from the regulator to the MFC. This pneumatic valve is actuated by compressed air pressure (house-supplied). When there is no compressed air pressure, the valve is closed. When 100 psi is applied, the valve opens and allows gas flow.

The compressed air flow is controlled by a standard 3-way normally-closed solenoid valve. This solenoid valve is operated by 240 VAC power. When the solenoid valve is de-energized, no compressed air flow is allowed to flow and the pneumatic valve is shut. When the solenoid valve is energized, it allows flow of 100 psi air to the pneumatic valve, which opens the valve and allows H_2S flow.

Power to the solenoid switch is controlled by a magnetic starter switch. These

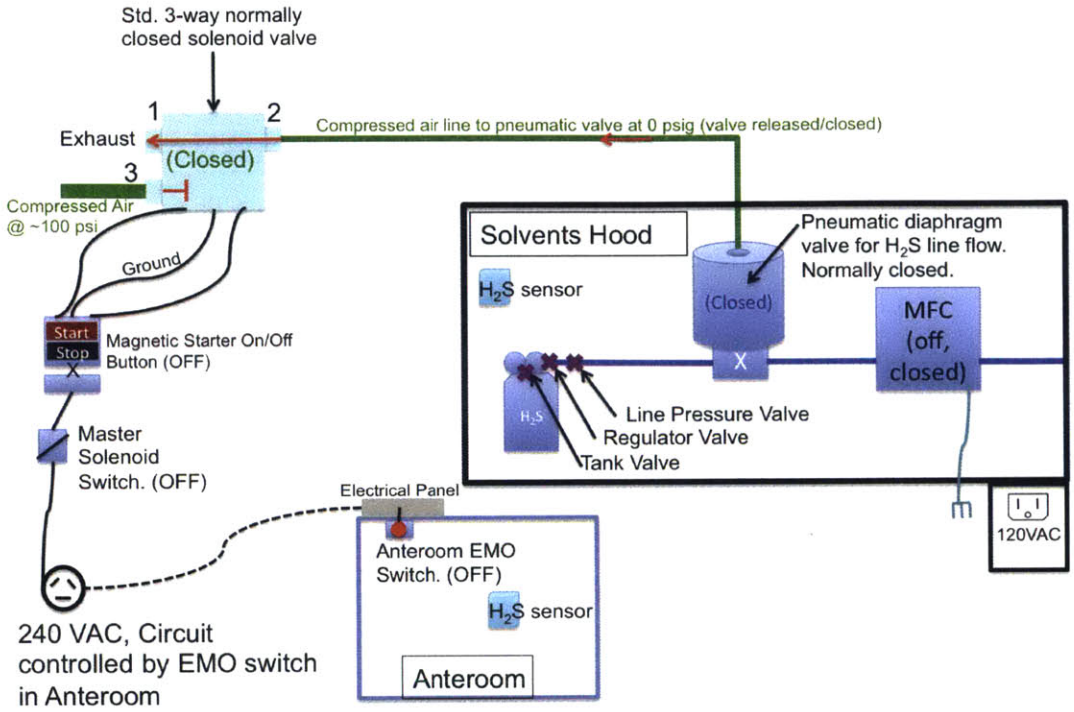

Figure 4-5: H_2S safety valve in de-energized state. Diagram is not to scale. It shows the electrical and gas valves in their off-state, needed to create the H_2S safety valve shut-off system.

types of switches, when energized, use an electro-magnetic coil to stay in an energized state. When power is cut, a spring physically separates the two leads that are completing the circuit. This means that without a physical force to press the two leads together (a.k.a. a person pressing the "Start" button), the circuit will not re-energize after a loss of power. When the "Start" button is pressed, 240 VAC power is allowed to power the solenoid valve on, which then allows compressed air to flow to the pneumatic valve, which then allows H_2S flow.

The magnetic starter switch is powered by the circuit which is a connected to the EMO switch in the anteroom. Thus when this EMO switch is pressed, the circuit power is cut, creating a cascading series of switch shut-offs, leading to the halt of H_2S gas flow. All of these switches are normally-closed, meaning should any one of them

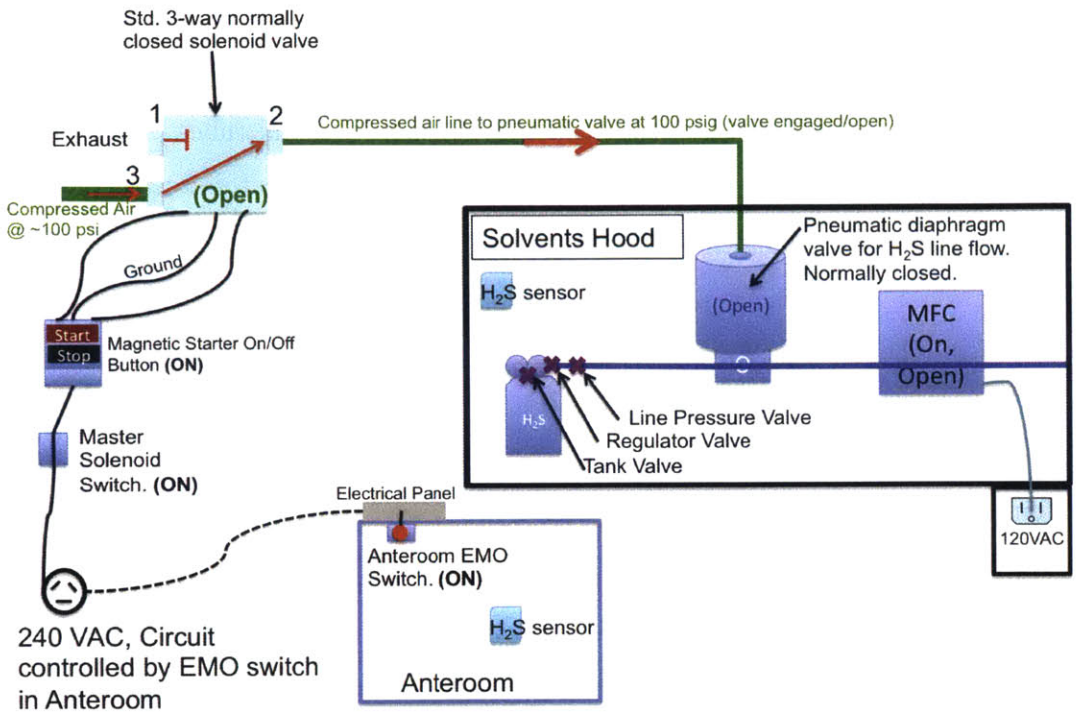

Figure 4-6: H_2S safety valve in energized state. Diagram is not to scale. It shows the electrical and gas valves in their on-state, needed to create theH_2S safety valve shut-off system.

fail, the whole series of switches will not work.

A second method of shutting off H_2S flow exists in the MFC. The MFC is powered by a 120 VAC outlet that runs off of power supplied to the solvents hood. This outlet is connected to the solvents hood EMO system, which shuts off any time there is not enough exhaust flowing through the hood. Thus during an emergency exhaust shutdown event, the MFC cannot be powered on. This MFC is also normally-closed and will prevent H_2S flow.

A visual diagram of these safety systems can be seen in Figure 4-5 and 4-6, showing the de-energized (no flow allowed) and energized state (flow allowed) of the H_2S safety valve system.

Backup pump power

In the event of an unexpected power shut off, the H_2S gas flow would shut off and the heating elements would shut off, as explained above. However, the pump would also shut off, leaving H_2S gas trapped in the furnace pipes and tubes. A safe way to evacuate this gas is needed. The SulfaTreat H_2S-absorbing material is useful here because it can reduce the H_2S gas content.

It is would be beneficial to have the oil pump still running during an electrical shut down. The pump will draw any remaining H_2S gas through the SulfaTreat trap, thereby purging the system of toxic gas. This makes the system safer upon start-up and does not allow H_2S gas to sit in the system for prolonged periods of time during an emergency.

Power for the pump to run for 20 minutes is supplied by an 1300 Ah backup battery or uninterruptible power supply (UPS). This backup battery is actually designed for computers and servers and can provide back up power within milliseconds of building power failure. These types of UPSs were not designed for high current loads. During normal operation, the oil pump (Edwards RV12) draws approximately 3 amps of current. This would normally be fine for a UPS, but during start-up a pump draws much higher current. When an oil pump is first turned on, it can draw upwards of 30 amps for several seconds. A UPS will not allow this level of current draw, so an automatic transfer switch (ATS) was also installed.

The role of the ATS is to act as a switch for the oil pump power. It monitors the quality of the power supplied by the building (or utility company). As long as good-quality building power is supplied, the ATS directs the oil pump current draw to the building-supplied power. When the building power is of low-quality, or shuts off unexpectedly, the ATS detects this and switches the oil pump power supply to the UPS backup battery. The key to this operation is that the oil pump must be *already on*. As stated previously, the pump draws 3 amps during continuous operation. This is a current draw that the UPS can handle. The UPS will then supply approximately 20 minutes of continuous, uninterrupted operation, allowing the pump to clear out

trapped H_2S gas from the furnace and gas lines.

Sensors and detection

While adequate exhaust is the first line of defense during an H_2S leak, the second line of defense is detection by H_2S sensors. There are five H_2S detection units in the lab, spread over different areas. They are designed as personal detection units for oil field workers and alarm at 10 ppm and 20 ppm, although they begin detection at 1 ppm. These detection limits are set by OSHA standards.

Perhaps more important is the knowledge that the human nose is highly sensitive to H_2S. It can be detected by the nose around 50 ppb, but does not pose a hazard to humans until 1–10 ppm. However, the human nose starts to become desensitized to the smell around 50 ppm, perhaps leading one to believe the danger has passed. This is why the sensor alarms are in place, instead of just relying on a persons sense of smell.

Exposure limits and notable thresholds are listed below, in order of increasing concentration:

50 ppb – Odor threshold (begin to smell)

1 ppm – ACGIH (American Conference of Governmental Industrial Hygienists), 8-hour Time Weighted Average (TWA)

5 ppm – ACGIH Short-term exposure limit (STEL)

10 ppm – NIOSH Recommended Exposure Limit (REL) over 10 minutes

20 ppm – OSHA Permissible Exposure Limit (PEL),if no other exposure occurs in an 8-hour work shift

30 ppm – AIHA ERPG-2 (emergency response planning guideline) (maximum airborne concentration below which it is believed that nearly all individuals could be exposed for up to 1 hour without experiencing or developing irreversible or other serious health effects or symptoms which could impair an individual's ability to take protective action)

50 ppm – Ability to smell H_2S begins to dull

100 ppm – NIOSH Immediately Dangerous to Life or Health (IDLH)

4.4 Analysis of gas by RGA (residual gas analyzer)

The decision to add an RGA (or mass spectrometer) to the furnace is primarily motivated by the desire to measure sulfur gas partial pressure. As seen in Chapter 3.4, the Kröger-Vink model suggests that P_{S_2} is one of the variables used to change majority carrier concentration. The ability to measure this value allows the use of a scientific variable (P_{S_2}), rather than an engineering variable (H_2S/H_2 flow ratio), when changing the sulfur content of an anneal. This scientific variable should, in principle, be more easily transferred to other annealing systems.

4.4.1 RGA specifications and operating conditions

A Hiden HPR-20 mass spectrometer was purchased for the purpose of analyzing gas that flows through the furnace. It uses a thoria (ThO_2) coated iridium filament that generates electrons by thermionic emission. These electrons impact gas molecules flowing in from the furnace. Some fraction of the gas molecules are ionized and they flow through a RF quadrupole mass analyzer that filters for m/z ratio (mass-to-charge ratio). These ions are detected either by a Faraday cup or secondary electron multiplier (SEM). This analyzer has a range of 1–200 amu and a practical pressure range in the H_2S furnace of 11 torr to 760 torr, depending on the capillary diameter and length used.

After much trial and error, ideal settings were found for this furnace gas mixture. Electron energy is typically set at 70 eV, while emission current is set to 350 μA. The mass spectrometer chamber pressure is maintained at 4×10^{-6} torr and the Faraday detector is used for all majority concentration gases and while the SEM detector is used for minority concentration gases.

Gas entry from the furnace to the mass spectrometer is allowed through a heated

stainless steel capillary tube. This capillary is attached to the rear end cap of the furnace by a quick-disconnect coupling. The stainless steel capillary is ideally heated to 200 °C along its whole length, thereby preventing the deposition of sulfur material inside the capillary tube (typically setting 1). The capillary allows pressure from the H_2S furnace to drop to an appropriate lower pressure needed in the mass spec chamber. A bypass valve that pulls gas directly to the scroll pump is also used as a mass spec chamber pressure adjustment mechanism. When the bypass valve is closed, all of the gas from the furnace goes into the mass spec chamber and the pressure in this chamber rises. This can create a stronger signal because there are more gas molecules to ionize, but a pressure that is too high will shut off the filament. During operation, it is important to maintain the same pressure in the mass spec chamber as was used during calibration. The mass spec chamber pressure is directly proportional to the total signal measured by the RF analyzer and detectors. As the pressure in the H_2S furnace chamber changes, the pressure in the mass spec chamber can be maintained at a constant value by adjusting the bypass valve.

During experiments that use the RGA, several gas species are monitored: H_2S, H_2, S_2, N_2, O_2, H_2O, Ar, and CO_2. While only the H_2S, H_2 and S_2 partial pressures are immediately important for the experiment, the other gases measured are also useful to record. The levels of H_2O, O_2, Ar and CO_2 present during the anneal can offer hints of the current leak rate of the furnace.

4.4.2 Calibration of H_2S and H_2 gas

H_2S and H_2 gas are easily calibrated using a pre-mixed gas tank of 3% H_2S, 1 % H_2, and 96 % N_2 (from Airgas). This mixture closely approximates gas conditions used in the furnace during annealing. This gas mixture is flowed through the furnace and RGA with the same flow rate as is used during annealing experiments and also adjusted to the same total pressure used in the furnace. The signal intensity from the mass spec detectors is measured and compared against the known H_2S and H_2 concentrations from the gas tank. A calibration factor is determined, which is then applied to the signal intensity of H_2S and H_2 during the experiment.

4.4.3 Calibration of sulfur gas

Obtaining a calibration factor for sulfur gas or more specifically S_2 gas is significantly more challenging. Sulfur is not gaseous at room temperature and will condense to a liquid at temperatures significantly higher than for H_2S and H_2. The phase diagram of sulfur shows the gas/liquid phase boundary for the relevant pressure range (Figure 4-7). The red dotted line in the figure indicates the sulfur partial pressure at the SnS/Sn_2S_3 phase boundary for SnS films at 400 °C. It intersects the gas/liquid phase boundary at ~175 °C. This means that all parts of the furnace and RGA must be at 175 °C or higher, to make sure sulfur gas does not condense to a liquid before reaching the ionization chamber in the mass spec. If this happens, the mass spec will read a lower sulfur partial pressure than the SnS film experiences in the H_2S furnace. To avoid condensation, the third zone can be heated up to 200 °C and the RGA capillary is also heated to 200 °C.

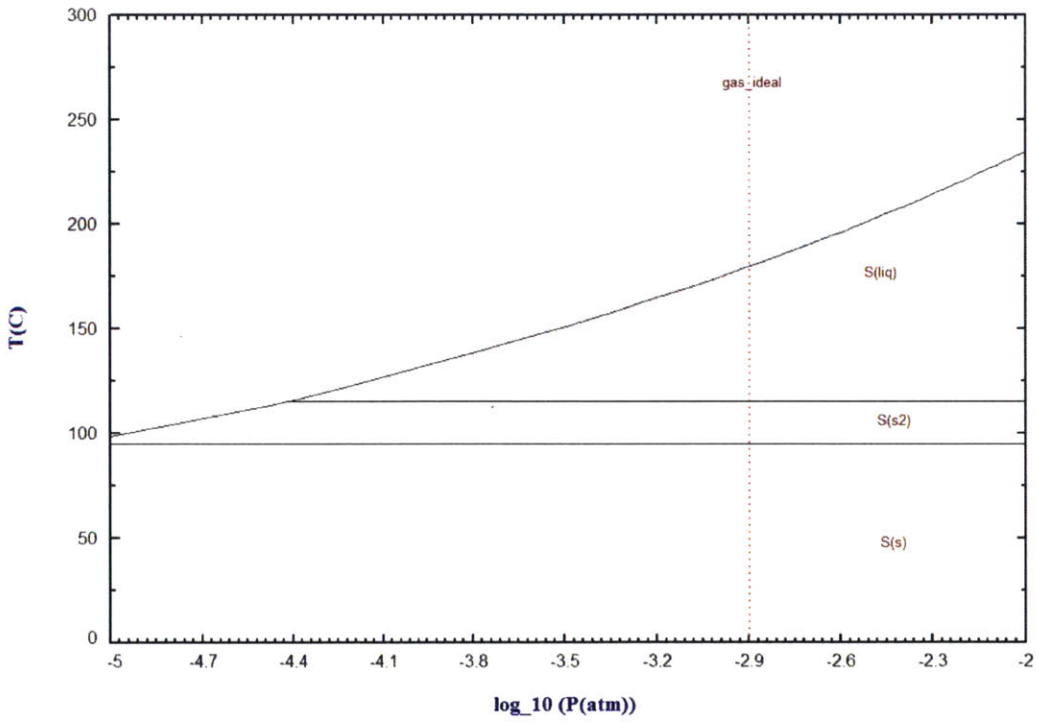

Figure 4-7: Sulfur phase diagram T vs. P plotted using FactSage. The vertical red dotted line marks the sulfur partial pressure at the SnS/Sn_2S_3 phase boundary at 400 °C. It intersects the gas/liquid sulfur phase boundary at ~175 °C.

An additional sulfur gas phase diagram highlights another problem with trying to measure sulfur partial pressure. Unlike oxygen, for which is is fairly easy to measure P_{O_2}, sulfur gas forms many molecules of different size. Specifically, S_2–S_8 are all possible and thermodynamically stable forms of sulfur gas molecules. Their individual partial pressures from 0–300 °C are plotted in Figure 4-8. The RGA used in these experiments is limited to 0–200 amu (or m/z) detection, therefore S_8^+ (256 amu) and S_7^+ (224 amu) ions cannot be detected.

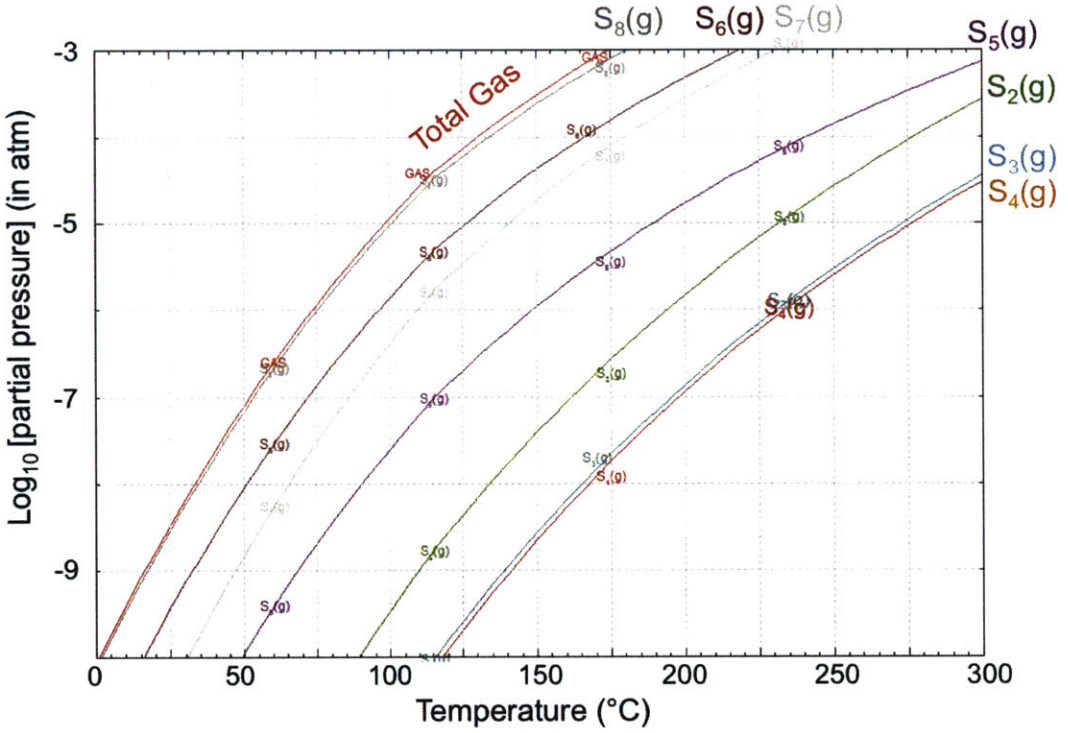

Figure 4-8: Sulfur gas species concentrations plotted $\log(P_{S_x})$ vs. T.

Many of the sulfur molecules will fragment into smaller molecules (e.g. an $S_8 \rightarrow 2 \times S_4^+$ or $4 \times S_2^+$). Most molecules have a "cracking pattern" that is recorded in a NIST database. However, each type of mass spectrometer will have its own unique cracking pattern for each molecule, based on its own configuration and settings.

Isotopes are another complicating factor to be considered. As an example: the S atom has 4 stable isotopes. The two most abundant ones are ^{32}S (94.4 %) and ^{34}S (4.3 %). Oxygen has three stable isotopes: ^{16}O (99.8 %), ^{17}O (0.04 %), ^{18}O (0.2 %).

The singly-charged $^{16}O_2$ molecule will have an m/z = 32, while an S atom will also have a peak at m/z = 32. The singly-charged $^{16}O^{18}O$ molecule will have m/z=34, which still overlaps the 4.3 % abundant ^{34}S, and additionally overlaps the H_2S mass also at m/z = 34. The presence of oxygen in the furnace system makes RGA data difficult to interpret, but not impossible. Generally, both oxygen and water vapor signals must be derived from their unique peaks and known cracking patterns (supplied by Hiden Analytical). When appropriate, the oxygen and water vapor signal contributions must be subtracted from any m/z peak related to sulfur.

Methods

A sulfur calibration chamber was constructed to measure known amounts of vaporized sulfur gas. This chamber is made of KF stainless steel fittings, flexible stainless steel pipe, and several high-temperature valves (not H_2S resistant). The chamber can be pumped down to approximately the same base pressure as the H_2S furnace. It has a thermocouple attached to the outside of the chamber and it is held inside a box oven. The box oven maintains stable temperatures from 25–300 °C. Stainless steel pipes are used for gas flow out of the box furnace and as a connection from the chamber to the RGA capillary. Heat tape is wrapped around all areas of pipe outside the box furnace and thermocouples are used to try to maintain the same temperature in the tubes as in the box furnace.

First, a small amount of sulfur (S_x, ≥99.998 % pure, Sigma Aldrich) powder is placed in an aluminum dish inside the chamber. The chamber is pumped down and purged with N_2 three times. N_2 is held in the chamber while the chamber heats up and the sulfur powder vaporizes. As the box oven and chamber heat up, the valves are shut and the chamber is essentially a closed system at a fixed temperature. The box oven, chamber, and heat tape are held at a fixed temperature (such as 150 °C) for 24 hours. In this time, the chamber is coming to equilibrium with an N_2 background pressure and a sulfur liquid-gas present. The concentration of each species of sulfur molecule can be predicted from FactSage, using Figure 4-8.

After 24 hours, the gas in the chamber is allowed to flow immediately into the RGA

capillary. The RGA is operating under conditions ideal for annealing experiments. As the gas flows from the chamber of fixed volume, through the RGA, the mass spec chamber pressure is maintained by slowly closing the bypass valve. This procedure can be repeated for several other temperatures from 100–200 °C to obtain several different concentrations of S_x vapor to measure.

The mass spectrum pattern achieved by this method showed strong oxygen and water vapor contamination, but also a strong S_2 peak at m/z=64. It is suspected that excess oxygen and water vapor leaked in during the 24-hour waiting period. Long wait-times were used to ensure the chamber would be at equilibrium. The strong S_2 signal was also accompanied by weaker than expected S_3, S_4, S_5, S_6 peaks. This author suspects the larger S_x fragments were broken into primarily S_2^+ and S^+ fragments, thereby making a true comparison to equilibrium S_x gas partial pressures difficult. However, from the expected partial pressures of the S_x gas species, one can predict the concentrations of S_2^+ and S^+ fragments one could expect, assuming all S_x molecules break down into S_2^+ and S^+ fragments. This is perhaps more representative of what the RGA is measuring. One could define a "sulfur content" calibration simply as the number of sulfur atoms detected, using the above assumptions.

Kröger-Vink defect theory assumes the S_2 molecule is the primary driver of majority carrier concentration change. However, it is unclear whether other sulfur molecules could be involved. If an S_8 molecule lands on the surface of SnS, it may still contribute S atoms to the crystal lattice, thereby generating tin vacancies. This is not a common issue for oxygen-based Kröger-Vink defect theory and thus is not a topic that has been deeply explored. For this reason, the author feels that "sulfur content," defined as the number of sulfur atoms in the gas could be an acceptable substitute for S_2 gas pressure, given the difficulties of calibration with the RGA in use.

Because "sulfur content" is not a true S_2 gas calibration, annealing experiments using this calibration method are referred to as "semi-quantitative." The challenge of more accurate sulfur gas calibrations will remain a topic for later research.

4.5 Summary

An H_2S annealing furnace was designed and built to anneal SnS films while recording gas composition data using an RGA. This furnace contains several unique safety systems and back-ups. It is capable of flowing 100 % H_2S gas, although currently 4 % is being used. By switching out the quartz furnace tube, it could be used with many sulfur-based systems with little risk of cross-contamination. The third zone also allows for experimental flexibility, particularly with respect to sample quenching and loading.

The H_2S furnace, "semi-quantitative" sulfur gas calibration, and quenching mechanisms will be used in the next chapter, to help elucidate properties of SnS films after annealing.

Chapter 5

Annealing SnS films in H_2S/H_2 gas mixtures

Chapter 3 outlined the reasons why annealing in H_2S gas could be beneficial for SnS. The chapter also defined some goals for annealed films, which may lead to improved photovoltaic performance.

The first section of this chapter presents preliminary results of an annealing study where P_{S_2} was the primary variable. Temperature and time of anneal were also investigated. These anneals were performed on as-deposited thermally evaporated SnS films. The initial starting conditions were selected based on external evidence of successful annealing to improve SnS solar cell efficiency.

The third section of this chapter outlines a design of experiment that attempts to minimize the impact of kinetics on annealing results. With this design, the impact of varying anneal temperature and sulfur partial pressure are explored.

5.1 First results of annealing in H_2S/H_2 mixture

5.1.1 Methods

SnS films approximately 600 nm thick were grown on Corning XG glass for Hall and van der Paw measurements and on $Si/SiO_2/Mo$ for grain morphology analysis, which

is more applicable to devices. These films had deposition parameters listed in Table 2.3.

Samples were annealed in the Main zone of the furnace, while sitting on a cleaned quartz plate 1 mm thick. Samples were within 1" of the thermocouple, ensuring their temperature to within 10 °C of the measured value. After loading the samples, the furnace tube is sealed and pumped down to base pressure (typically < 20 mtorr). Then the furnace and gas tubes are purged with N_2 gas three times. The furnace is then allowed to pump back down to base pressure.

Gas flow parameters and total pressure are established before heat is applied. Heating ramp time remains constant for all anneals, at 10 minutes from room temperature to plateau temperature. The gas conditions are not changed until the sample cools below 70 °C. The samples were allowed to cool in the hot zone, after the heating elements are turned off at the end of the plateau time. Typical cooling time is around 30 minutes to reach 70 °C. The RGA begins measurement before heat is applied. For these experiments, the emission current = 100 μA, electron energy = 70 eV, mass spec chamber pressure maintained at 3×10^{-6} torr and only the SEM detector was used. The H_2S and H_2 gases were calibrated, but the S_2 value is not. For these experiments, S_2 concentration is the uncalibrated peak intensity at m/z=64.

The range of annealing conditions performed are listed in Table 5.1

Sample Label/ Goal	**Target $\frac{H_2S}{H_2}$ ratio**	**Plateau Temp (°C)**	**Plateau Time (min)**	**Total Flow Rate (sccm)**	**Total Press. (torr)**
Low S_2	0.10	400	60	100	28
Mid S_2	1.0	400	60	100	28
High S_2	10.5	400	60	100	28
Lower Temp	10.5	300	60	100	28
Short Time, High S_2	10.5	400	6	100	28
Short Time, Low S_2	0.10	400	9	100	28
N_2 only	N/A	400	60	100	28
H_2 only	N/A	400	60	100	28
H_2S only	N/A	400	9	100	80

Table 5.1: Parameters for first round of H_2S/H_2 annealing experiments on as-deposited films.

Samples were characterized by measuring majority carrier concentration and mobility by Hall and van der Pauw. Contacts on square samples are deposited by e-beam evaporation in a 20 nm Ti/200 nm Au stack. Film thickness was measured by cross-section SEM. This measurement has an estimated ±100 nm error. This error value is applied to all majority carrier concentration data and displayed as error bars. The statistical error in the Hall measurement, as determined by a goodness of fit (R^2), is frequently less than 1 %. Although as-deposited films with carrier concentrations in the 10^{15} cm^{-3} range tend to have a larger statistical error due to low mobility and low carrier concentration.

The largest source of error in the Hall measurement comes from contact displacement (a contact not on the edge of the sample). This creates an offset estimated to be at most +10 % for all samples. Most sample contacts were correctly placed and small compared to the sample size. However, one contact on a couple samples was displaced up to 1 mm. This causes an underestimation of carrier mobility [37], which is displayed as a 10 % error bar on plots of majority carrier mobility.

Grain size is determined by hand-tracing plan-view SEM images taken at 50 kX magnification using a field-emission SEM. Hand-tracing the grain boundaries of each grain was necessary due to the uneven nature of the surface of the films, which creates contrast in the SEM image. This contrast cannot currently be resolved by automatic image segmentation code. After tracing grain boundaries, grain areas were calculated using ImageJ software.

5.1.2 Results

Electrical

The majority carrier concentration (Figure 5-1) and mobility (Figure 5-2) results of each sample in Table 5.1 are presented. Each sample that was annealed also had a "sister" sample from the same substrate. Each "sister" sample is plotted (green triangles) to align with its annealed sibling such that the two paired samples align vertically. This highlights the change in carrier concentration or mobility for

each sample. These figures also highlight the spread in as-deposited characteristics. Note that as-deposited samples did *not* experience different P_{S_2}, only the annealed "sister" sample did. Each data point also has its sample label written near it, for easy reference.

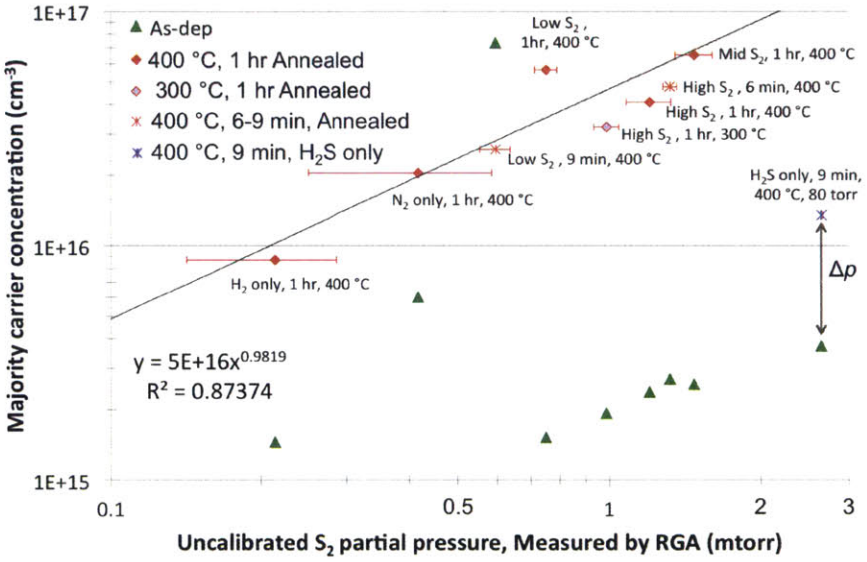

Figure 5-1: Changes in carrier concentration after annealing as-deposited films with different H_2S/H_2 ratios. Green triangles indicate the as-deposited "sister" of the annealed sample, cleaved from the same substrate. All as-deposited samples had the same deposition conditions and are not related to the x-axis S_2 partial pressure. Red and blue markers indicate different annealing conditions. The solid red diamonds are used as data for a power-law trendline fit, showing a $\log(p)$ vs. $\log(P_{S_2})$ slope of 0.98. The x-axis is sulfur content is measured at m/z=64, using an uncalibrated RGA.

For samples which are directly comparable (400 °C plateau temperature, 1 hour plateau time, 28 torr total pressure), plotted with solid red diamonds, the data is fit and a slope is derived for the dependence of $\log(p)$ vs. $\log(P_{S_2})$. It is observed that this dependence is 0.98, although the R^2 value is somewhat low. From Kröger-Vink equations on the dependence of $[p]$ on P_{S_2} (Equation 3.17), the expected slope is $\frac{1}{6}$, or 0.167.

Of particular note are the "Short Time" anneals. These films were at the plateau temperature for 6–9 minutes, but still held approximately the same trend as the 1

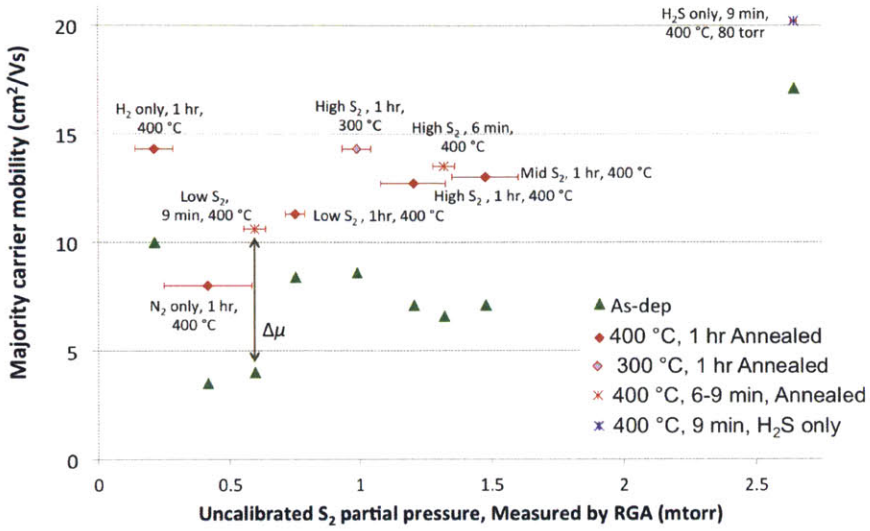

Figure 5-2: Changes in mobility after annealing as-deposited films with different H_2S/H_2 ratios. Green triangles indicate the as-deposited "sister" of the annealed sample, cleaved from the same substrate. All as-deposited samples had the same deposition conditions and are not related to the x-axis S_2 partial pressure. Red and blue markers indicate different annealing conditions. The x-axis is sulfur content is measured at m/z=64, using an uncalibrated RGA. No apparent trend is observed with sulfur partial pressure.

hour annealed samples. This suggests the changes happening to as-deposited films can be rapid. The "Low Temp" sample, annealed at 300 °C, also lies on a similar trend line as the 400 °C data.

There are two samples which were designed as controls: the "H_2 only" and "N_2 only" conditions. However, these samples did not turn out to be good controls because there was still a significant and measurable amount of sulfur in the gas flow. It was not possible to determine whether the unexpected presence of sulfur came from the sample, the furnace tube walls, or was residual sulfur trapped in the RGA itself. For the purposes of the study, it is assumed that these two samples were actually exposed to the measured amount of sulfur.

The datapoint labeled "H_2S only" appears to be on a different trend line than the rest of the data. It did not involve any H_2 gas mixing and was also annealed with a different total pressure than the other samples. The purpose of these anneal settings

was to increase the total amount of S_2 exposed to the sample. This was successful, although the results unexpected. This particular as-deposited sample had a different film morphology when examined by SEM, and also had an usually high mobility for an as-deposited film. This suggests there may be other parameters affecting the results of this sample.

The majority carrier mobility of all samples is shown to increase, but there is no observable trend with S_2 partial pressure. The increase in mobility ranges from 2–6 cm^2/Vs. These increases are modest but likely beneficial for solar cell performance. At this time, the cause of the observed mobility increase cannot be determined. However, a likely explanation is grain growth and structural defect reduction during annealing. Another possibility is the reduction of mid-gap defect states.

The x-axis on each of these plots is labeled as uncalibrated. To determine the uncalibrated S_2 partial pressure, the signal at m/z=64 was used. In the simplest case

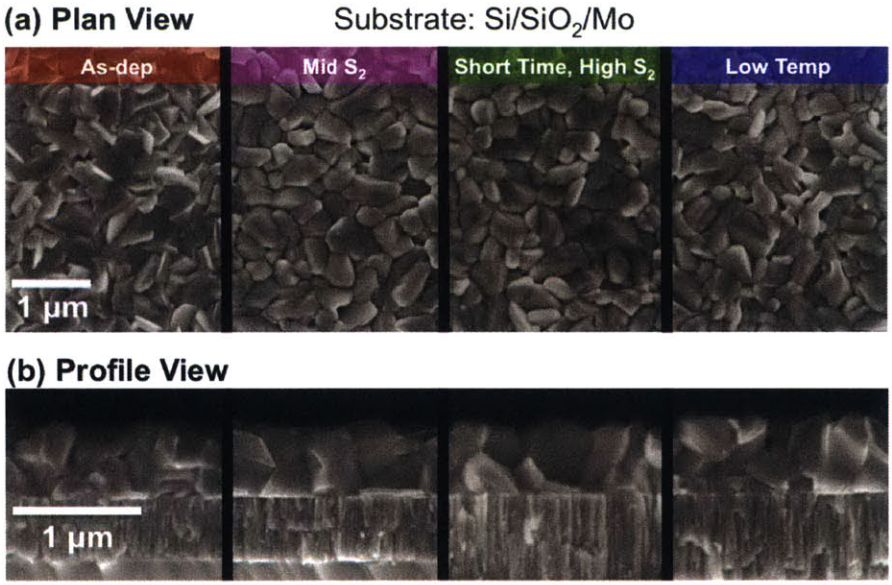

Figure 5-3: Plan (a) and profile (b) view SEM of selected annealed samples. Images show significant grain growth, although it is hard to discern differences between the different annealing conditions by eye.

case, this corresponds to a singly charged S_2^+ ion, because the mass of a sulfur atom is 32 amu. At the time of these experiments, a calibration method did not exist for S_2

gas. The "semi-quantitative" sulfur content calibration method discussed in Chapter 4.4.3 was developed for the next set of experiments performed in Chapter 5.3.

Morphology

Notable SEM images on molybdenum substrates are shown in Figure 5-3. Images on Corning XG glass also show grain growth. However, the grain structure on molybdenum is seen as more relevant for devices and is reviewed here. At first glance, there is a clear difference between the as-deposited sample and all of the annealed samples. However, the differences between the annealed samples is harder to discern by eye.

To examine more subtle grain size changes, a grain size analysis is performed and plotted in Figure 5-4. Each population of grain areas is presented in a cumulative

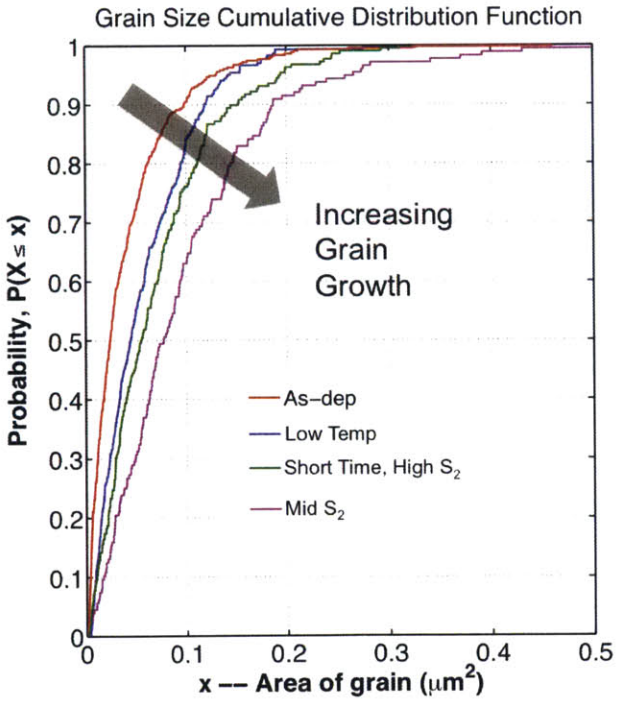

Figure 5-4: Grain size cumulative distribution function for annealed samples shows clear differences between grain area of the as-deposited film and the annealed films. The "Mid S_2" annealing condition was found to have the greatest grain growth.

distribution function. In this type of plot, the y-axis gives the probability of finding a grain of a particular size *or smaller* (the size is read from the x-axis). For example,

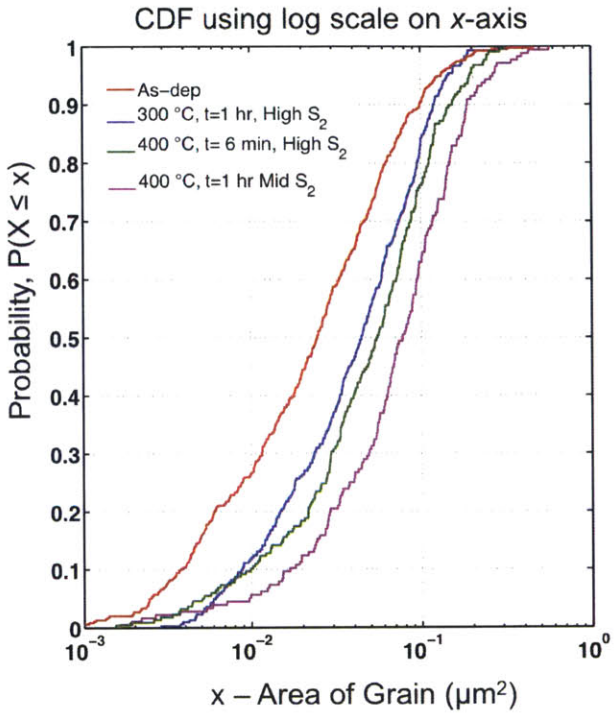

Figure 5-5: Grain size cumulative distribution function for annealed samples, plotted using log scale on x-axis. The same samples are shown as in the previous figure.

let us examine the data from the as-deposited film (red curve). For any random grain we pick in the film, it will have a 90 % chance of being 0.1 μm^2 or smaller. When we look at the "Mid S_2" curve (magenta), we see that any random grain selected has only a 64 % chance of being 0.1 μm^2 or smaller. Thus there are more grains larger than 0.1 μm^2 in the "Mid S_2" film than in the as-deposited film. In general, as the curves push into the middle of the graph (following the gray arrow), the larger the grains become. Figure 5-4 shows the least amount of grain growth occurred for the "Low Temp" anneal, more for the "Short Time, High S_2" anneal, and the most for the 1 hour long "Mid S_2" anneal.

The same data is plotted again in Figure 5-5, but using a log scale on the x-axis. Difference between the data sets is more easily seen using this plotting method. This graph also highlights the log-normal distribution of the grain size area data.

XRD

All annealed samples were analyzed by using a θ-2θ XRD scan. Each film was found to still be phase pure to the limits of XRD detection. Films deposited on Corning XG glass or thermal oxide favored the (040) orientation, as shown in Figure 5-6. Annealing further emphasizes the (040) orientation on Corning XG glass.

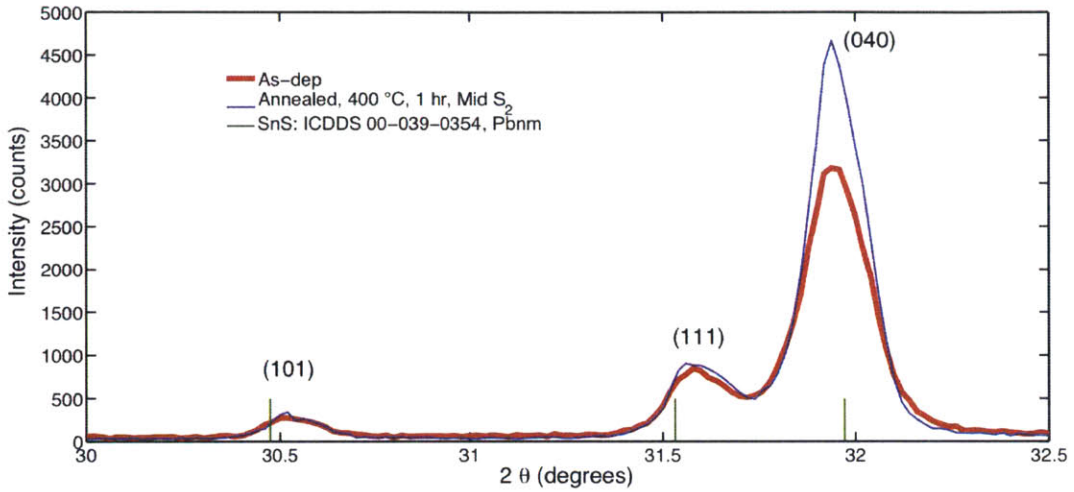

Figure 5-6: XRD comparison of as-dep and annealed film ("Mid S_2") on Corning XG glass. The film shows a strong preference for the (040) orientaiotion, which becomes even stronger after annealing. Films remain phase pure after annealing.

5.2 Addressing kinetic considerations

Before continuing further experiments, it is necessary to consider the issue of applying thermodynamic models (Kröger-Vink and DFT) to real-world systems that are affected by kinetics. Care must be taken to design experiments so that the results are easily compared to thermodynamic predictions.

As shown during discussion the of Kröger-vink defect model, the variables that are expected to impact film carrier concentration are anneal temperature and sulfur partial pressure (P_{S_2}), and nothing else. However, during annealing there are many other experimental parameters to choose, such as plateau time, temperature ramp rate, cooling rate, total flow rate of gases, and total pressure. There are also

film properties that affect the Hall measurement, such as grain size (or grain boundary density), which can change for different annealing conditions and make samples difficult to compare.

5.2.1 Grain growth during annealing

In general, grain growth during annealing is considered beneficial for improved photovoltaic efficiency. However, it is a confounding factor when trying to establish a trend in mobility. A different density of structural defects, such as grain boundaries, can impact the mobility measurement. For this reason, it is desirable to keep the grain size constant over all annealing conditions. If this is achieved, one could begin to attribute changes in mobility to other factors, such as a reduction in point defect concentration.

One method of keeping grain size constant during an anneal is to "pre-grow" the grains. This requires a high temperature, long time anneal to allow large grain growth. A slow cooling step is preferred, because this may allow the carrier concentration to reach a lower level before finally "freezing" due to slow kinetics at lower temperatures.

Once the grains have been grown, this "large-grained" material may be re-annealed. Because the majority of the grain growth has already occurred, very little grain growth should occur on the second anneal. During the 2^{nd} anneal, the film is still exposed to an anneal temperature and P_{S_2}, the film should come to an equilibrium carrier concentration and mobility associated with the 2^{nd} anneal parameters.

Several experiments were performed to determine what this "large-grained" anneal should be. SnS films used for these experiments have the same deposition conditions on molybdenum (for grain growth) and SiO_2 (for electrical measurements). The Hall samples are now deposited on Si wafers with thermal oxide. These substrates are also used for devices, but with the molybdenum layer. Based on the previous set of experiments, temperatures and times that are higher and longer are chosen. The H_2S/H_2 gas mixture ratio was fixed at the "Mid S_2" level, because this condition showed the greatest grain growth previously. Total pressure was fixed at nominally 80 torr.

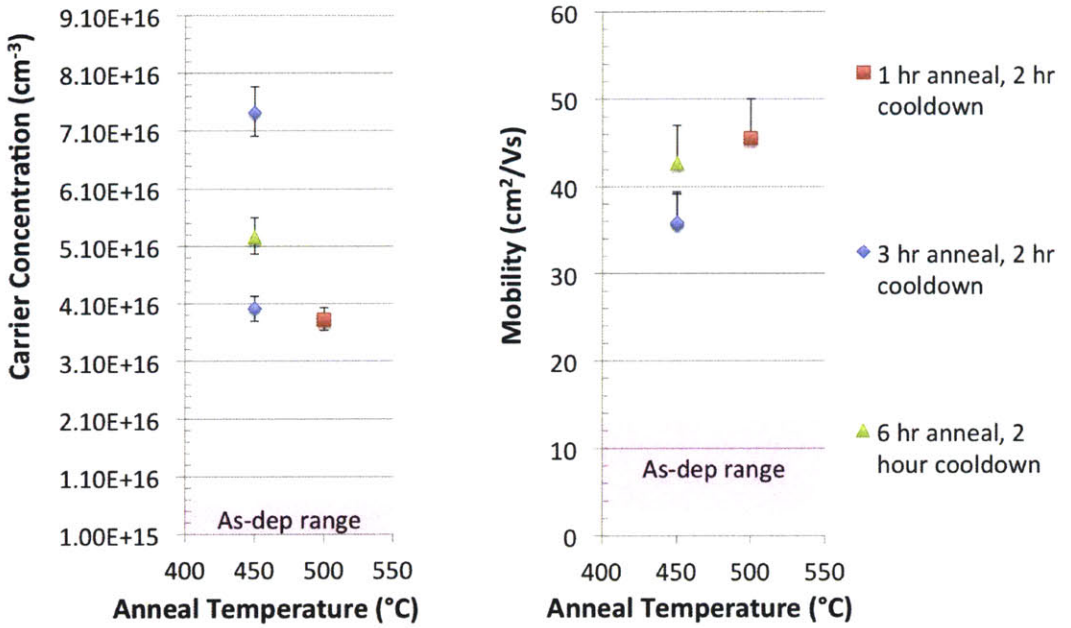

Figure 5-7: Carrier concentration (left) and mobility (right) are plotted for 3 different annealing conditions selected to encourage grain growth during the anneal. Carrier concentration error is derived from a ± 100 nm thickness measurement error. Mobility error bars show a correction based on largest observed contact displacement. Most samples have a much smaller correction.

Three anneal settings were explored: 450 °C anneal temperature for 3 hours, 450 °C anneal temperature for 6 hours, 500 °C anneal temperature for 1 hour. All samples had a 10 minute ramp time and a 2 hour linear cool down period to 70 °C. A 2 hour cool down (as opposed to a 30 min cool down) was selected as a practical upper limit on cool down speed.

Carrier concentration and mobility are seen in Figure 5-7. The carrier concentrations are in the same range as the previous set of experiments (Figure 5-1). The 2 hour cool down rate did not seem to have its intended effect of lowering carrier concentration. Mobility jumps up markedly and has promising implications for devices. Examining SEM plan-view images allows us to make a decision for which anneal will be a standard "large-grained" anneal.

Significant grain growth observed in both the Si/SiO_2 substrates and the $Si/SiO_2/Mo$

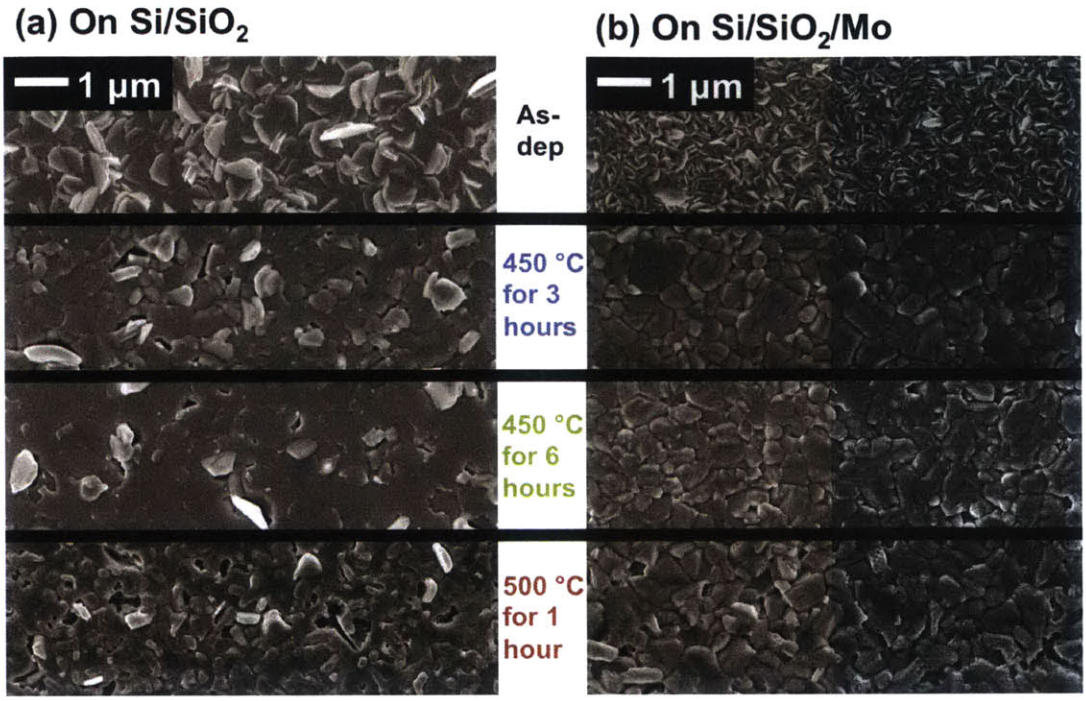

Figure 5-8: Plan-view SEM images on SiO_2 and Mo, for large grain growth anneal tests. 450 °C for 3 hours was selected as the best grain growth anneal because it did not cause excessive porosity in the films.

substrates (Figure 5-8). However, it is also observed that for the 450 °C for 6 hour anneal and the 500 °C for 1 hour anneal, the film appears to lose mass. Holes and pits can be seen in the surface. It is likely that 500 °C temperatures will evaporate the SnS film when the total pressure is at 80 torr, while 450 °C is on the cusp of evaporation. The 450 °C for 3 hour anneal is seen as most promising for device applications and will also serve as the "large-grain" anneal step for further material studies.

5.2.2 Cooling rate

An ideal experiment would measure carrier concentration and mobility of the sample while at the anneal temperature. This would eliminate any question of whether the sample properties are representative of an anneal temperature. However, that kind of setup is beyond the scope of this thesis and is made difficult by the corrosiveness of H_2S gas.

Instead, the samples are cooled rapidly to "lock in" the properties of the film at the anneal temperature. This method is also more applicable to SnS solar cells, since no traditional solar cell will be operated at 400 °C.

The difficulty of cooling rapidly is in the necessity of maintaing the H_2S/H_2 gas atmosphere around the sample. The sample cannot be dropped into water or oil without purging the furnace of H_2S first, while at the anneal temperature. Removing the source of sulfur prematurely, while still hot, may affect results if the film loses sulfur. Exposing the sample to air (or water) at high temperatures also leads to a thick oxidation layer.

A quench mechanism was designed to be operated from outside the furnace, using a magnetic coupling. The mechanism pulls a 1 mm thick quartz tray, which holds the samples and sits inside the hot zone during the anneal. When the magnetic coupling is slid along the length of the quartz furnace tube, the quartz tray is pulled out of the Main zone and into the 3rd zone. At a distance of 4" away from the Main zone, the 3rd zone is maintained at room temperature. The moving (and hot) quartz tray slides along two quartz rails, then hits an 8" long rectangular piece of silicon wafer, 850 μm thick, referred to as a silicon "runway." The quartz tray with the samples stops its movement because it hits the stationary piece of silicon (the silicon is prevented from sliding). However, the samples are not stopped because the quartz tray is slightly thicker than the silicon runway. The samples' momentum is used to continue traveling onto the room temperature silicon runway. The samples slide down the silicon runway and come to rest at the end of the 3rd zone. If one listens closely, a faint "weeeeeeeee!" can be heard from each sample.

The sample substrate (Si) can now cool rapidly on a large, room temperature piece of silicon. It is estimated that the film reaches room temperature within three minutes, although this has not been measured. Silicon was selected for both the substrate material and the "runway" material for its excellent thermal transfer properties and its cleanliness. Without extensive modification of the H_2S furnace, it is believed that this is the fastest cooling rate one can achieve within this furnace while still maintaining the gas atmosphere of the anneal.

5.2.3 Plateau time

The answer to "when is a material in thermodynamic equilibrium?" is beyond the scope of this thesis, but for the purposes of these experiments, will be considered. After the 1st "large grain" anneal step, the relevant question becomes "how long should the second anneal be, to ensure that the film has reached equilibrium in the annealing chamber?" To answer this question, samples that have undergone the "large grain" anneal step were annealed for 30, 60, 180 and 360 minutes at various temperatures and all with the "Mid S_2" condition. These samples were cooled using the quenching mechanism described in the previous section. It is assumed the carrier concentrations are representative of a film at the annealing temperature, due to rapid cooling. In this experiment, there were also two samples that start from the "as-deposited" condition, rather than the "1st annealed/Large grain" condition.

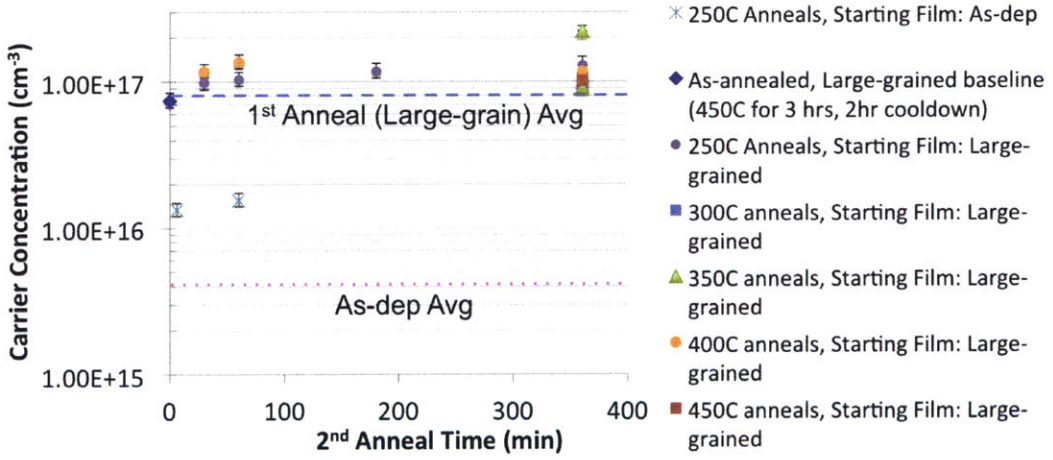

Figure 5-9: Carrier concentration of twice-annealed samples with various $t_{2^{nd}anneal}$ and $T_{2^{nd}anneal}$. Samples were first annealed using "large grain" conditions, then annealed a 2nd time. Two samples (teal stars) are annealed from as-deposited films instead, and only experienced the 2nd anneal conditions. The pink dashed line marks the average carrier concentration for as-deposited films. The blue dashed line marks the average carrier concentration after the 1st "large grain" anneal.

Figure 5-9 shows a slight increase of carrier concentration after the 2nd anneal. Examining results along different times of anneal reveals a spread in the data from a range of 0.9–2 $\times 10^{17}$ cm^{-3}. These results do not point to any one anneal time as long

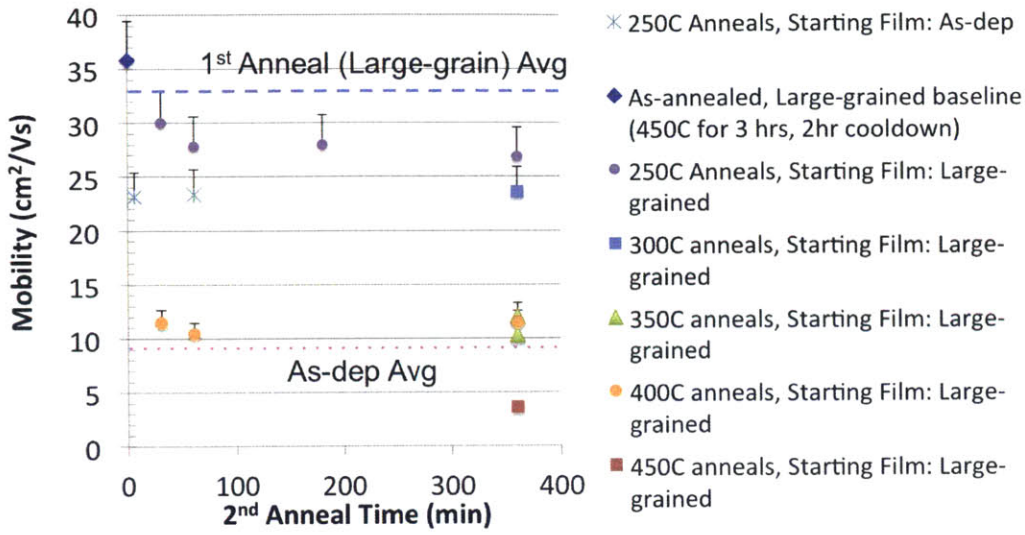

Figure 5-10: Carrier concentration of twice-annealed samples with various $t_{2^{nd}anneal}$ and $T_{2^{nd}anneal}$. Samples were first annealed using "large grain" conditions, then annealed a 2nd time. Two samples (teal stars) are annealed from as-deposited films instead, and only experienced the 2nd anneal conditions. The pink dashed line marks the average mobility for as-deposited films. The blue dashed line marks the average mobility after the 1st "large grain" anneal. The 2nd anneal + quench appears to have a deleterious effect on mobility as the temperature of the 2nd anneal increases..

enough to guarantee thermodynamic equilibrium of the film. Thus the 6 hour (360 min) anneal time is chosen, again as a practical limit.

Majority carrier mobility data is presented in Figure 5-10. It is interesting to note a decrease in mobility after the 2nd anneal. As the temperature of the 2nd anneal increases, the mobility drops further. The 250 °C anneals on as-deposited films also saw a strong increase in mobility.

Diffusivity calculation

In considering the length of anneal time, we perform one calculation to roughly see if it is feasible for these films to reach equilibrium in the time span of 30 min to 360 minutes. We use the equation: $x = 2\sqrt{Dt}$, where x = diffusion penetration distance, D = diffusivity of the mobile species, and t = time allowed for diffusion [9]. This formula provides the penetration distance, x, where the concentration of the diffusing

species has fallen off by approximately $1/e \approx 0.37$ of the concentration at $x = 0$ (the point source, or surface of the film in this case). The minimum diffusivity necessary for a diffusing vacancy or ion at the surface of the film to reach the substrate will be calculated.

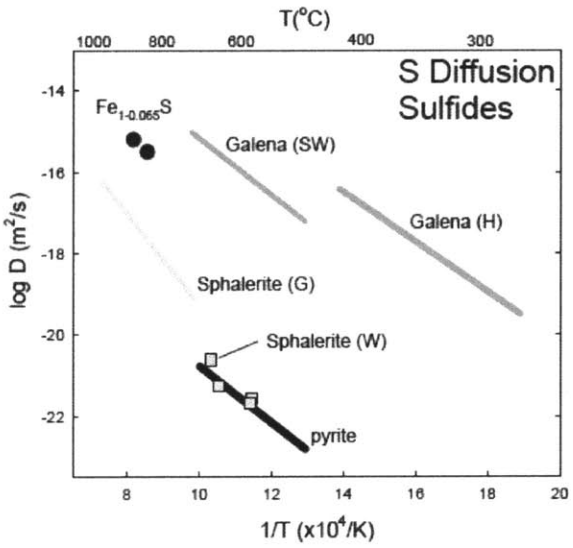

Figure 9. S diffusion in sulfide minerals. Sources for data: $Fe_{(1-0.065)}S$: Condit et al. (1974); pyrite: Watson et al. (2009), galena: SW – Seltzer and Wagner (1965), H – Hoeppener et al. (1990); sphalerite: G – Gobrecht et al. (1976); W – Watson et al. (2009).

Figure 5-11: Sulfur diffusivity in sulfides vs. temperature. Figure from Cherniak [16].

Set $x = 1\,\mu\text{m} = 1 \times 10^{-9}\,\text{m}$, which is the typical thickness of the SnS films.

Let $t = 6\,\text{min} = 360\,\text{s}$, because this is the shortest anneal time used for these experiments. The necessary minimum diffusivity calculated is: $D = 6.9 \times 10^{-16}\,\text{m}^2/\text{s}$.

Instead, using $t = 60\,\text{min} = 3600\,\text{s}$, the necessary minimum diffusivity calculated is: $D = 6.9 \times 10^{-17}\,\text{m}^2/\text{s}$.

Using $t = 360\,\text{min} = 21600\,\text{s}$, which is the longest anneal time for these experiments, the necessary minimum diffusivity calculated is: $D = 1.2 \times 10^{-17}\,\text{m}^2/\text{s}$.

A brief literature search on measured diffusivities in sulfide materials yields a review paper summarizing diffusivities for sphalerite (ZnS, zincblende), pyrite (FeS_2, cubic), galena (PbS, cubic), chalcopyrite ($CuFeS_2$, tetragonal or pseudo-cubic) [16]. Sulfur diffusion in sulfides is shown in Figure 5-11 and Fe diffusion in sulfides is shown in Figure 5-12. Both the cation and anion diffusivities are presented because at this

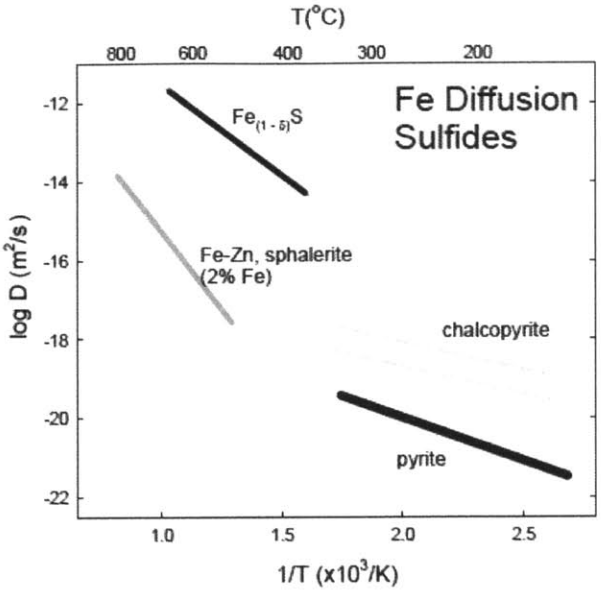

Figure 10. Fe diffusion in sulfide minerals. Sources for data: Fe-Zn interdiffusion, sphalerite – Mizuta (1988); Fe diffusion, chalcopyrite, pyrite – Chen and Harvey (1975); Fe diffusion, $Fe_{(1-\delta)}S$ – Condit et al. (1974).

Figure 5-12: Fe diffusivity in sulfides vs. temperature. Figure from Cherniak [16].

time it is not known which species diffuses in SnS during annealing.

Although no diffusivity data could be found for SnS, data from Cherniak offers a plausible range of diffusivities one could expect for SnS [16]. The minimum diffusivities calculated above suggest that it is possible the 1 μm thick SnS films have reached a near-equilibirums state after annealing for 6–360 minutes . However, there is still a strong possibility that 6 hour anneals are kinetically limited by diffusivities lower than $D = 1.2 \times 10^{-17}\,\mathrm{m}^2/\mathrm{s}$.

All of the materials in the Cherniak review paper are cubic or near-cubic, suggesting relatively isotropic diffusivities. Also interesting to note, the off-stoichiometric FeS material has a higher diffusivity than any of the other materials presented. Because of the large lattice spacing between the layer planes of SnS, it is possible that diffusivity along layer planes is much larger than diffusivity perpendicular to the layer planes. The anisotropy of the SnS crystal structure may still allow for the possibility of rapid diffusion.

5.2.4 H_2S/H_2 gas mixing

In Chapter 3.5.2, the issue of a kinetically limited reaction between H_2S, H_2 and S_2 gases was discussed. While the selection of data points to test are based on equilibrium predictions of S_2 content, the RGA was purchased because gas mixing and decomposition may be kinetically limited. The RGA allows the observation of gas content in real time. It is assumed that what is observed by the RGA is the same gas mixture that exists around the samples in the hot zone.

It is possible, for example, that temperature fluctuations along the length of the furnace affect the local gas composition. However, that issue will not be addressed in this thesis. It is observed that as heat is applied to the furnace, no change in gas content is registered by the RGA.

5.3 Second round of H_2S/H_2 annealing experiments

Based on the knowledge gained from the first round of experiments in Chapter 5.1, and the considerations of how kinetics impact the annealing conditions (Chapter 5.2), a new design of experiment is proposed. The goal is to isolate the impact of annealing temperature or P_{S_2} on majority carrier concentration and mobility.

5.3.1 Design of experiment

As-deposited samples (on Si/SiO_2 and $Si/SiO_2/Mo$), now 1 μm thick, will first be annealed to grow grains in a "large grain" annealing step. This anneal step is a 450 °C anneal for 3 hours with a 2 hour linear cool down, with total pressure at 80 torr and a "Mid S_2" gas mixture (4% H_2S at 50 sccm / 4% H_2 at 50 sccm, with 96% N_2 balance). Several samples will be removed at the as-deposited stage and the "large grain" stage for characterization by SEM, Hall and van der Pauw.

Next, individual samples will undergo a temperature sweep study. "Large grain" samples will be annealed at temperatures from 250 °C to 450 °C for 6 hours, all with a fixed gas total pressure of 80 torr and a "Mid S_2" gas mixture. This will test only

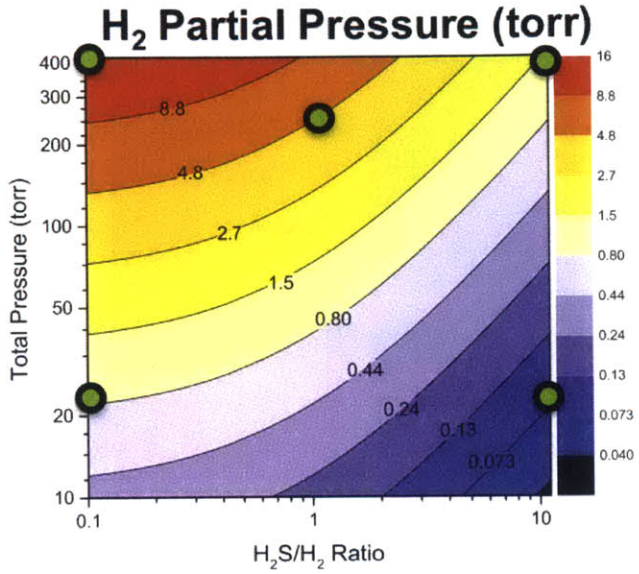

Figure 5-13: H_2 partial pressure contour map for different furnace parameters (total pressure and H_2S/H_2 ratio). Green dots show locations of experimental data points. Each axis is an experimental "knob" or parameter that can be adjusted on the H_2S furnace.

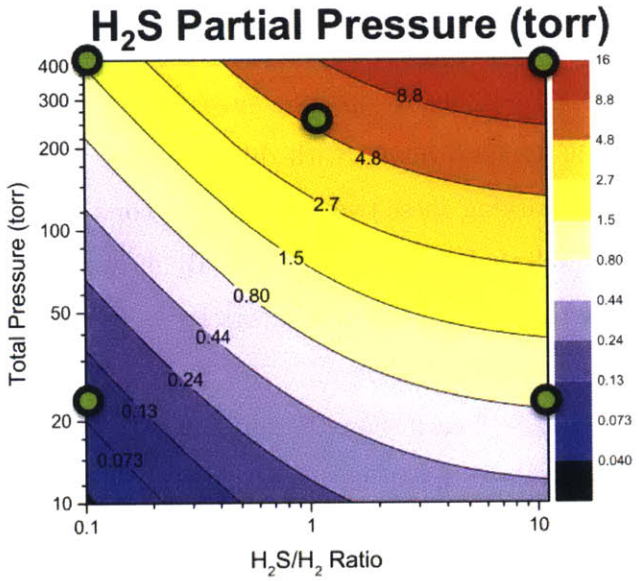

Figure 5-14: H_2S partial pressure contour map for different furnace parameters (total pressure and H_2S/H_2 ratio). Green dots show locations of experimental data points.Each axis is an experimental "knob" or parameter that can be adjusted on the H_2S furnace.

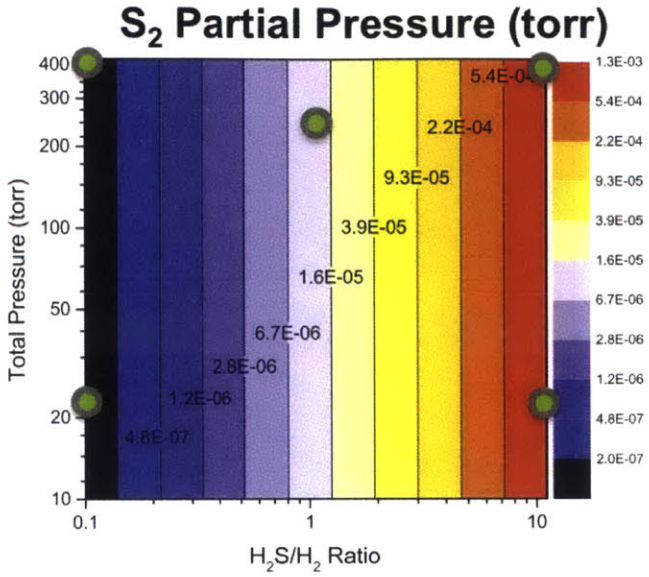

Figure 5-15: S_2 partial pressure contour map for different furnace parameters (total pressure and H_2S/H_2 ratio). Green dots show locations of experimental data points.Each axis is an experimental "knob" or parameter that can be adjusted on the H_2S furnace.

the effect of 2nd anneal temperature on majority carrier concentration.

Other samples will undergo an S_2 pressure sweep study. "Large grain" samples will be annealed at 450 °C for 6 hours, with different total pressures and different H_2S /H_2 flow ratios. By varying these two experimental conditions, we can explore a range of P_{S_2} values, as well as P_{H_2} and P_{H_2S} values. By measuring P_{S_2}, P_{H_2S} and P_{H_2} with the RGA, we can test to see if there is a correlation of any of these gases with carrier concentration or mobility changes.

Figures 5-13, 5-14, and 5-15 each show the range of partial pressures (for H_2, H_2S and S_2 respectively) available in the furnace, with current pressure sensors, valves and mass flow controllers. The y- and x- axis of each plot is an experimental variable (or "knob") that can be set on the furnace, while the contours are the scientific variable that will be changed for each anneal. The green dots show where experimental data points have been taken for the pressure sweep. Also notice that the S_2 partial pressure plot (Figure 5-15) is a series of vertical lines. This is because the sulfur partial pressure only changes with P_{H_2S}/P_{H_2}, not total pressure. The green dots on each figure have

been selected to create a wide range of P_{H_2}, P_{H_2S} and P_{S_2} values.

Methods

As-deposited films are still produced using "standard" conditions listed in Table 2.3. The depositions now occur solely on silicon wafers with a thermal oxide at least 500 nm thick. These wafers are diced and cleaned in acetone, ethanol, and IPA before deposition. Molybdenum is also coated on these Si/SiO_2 substrates, which serve as a platform to study grain morphology in films that can become SnS devices.

An example temperature vs. time and pressure vs. time schematic is shown in Figure 5-16. It is an example of the conditions a sample may experience during the two anneals.

The RGA is using conditions stated in Chapter 4.4. For the pressure sweep experiments, it was taking data continuously for each anneal, using the "semi-quantitative" calibration conditions.

Films that are annealed a 2nd time are again characterized by plan and profile view SEM, Hall and van der Pauw measurements.

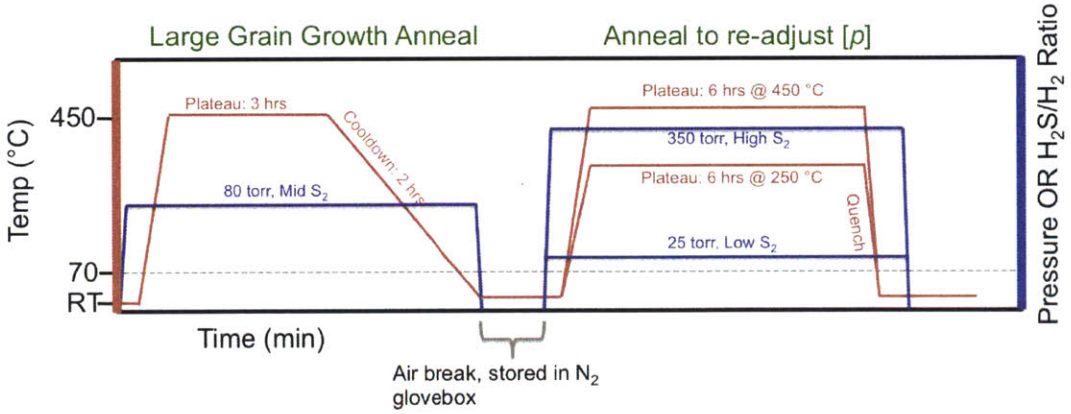

Figure 5-16: Schematic of experimental conditions for twice-annealed films. On the left, in red, is the temperature axis. On the right, in blue, is the Total Pressure or H_2S/H_2 ratio axis. Time is plotted on the x-axis, not to scale. The first anneal, or "Large Grain" anneal is plotted first, then an air break where samples are stored in N_2, then the 2nd anneal is plotted. Various options for 2nd anneal temperature and pressure are shown.

5.3.2 Results

"Large grain" film characterization

The results of "large grain" anneals are primarily seen in Chapter 5.2.1 in Figures 5-7 and 5-8. The 450 °C, 3 hour anneal is used (blue diamonds).

Temperature sweep

The effect of changing the 2nd anneal temperature from 250–450 °C is seen in Figure 5-17. Data are plotted against Albers *et al.* 1961 quenched crystal experiment for reference [5]. Based on the data collected, there appears to be little effect of 2nd anneal temperature on the final carrier concentration of the films. The comparison to Albers' data is slightly misleading. It cannot be determined if the annealing conditions used for Albers' experiments are completely appropriate for this comparison to thin films. However, it is one of the only other experiments to use quench-cooling to trap the carrier concentration of the SnS material in a high-temperature state.

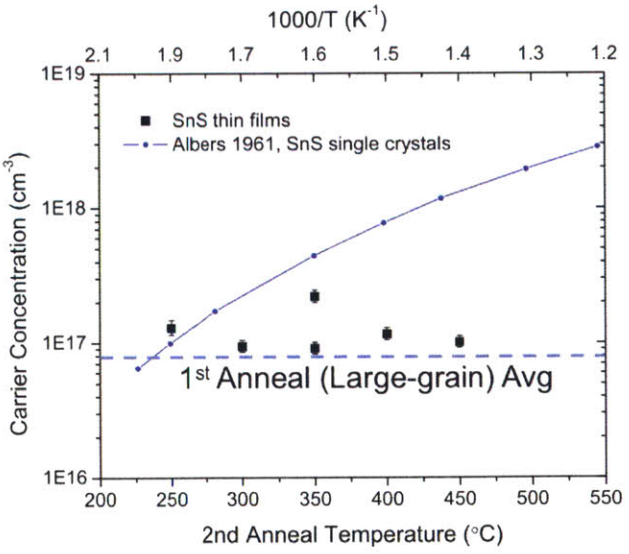

Figure 5-17: Carrier concentration vs. temperature of 2nd anneal. Black squares show data from this thesis, while blue line shows digitized data from Albers *et al.* 1961 paper, plotting the carrier concentration of quenched single crystals [5]. Error bars calculated from error due to thickness estimation (worst case: ± 100 nm). Blue dashed line is the average carrier concentration after the 1st "large grain" anneal.

Figure 5-18 plots mobility for samples held in the 2nd anneal stage for 360 minutes. The majority carrier mobility changes due to the temperature of the 2nd anneal. The mobility appears to decease with increasing 2nd anneal temperature. It is postulated that this is due to cracks likely induced by the rapid cooling quench step. These cracks are visible in both films on SiO_2 and Mo. It is also possible the decrease in mobility is due the effect of an unforeseen intrinsic defect.

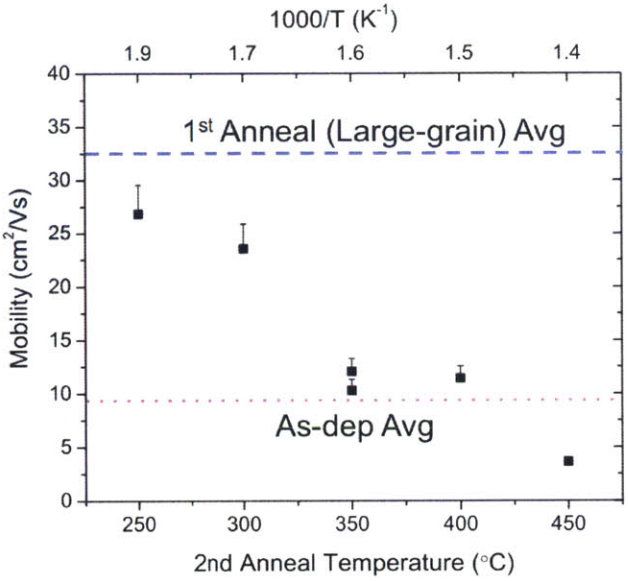

Figure 5-18: Mobility vs. temperature of 2nd anneal. Majority carrier mobility of thin films is observed to decrease with increasing 2nd anneal temperature. It is theorized this is due to cracking in the film as a result of the quench step. Average mobility is also shown for the as-deposited films and after the 1st "large grain" anneal.

SEM images on SiO_2 (Figure 5-19) show relatively little change in grain morphology after the 2nd anneal step.

Sulfur partial pressure (P_{S_2}) sweep

Sulfur conditions as measured by "semi-quantitative" RGA calibration

During the 2nd anneal step, we examine the extent of P_{S_2} space that the experimental conditions shown in Figures 5-13, 5-14, 5-15 were able to access. The P_{S_2} (measured by RGA and expected from equilibrium calculations) and temperature conditions are overlaid on the T vs. P_{S_2} phase diagram calculated in FactSage (Fig-

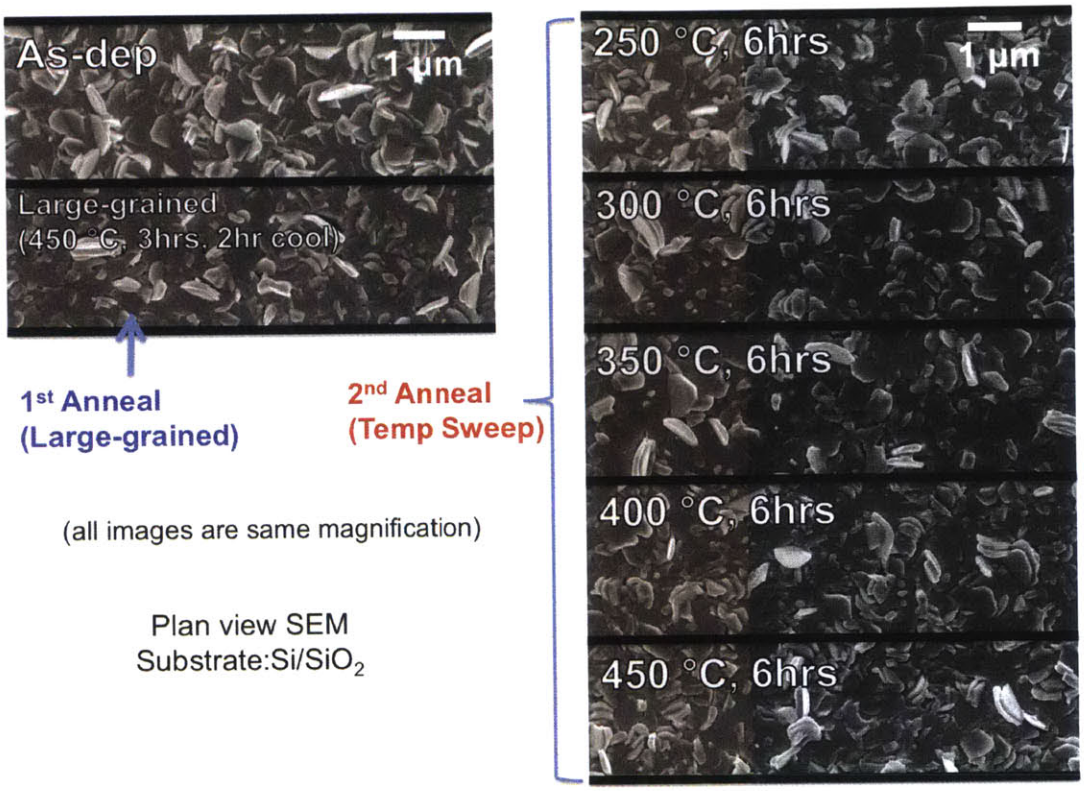

Figure 5-19: Temperature of 2nd Anneal Results: SEM images on SiO_2. The 2nd anneal appears to have little impact on grain morphology of SnS thin films grown on SiO_2.

ure 3-6). While the expected (equilibrium) S_2 conditions had a range of 6 orders of magnitude, the measured S_2 conditions had a much smaller range of 2 orders of magnitude. This apparent "compressing" of the experimental range is likely due to slow H_2S decomposition kinetics. Research into H_2S pyrolysis (or decomposition) show that the reaction does not proceed forward at fast rates until temperatures above 700 °C [36]. Thus production of S_2 is kinetically limited.

Figure 5-20 also suggests the experimental conditions may be in the Sn_2S_3 and SnS_2 forming regions. This possibility cannot be ruled out at the moment, but XRD scans currently indicate no other minority phases. However, XRD would not detect very small or nano-scale inclusions of sulfur-rich phases. Although great effort has been taken to obtain a reliable calibration for S_2 gas, it is still possible the measurement of S_2 is offset by some constant value.

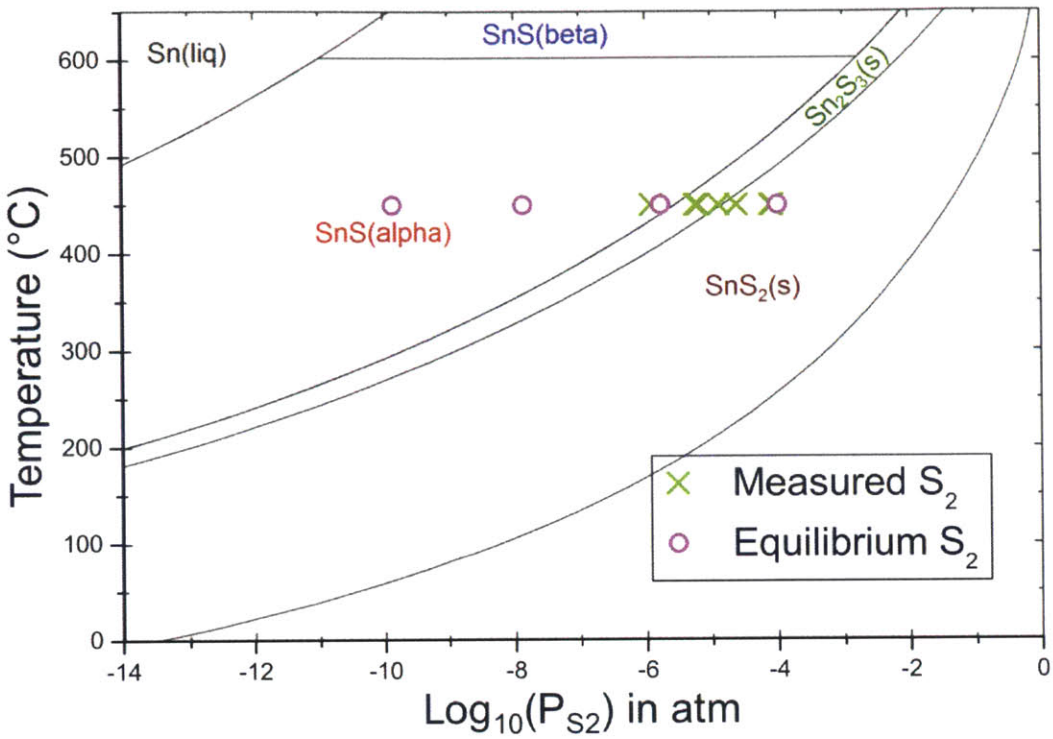

Figure 5-20: Measured and expected/equilibrium levels of P_{S_2} plotted on the SnS phase diagram. Expected/equilibrium conditions (magenta circles) for each data point come from the total pressure and H_2S/H_2 ratio in the furnace and the annealing temperature. Measured S_2 data (green crosses) are from a "semi-quantitative" calibration of the RGA, which samples gas at the end of the furnace tube.

Film Properties

Carrier concentration and mobility values for the pressure sweep annealing conditions have been plotted along three axes: P_{H_2}, P_{H_2S} and P_{S_2}, which have all been measured by the RGA during the 2nd anneal step. The colorbar legend indicates the total pressure of each anneal. Data points are also labeled with their primary anneal characteristics. Each 2nd step anneal was for 6 hours at 450 °C.

Figures 5-21 and 5-22 appear to show a flat-line trend of carrier concentration with partial pressure of any gas. Two repeated data points of "Low P, High S_2" appear to be outliers and do not fit well with the flat-line trend.

Figures 5-23 and 5-24 suggest a possible trend of increasing mobility with increasing P_{S_2} or P_{H_2S}. However, this trend is weak and may also be influenced by the

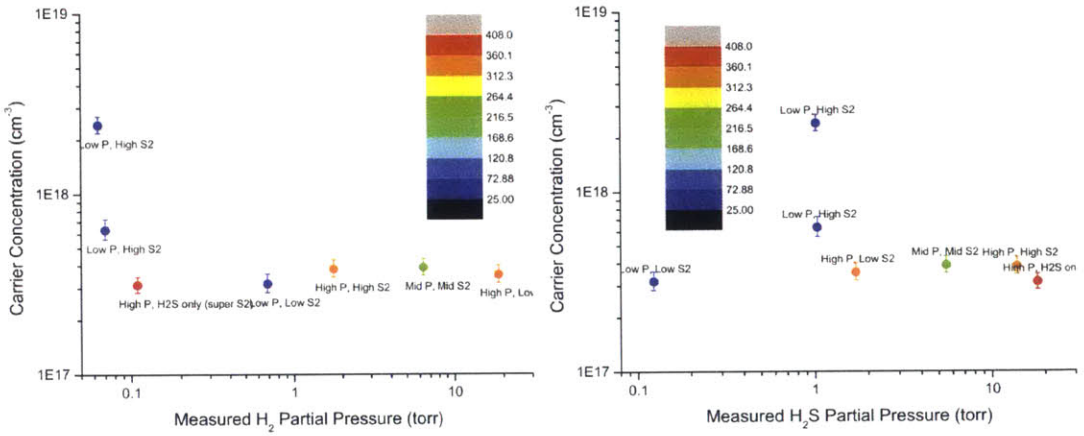

Figure 5-21: Carrier concentration vs. P_{H_2} gas or P_{H_2S} gas after pressure sweep 2nd anneal

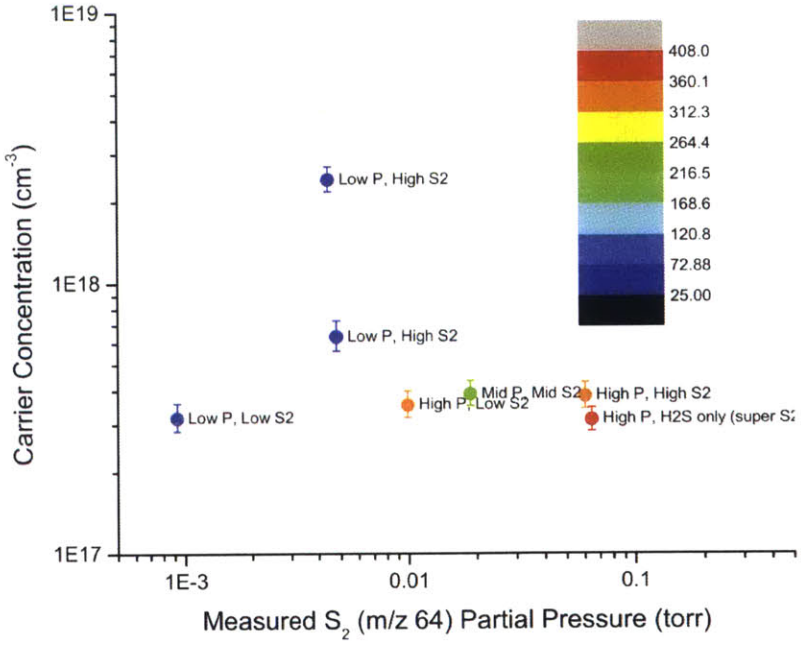

Figure 5-22: Carrier concentration vs. P_{S_2} gas after pressure sweep 2nd anneal

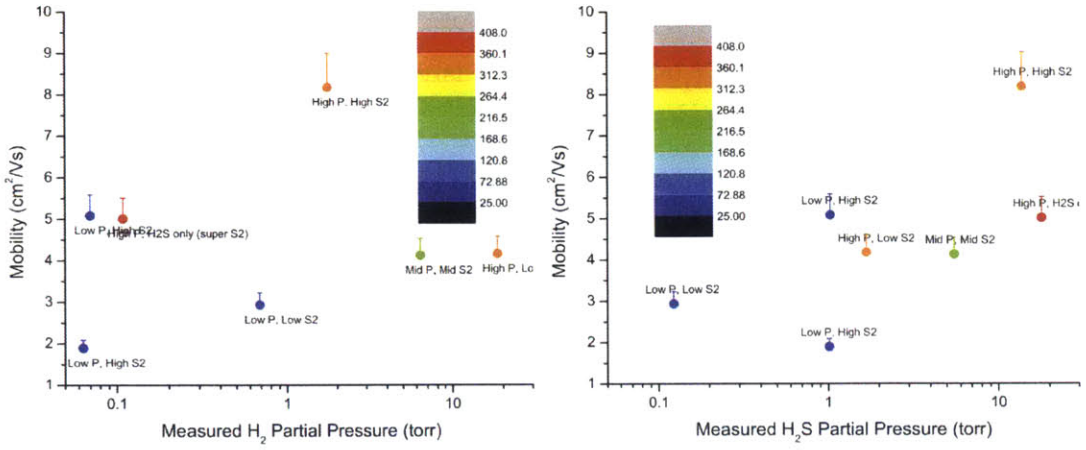

Figure 5-23: Mobility vs. P_{H_2} gas or P_{H_2S} gas after pressure sweep 2nd anneal

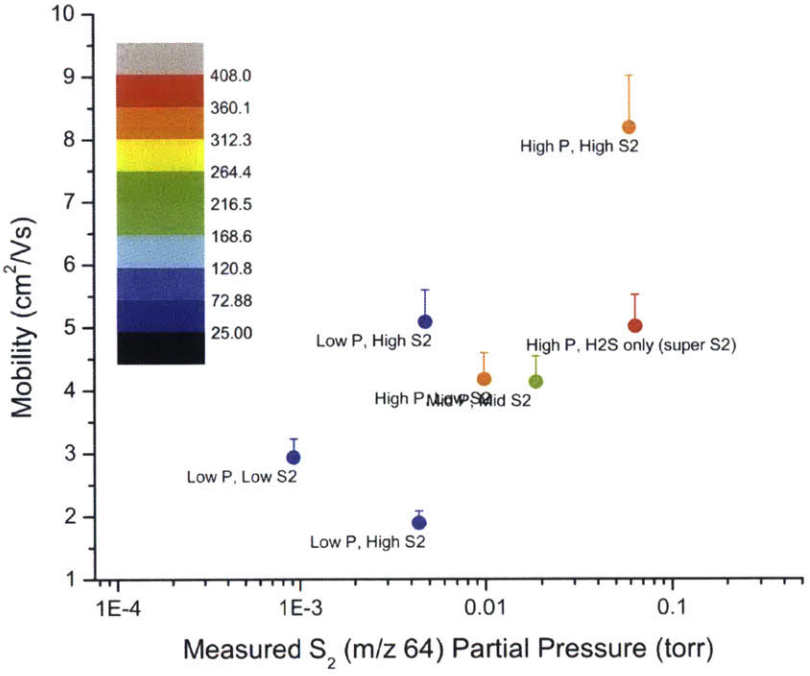

Figure 5-24: Mobility vs. P_{S_2} gas after pressure sweep 2nd anneal

fracturing of the SnS film upon quenching. There does not appear to be a trend of mobility changing with P_{H_2}.

SEM plan view images of the annealed films on Mo and on SiO_2 are shown below in Figures 5-25 and 5-26. Most interesting is the large grain size of the "High P, H_2S" only anneal (lower right). All of the annealed films show increased grain size on Mo, even after the 1st "large grain" anneal. Also of note is the "rippled" texture on the surface of some grains, especially at "Low P, Low S_2" condition. There are also a few holes/divots visible in the "Low P, High S_2" condition.

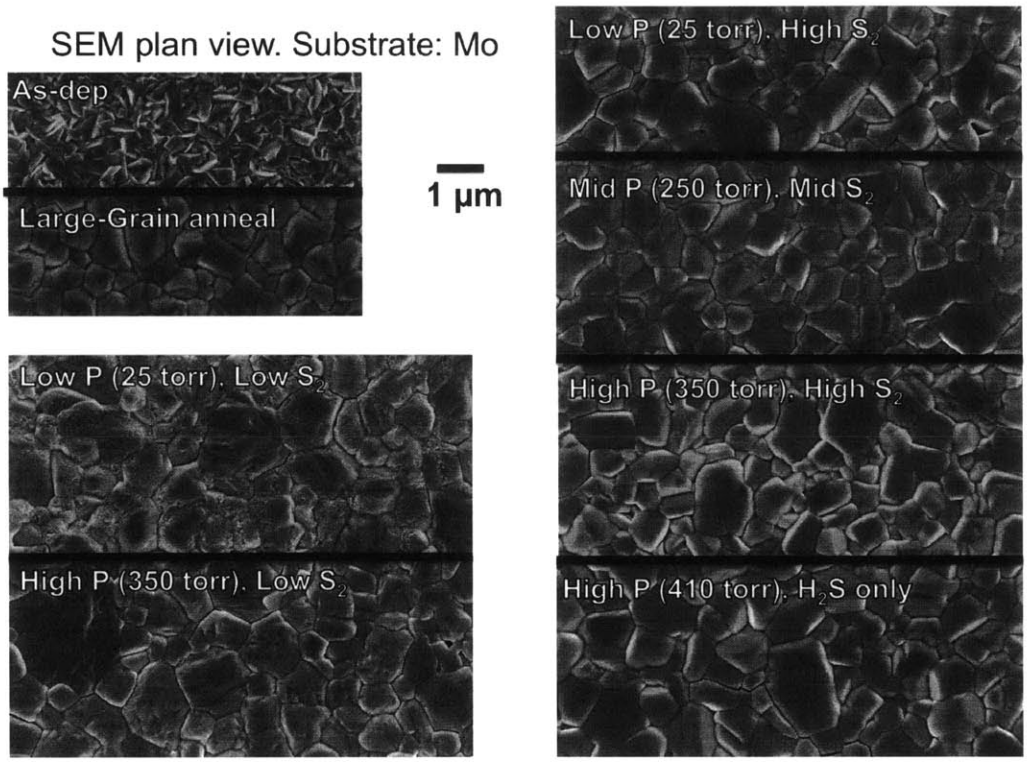

Figure 5-25: SEM plan-view after 2nd anneal pressure sweep, on Mo

A grain size analysis was performed on the twice-annealed films on Mo. Grain boundaries were traced and their areas computed. The results are displayed in Figure 5-27. Compared to Figure 5-4, the x-axis is 5× larger and shows significant grain growth for the "large grain" anneal and subsequent anneals. A strong pattern correlated to pressure or S_2 content is not observed, but the highest pressure, H_2S only anneal is observed to have the largest grain growth (shown in blue).

In the SEM images on SiO_2, it becomes more apparent that material is lost from the film during annealing under certain conditions. The "Low P, Low S_2" condition

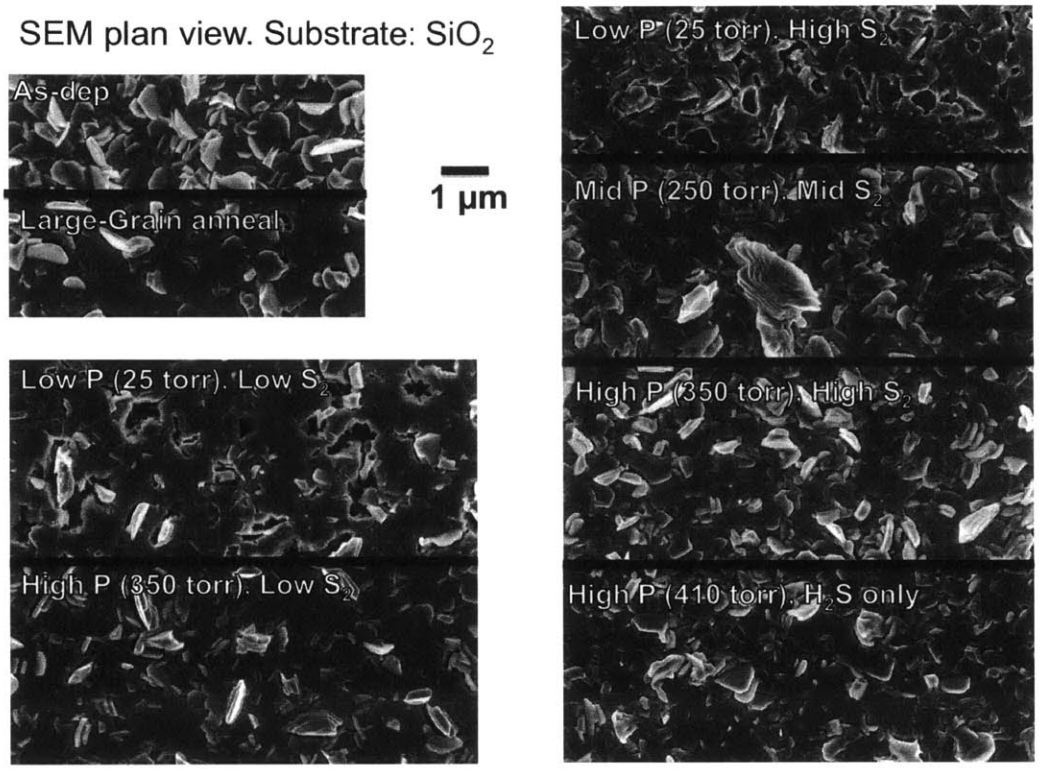

Figure 5-26: SEM plan-view after 2nd anneal pressure sweep, on SiO_2

shows significant porosity with numerous holes and divots. "Low P, High S_2" has a similar appearance. Even the "High P, Low S_2" annealing condition shows divots. The hypothesis of mass loss during these specific anneal conditions is also supported by observed deposition of material on the inside of the furnace walls, just outside the hot zone. After the 2nd anneal, the apparent grain size and morphology appears less altered for SnS films on SiO_2 than films on Mo.

XRD analysis (not shown) of the most sulfur rich condition ("High P, H_2S Only") showed that both the film on SiO_2 and on Mo remained phase pure SnS. Again the (040) peak on SiO_2 grew in strength, while the (111) peak for films on Mo grew slightly after annealing.

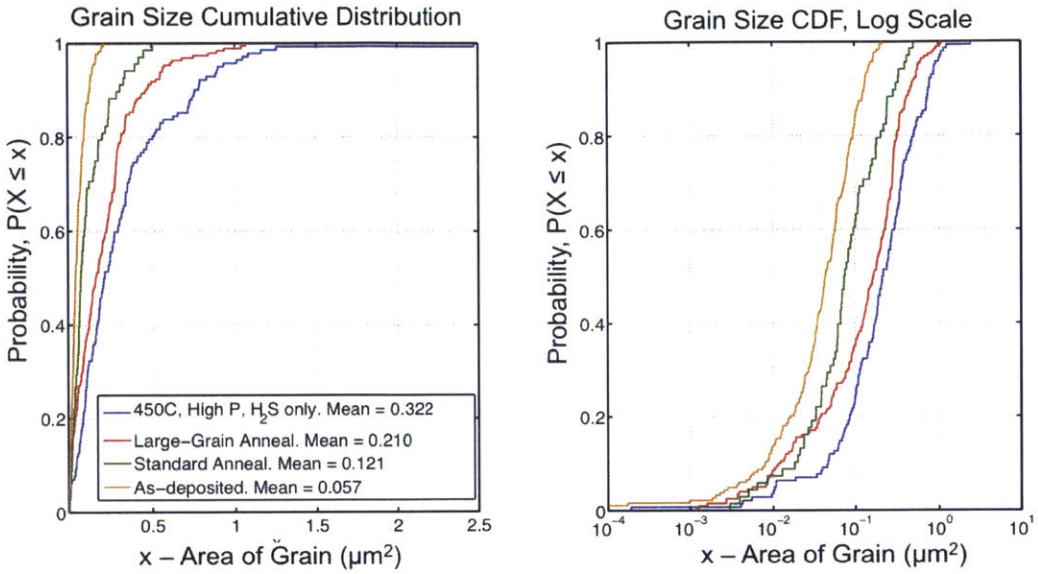

Figure 5-27: (Left) Grain size cumulative distribution function after 2nd pressure sweep anneals. (Right) Same data, but using a log-scale on the x-axis. As-deposited (yellow) and "Standard" (green) anneal conditions are plotted for reference. The "large grain" anneal (red) shows significant grain growth. After a 2nd anneal at 450 °C in "High P, H_2S only" conditions, the film on Mo shows even larger grain growth (blue). Mean grain area (in μm^2) is shown on the legend.

5.3.3 Device results

Annealing to create "large grain" material has also led to new promising solar cell results. Previously a "standard" anneal has been employed, which brings the the as-deposited SnS cells to a higher efficiency for both ALD-deposited SnS solar cells [88] and thermally evaporated solar cells. A thermally evaporated cell using the "standard" anneal was measured at NREL and found to have an efficiency of 3.88 % (Figure 5-28) [90]. In Table 5.2, the two annealing conditions used in the "standard" anneal and the new "large grain" anneal are compared. Both samples use a 1 μm SnS layer with a 14:1 N-doped ZnO_xS_y buffer layer. They were processed together for buffer layer deposition, ITO and Ag metallization.

JV measurements were taken using a Newport Oriel AAA-rated solar simulator, assuming a 0.25 mm^2 area. A light aperture was applied over each cell, to ensure an accurate area estimation and to avoid carrier collection from outside the cell area

and ITO pad. Light intensity was calibrated using a silicon calibration cell. Comparisons between devices measured on the same instrument are believed to be accurate. However, only NREL-certified efficiency results are shown.

Parameter	Standard	Large grain
Temperature (°C)	400	450
Ramp Time (min)	10	10
Plateau Time (min)	60	180
Cooling Profile	natural (~30 min)	linear (~120 min)
Gas Content	4 % H_2S at 100 sccm	4 % H_2S at 50 sccm + 4 % H_2 at 50 sccm
Total Pressure (torr)	28	80

Table 5.2: Comparison of SnS "standard" anneal and "large grain" anneal parameters. These two annealing conditions are used to make devices.

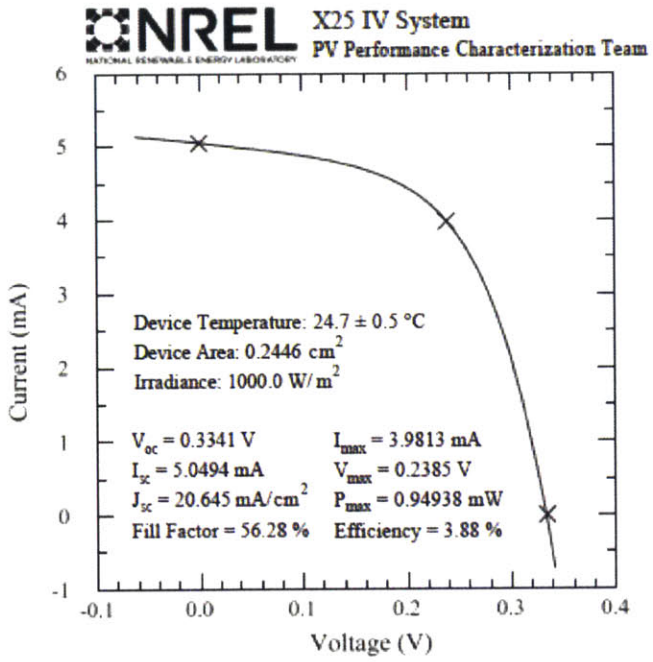

Figure 5-28: NREL-certified thermally evaporated SnS solar cell using "standard" thermal evaporation conditions and "standard" anneal conditions. Image from [90].

A JV comparison of the best cell for each annealing treatment is presented in Figure 5-29 (as-deposited,"standard," and "large grain"). For reference, the 1.3 % device from Reddy *et al.* 2006 is also plotted [70]. A comparison of median-value

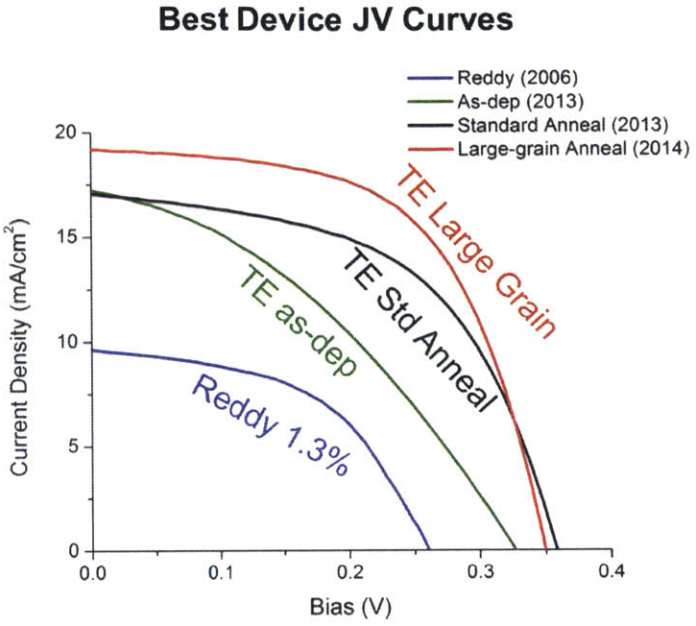

Figure 5-29: The best device for 3 different thermally evaporated SnS cell conditions are plotted and compared to the 1.3 % result from Reddy *et al.* 2006 [70]. The "large grain" anneal is observed to have the best efficiency results to date.

device parameters and associated thin film properties is also included in Table 5.3. Because there is some spread in the device results, a histogram is used to better visualize the data, rather than relying only on a median value. Histograms of V_{OC}, J_{SC} and FF are plotted for "standard" and "large grain" anneals (Figure 5-30). Comparing the 2 populations of devices: V_{OC} does not appear to change between the two annealing conditions, while J_{SC} and FF both show improvement after the "large grain" anneal.

Internal quantum efficiency (IQE) results for a well-performing device are plotted in Figure 5-31. EQE (external quantum efficiency) is measured on a PV Measurements QEX7 tool and reflectivity for each sample is measured on a Perkin Elmer Lambda 950 UV-Vis-NIR spectrophotometer. EQE measurements are recorded while the sample is in a dark box, with only the QE lamp as a light source. This is referred to as a "dark QE." Samples are measured with 0 V electrical bias and no other light bias.

Device parameter (median value)	Reddy, CdS (2006)	TE as-dep (2013)*	TE Standard anneal (2013)	TE Large grain anneal (2014)
$\Delta\ \eta$ (relative %)	–	33.8	60.2	23.8
V_{OC} (mV)	260	291	340	328
J_{SC} (mA/cm^2)	9.6	17.1	16.2	18.8
FF (%)	53	40	50.7	55.8
R_{series}	23	7.53	1.84	1.53
R_{shunt}	–	81.9	258	296
Film property (avg.)	–	–	–	–
Grain area (μm^2)	(est.) 0.11	0.06	0.12	0.21
Resistivity (Ω-cm)	5	193	34.3	2.86
Majority carrier conc. (cm^{-3})	5.3×10^{14}	4.2×10^{15}	5.5×10^{15}	8.1×10^{16}
Mobility (cm^2/Vs)	128	9.2	34.0	32.7

Table 5.3: Summary of median device and average film parameters. Device parameters listed are median values for each film condition. # of as-deposited devices = 11, # of "standard" anneal devices = 17, # of "large grain" devices = 16. Film properties are reported as averages. Target thickness for the SnS layer in each cell was 1000 nm, while the SnS layer in the Reddy cell is reported to be 600 nm thick. $\Delta\ \eta$ (relative %) is calculated using the previous cell efficiency. *The as-deposited cell sample was made approximately 1 year ago and stored in air. It was re-measured for this table. High series resistance is likely due to corroded Ag fingers.

Examining the two IQE curves, the "large grain" device shows clear improvement over almost the entire spectrum. In particular, there is improved IQE response in the long-wavelength range (~800–1000 nm). This is suggestive of an increased minority carrier collection length.

5.4 Discussion

5.4.1 Contributions to device improvement

Reflecting back to the motivations for annealing SnS films in Chapter 3, it is evident that annealing has produced positive improvements for SnS solar cells.

Contributions of increased grain size, increased mobility and increased carrier collection at high pressure and high H_2S content anneals have improved device per-

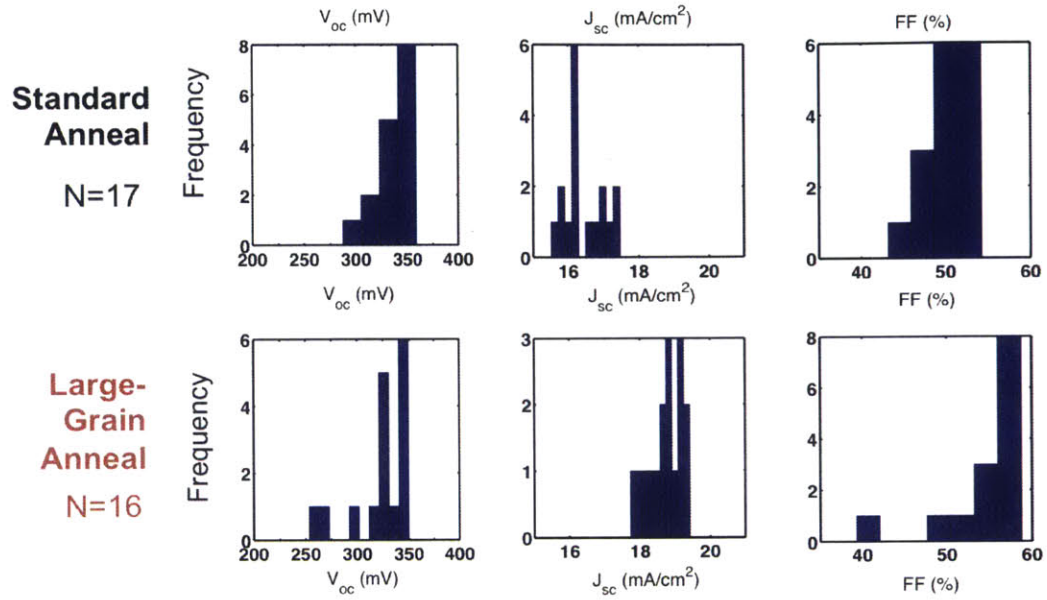

Figure 5-30: Histogram of device parameters for "standard" and "large grain" anneal conditions. Little change is observed for V_{OC}, but both J_{SC} and FF are observed to improve after the "large grain" annealing treatment.

formance by 98.4 % relative, compared to as-deposited devices. The larger grain size likely reduces carrier recombination, while increased mobility can also reduce recombination and increase carrier collection.

Both of the annealing conditions showed an increase in V_{OC} as compared to the as-deposited devices. V_{OC} can be improved through reduced dark current (Equation 3.1). Alternatively, an increase in $[p]$ also directly increases open-circuit voltage (Equation 3.2). However, as discussed in Stevanović *et al.*, SnS experiences large changes in conduction band minimum, depending on the surface orientation [91]. This has strong consequences for V_{OC} and makes interpreting changes in V_{OC} very difficult because the orientation of SnS grains changes from as-deposited to "standard" to "large grain" anneal.

Improvements in J_{SC} are easily seen between the "standard" anneal and "large grain" anneal. J_{SC} is heavily influenced by the carrier collection length (depletion region + diffusion length). Based on the IQE data in Figure 5-31, the evidence for improved collection is strong. Additionally, the majority carrier concentration increases

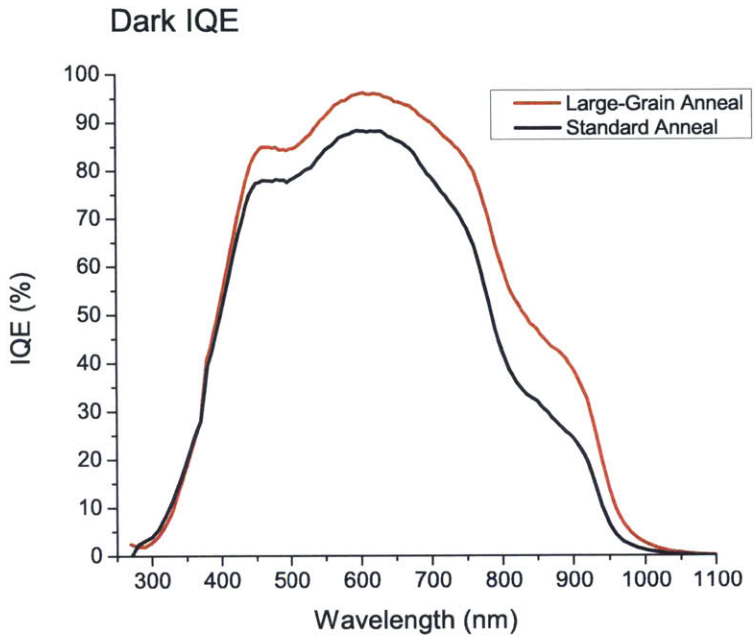

Figure 5-31: IQE (internal quantum efficiency) for a "standard" anneal device (black) and a "large grain" anneal (red), measured under dark conditions with no electrical or light bias.

sharply between the "standard" and "large grain" anneals. When the majority carrier concentration increases in the SnS layer, the depletion region is expected to shrink. This would have the effect of decreasing total collection length, assuming the diffusion length stays the same. However, the efficiency improved for the "large grain" anneal and it is hypothesized that the minority carrier diffusion length would have to increase *more* than the shrinking of the depletion region, in order to see improved efficiency. Further modeling of the IQE curve and of the device itself (such as in SCAPS) is necessary to determine if this hypothesis can explain J_{SC} and η improvement.

Series resistance, shunt resistance and fill factor are all improved significantly with the "large grain" anneal. It is suspected the increase in shunt resistance is due to grain coalescence and fewer pinholes, but this has not been proven. Lock-in thermography would be a good method to test this hypothesis. It is difficult to pinpoint the cause in reduced series resistance, but lower absorber layer resistivity is a possibility. Fill factor also improved from as-deposited to "standard" to "large grain" anneal. The

sharpest increase is between as-deposited to "standard" anneal, suggesting the change in morphology from as-deposited to annealed may play a role.

5.4.2 Practical boundaries of annealing for improved grain morphology

The anneal that created the highest performing device was intentionally optimized for large grain size, but also selected for its promising morphology on Mo. The other films in the pressure sweep anneal set (Chapter 5.2.1) experience material evaporation instead. This loss of material is likely detrimental to solar cell performance, creating holes and voids for easy shunt paths and reducing the amount of material that can absorb photons. This loss of material may also reduce carrier mobility.

Based on these observations, an upper bound can be drawn for the annealing temperature and time. If one is annealing for large grain growth, one should not go above 500 °C for 1 hour with a pressure of 80 torr at Mid S_2 conditions. To exceed these time or temperature limits, one may have to raise the total pressure or S_2 content of the gas. One could also exceed this time limit by lowering the temperature or raising the total pressure.

Using the SEM images in Figures 5-25 and 5-26 we can also draw a lower bound in annealing parameter space for total pressure and S_2 gas content. For films annealed at 450 °C for 6 hours, pressures should not go below 25 torr or a "Low S_2" content. Even the "Low P, High S_2" content annealing condition was not enough to prevent material loss. This suggests that total pressure is a strong lever for preventing or allowing evaporation of material. In general, annealing at higher pressures will likely reduce film evaporation and mass loss. The benefits of high total pressure are seen in the "High P, H_2S only" condition. This anneal had the highest total pressure and also exhibits the largest grains.

5.4.3 Carrier concentration and thermal history

The majority carrier concentration of SnS films can be manipulated by two orders of magnitude. To create inversion at a *p*-*n* junction the majority carrier concentration in SnS should be selected based on a known buffer layer *n*-type carrier concentration. These annealing results provide a starting recipe to be able to attain the desired carrier concentration. Additionally, several of these annealing conditions provide a high mobility film. Due to the curvature of the conduction band minimum, electrons are predicted to have lower effective mass than holes. This suggests that electron mobilities could be even higher than the measured hole mobilities. If this is the case, SnS films would have excellent minority carrier mobilities compared to some of its competitors such as CIGS (1-20 cm^2/Vs [47, 102]) and CZTS.

Thermal history of the sample also seems to be an important factor in the ability to change carrier concentration. We observe that as-deposited films can change their carrier concentration by 1 or 2 orders of magnitude. Even within the first 6 minutes of a 250 °C anneal, a significant change in carrier concentration is observed (Figure 5-7). However, after the 1st anneal, the carrier concentration seems more difficult to adjust. Both annealing temperature and P_{S_2} appear to have little effect on the carrier concentration. Assuming these films reached equilibrium during the 6 hour anneal, these films do not behave as we might expect according to Kröger-Vink theory or DFT calculations. There is likely another phenomenon acting upon the samples to produce these results.

When compared to the Albers *et al.* 1961 results on single crystals (Figure 5-17), the carrier concentration in SnS thin films did not change with temperature, while $[p]$ in single crystals did change. There are several possible explanations, none of which currently has enough supporting evidence. It is possible that the diffusivity is too low in thin films, thereby preventing a change in stoichiometry (or V''_{Sn} concentration) or low diffusivity could also prevent the re-association of V''_{Sn} to the $(V_{Sn}V_{Sn})^{\times}$ neutral defect (as shown in Equations 1.3 and1.4).

Generally, the the observed changes in thin film SnS after annealing are not well

explained by the Kröger-Vink or DFT models. More research, particularly into kinetic limitations is needed to better explain the current results.

In the process of teasing out these conclusions, a great deal has been learned about the annealing of SnS. Annealing parameters have been found that lead to more efficient SnS devices. These parameters may also permit a thinner SnS device. Currently the SnS layer is 1 μm thick, but improved annealing may allow a 500 nm or thinner layer, while still preventing pinholes and shunts. This would benefit the cell efficiency by improving V_{OC} because of reduced leakage current.

This thesis presents a useful tool and framework for understanding and controlling the intrinsic point defect population in SnS. Subsequent students can use this tool and framework for research questions that further elucidate the behavior of SnS intrinsic point defects.

Chapter 6

Conclusion

At the start of this project in 2008, SnS had an efficiency of 1.3%. Now, because of research into the annealing of SnS in H_2S, the record has nearly tripled for thermally evaporated SnS devices. Majority carrier concentration can be controlled over 2 orders of magnitude and grains over 2 μm in diameter can be achieved. Bounds on the useful parameter space for annealing SnS have been delineated. Within these bounds there is promise for improved device efficiencies. Also important is the realization that thermal history of the sample influences majority carrier concentration. Both thermodynamic models of Kröger-Vink/Rau and DFT defect calculations are not able to predict the currently observed behavior during annealing. This points towards kinetic factors that influence the carrier concentration.

The construction of the H_2S furnace and the learnings garnered in this thesis will act as a platform for further research into tin sulfide intrinsic defects. At some point in the near future, we might be able to say why SnS will or will not make a great solar cell material.

To be able to examine a material, its properties, and then predict its performance in a particular function is part of a much broader goal of material science as a field. We can figure out how to do this more accurately by creating case studies, such as that of SnS and its application in PV materials. In the process of studying SnS as a solar cell material, we are better able to refine our list of ideal solar cell material properties. The list of necessary characteristics for a solar cell material, as stated in

Chapter 1, does not look the same today. By continuing to study SnS with the tools and framework established in this thesis, we continue to learn about SnS and what defines the ideal solar cell material.

Bibliography

[1] 3.1.3 Abundances of the elements. In *Kaye and Laby Tables of Physical & Chemical Constants Online. Version 1.0.* National Physical Laboratory, 2005.

[2] U.S. Energy Information Administration. Annual Energy Outlook 2011. `www.eia.gov/forecasts/aeo/`. [Online; accessed April 2011].

[3] W Albers, C Haas, H Ober, G R Schroder, and J D Wasscher. Preparation and properties of mixed crystals $SnS_{(1-x)}Se_x$. *Journal of Physics and Chemistry of Solids*, 23:215–220, 1962.

[4] W Albers, C Haas, and F van der Maesen. The preparation and the optical properties of electrical and SnS crystals. *Journal of Physics and Chemistry of Solids*, 15:306–310, 1960.

[5] W Albers, C Haas, H J Vink, and J D Wasscher. Investigations on SnS. *Journal of Applied Physics*, 32(10):2220, 1961.

[6] W Albers and K Schol. The P-T-X phase diagram of the system Sn-S. *Philips Research Reports*, 16:329–342, 1961.

[7] European Photovoltaic Industry Association. Global Market Outlook for Photovoltaics 2014-2018. `http://www.epia.org/fileadmin/user_upload/Publications/EPIA_Global_Market_Outlook_for_Photovoltaics_2014-2018_-_Medium_Res.pdf`. [Online; accessed 20 Oct 2014].

[8] D Avellaneda, G Delgado, M T S Nair, and P K Nair. Structural and chemical transformations in SnS thin films used in chemically deposited photovoltaic cells. *Thin Solid Films*, 515(15):5771–5776, 2007.

[9] R W Balluffi, S M Allen, and W C Carter. *Kinetics of Materials.* Wiley, 2005.

[10] R E Banai, L A Burton, S G Choi, F Hofherr, T Sorgenfrei, A Walsh, B To, A Cröll, and J R S Brownson. Ellipsometric characterization and density-functional theory analysis of anisotropic optical properties of single-crystal α-SnS. *Journal of Applied Physics*, 116:013511, 2014.

[11] R B Bergmann. Crystalline Si thin-film solar cells: A review. *Applied Physics A*, 69:187–194, 1999.

[12] P Campbell and M A Green. Light trapping properties of pyramidally textured surfaces. *Journal of Applied Physics*, 62:243–249, 1987.

[13] P Campbell and M A Green. High performance light trapping textures for monocrystalline silicon solar cells. *Solar Energy Materials and Solar Cells*, 65:369–375, 2001.

[14] J M Chamberlain and M Merdan. Infrared photoconductivity in *p*-SnS. *Journal of Physics C: Solid State Physics*, 10(19):L571, 1977.

[15] J M Chamberlain, P M Nikolic, M Merdan, and P Mihailovic. Far-infrared optical properties of SnS. *Journal of Physics C: Solid State Physics*, 9(22):L637, 1976.

[16] D J Cherniak. Diffusion in carbonates, fluorite, sulfide minerals, and diamond. *Reviews in Mineralogy and Geochemistry*, 72:871–897, 2010.

[17] Y Chiang, D P Birnie, and W D Kingery. *Physical Chemistry*. Wiley, 1997.

[18] C Cifuentes, M Botero, E Romero, and C Calderón. Optical and structural studies on SnS films grown by co-evaporation. *Brazilian Journal of Physics*, 36(3B):1046–1049, 2006.

[19] R Colin and J Drowart. Thermodynamic study of tin sulfide and lead sulfide using a mass spectrometer. *Journal Of Chemical Physics*, 37:1120, 1962.

[20] N P Dasgupta, J F Mack, M C Langston, A Bousetta, and F B Prinz. Design of an atomic layer deposition reactor for hydrogen sulfide compatibility. *Review of Scientific Instruments*, 81:044102, 2010.

[21] M Devika, K Reddy, N Reddy, K Ramesh, and R Ganesan. Microstructure dependent physical properties of evaporated tin sulfide films. *Journal of Applied Physics*, 100:023518, 2006.

[22] M Devika, N Reddy, K Ramesh, R Ganesan, K R Gunasekhar, E S R Gopal, and K T Ramakrishna Reddy. Thickness effect on the physical properties of evaporated SnS films. *Journal of the Electrochemical Society*, 154:H67–H73, 2007.

[23] K Emery and D Myers. ASTM G173-03 Reference Spectra. NREL, `http://rredc.nrel.gov/solar/spectra/am1.5/`. [Online; accessed July 2008].

[24] A R H F Ettema, R A deGroot, C Haas, and T S Turner. Electronic structure of SnS deduced from photoelectron spectra and band-structure calculations. *Physical Review B*, 46:7363–7373, 1992.

[25] A Feltrin and A Freundlich. Material challenges for terawatt level deployment of photovoltaics. *4th World Conference on Photovoltaic Energy Conversion*, pages 2469–2472, 2006.

[26] X Fontané, V Izquierdo-Roca, L Calvo-Barrio, A Pérez-Rodríguez, J R Morante, D Guettler, A Eicke, and A N Tiwari. Investigation of compositional inhomogeneities in complex polycrystalline Cu(In,Ga)Se_2 layers for solar cells. *Applied Physics Letters*, 95(26):261912, 2009.

[27] M Fox. *Optical Properties of Solids.* Oxford University Press, 2001.

[28] F M Gashimzade, D G Guliev, D A Guseinova, and VY Shteinshrayber. Band-structure calculation for A^4B^6 layered crystals by the equivalent-orbital linear combination of atomic orbitals method. *Journal of Physics Condensed Matter*, 4:1081–1091, 1992.

[29] M A Green. Limits on the open-circuit voltage and efficiency of silicon solar cells imposed by intrinsic Auger processes. *Electron Devices, IEEE Transactions on*, 31(5):671–678, 1984.

[30] W Guang-Pu, Z Zhi-Lin, Z Wei-Ming, G Xiang-Hong, C Wei-Qun, H Tanamura, M Yamaguchi, H Noguchi, T Nagatomo, and O Omoto. Investigation on SnS film by RF sputtering for photovoltaic application. *IEEE First World Conference on Photovoltaic Energy Conversion, Dec 5-9, 1994. Hawaii. / Conference Record of the 24th IEEE Photovoltaic Specialists Conference*, pages 365–368, 1994.

[31] C Haas and M M G Corbey. Measurement and analysis of the infrared reflection spectrum of semiconducting SnS. *Journal of Physics and Chemistry of Solids*, 20:197–203, 1961.

[32] K Hartman, M Bertoni, J Serdy, and T Buonassisi. Dislocation density reduction in multicrystalline silicon solar cell material by high temperature annealing. *Applied Physics Letters*, 93:122108, 2008.

[33] K Hartman, J L Johnson, M I Bertoni, D Recht, M J Aziz, M A Scarpulla, and T Buonassisi. SnS thin-films by RF sputtering at room temperature. *Thin Solid Films*, 519:7421–7424, 2011.

[34] K A Hawboldt, W D Monnery, and W Y Svrcek. New experimental data and kinetic rate expression for H_2S pyrolysis and re-association. *Chemical engineering science*, 55:957–966, 2000.

[35] S S Hegedus and W N Shafarman. Thin-film solar cells: Device measurements and analysis. *Progress in Photovoltaics Research and Applications*, 12:155–176, 2004.

[36] V E Kaloidas and N G Papayannakos. Hydrogen production from the decomposition of hydrogen sulphide. Equilibrium studies on the system $H_2S/H_2/S_i$,(i=1,..., 8) in the gas phase. *International Journal of Hydrogen Energy*, 12:403–409, 1987.

[37] D W Koon. Effect of contact size and placement, and of resistive inhomogeneities on van der Pauw measurements. *Review of Scientific Instruments*, 60:271, 1989.

[38] N Koteswara Reddy and K T Ramakrishna Reddy. Tin sulphide films for solar cell application. *IEEE 26th Photovoltaics Specialists Conference, Sept 30 - Oct 3*, pages 515–518, 1997.

[39] F A Kröger and H J Vink. Relations between the concentrations of imperfections in solids. *Journal of Physics and Chemistry of Solids*, 5:208–223, 1958.

[40] A P Lambros, D Geraleas, and N A Economou. Optical absorption edge in SnS. *Journal of Physics and Chemistry of Solids*, 35:537–541, 1974.

[41] S Lany, K Biswas, J Vidal, and A Zunger. Theory of bandstructure and defect properties in compound semiconductors for energy applications. In *Materials Research Society Spring 2011 Conference*, San Francisco, CA, June 2011. [Presentation, Session D3.1].

[42] B Leffler. *Stainless-stainless steels and their properties.* Scribd, 2013.

[43] E A Lund and M A Scarpulla. Photovoltaic heterojunctions of inorganic semiconductors in the defective limit. *Materials Science and Engineering B*, 177(16):1436–1440, 2012.

[44] L Makinistian and E A Albanesi. On the band gap location and core spectra of orthorhombic IV-VI compounds SnS and SnSe. *physica status solidi (b)*, 246:183–191, 2009.

[45] B D Malone, A Gali, and E Kaxiras. First principles study of point defects in SnS. *Physical Chemistry Chemical Physics*, 16:26176–26183, 2014.

[46] B D Malone and E Kaxiras. Quasiparticle band structures and interface physics of SnS and GeS. *Physical Review B*, 87:245312, 2013.

[47] J Mattheis and J H Werner. Finite mobility effects on the radiative efficiency limit of pn-junction solar cells. *Physical Review B*, 77(8):1–13, 2008.

[48] R W Miles, O E Ogah, G Zoppi, and I Forbes. Thermally evaporated thin films of SnS for application in solar cell devices. *Thin Solid Films*, 517(17):4702–4705, 2009.

[49] D B Mitzi, O Gunawan, T K Todorov, K Wang, and S Guha. The path towards a high-performance solution-processed kesterite solar cell. *Solar Energy Materials and Solar Cells*, 95(6):1421–1436, 2011.

[50] A Nagoya, R Asahi, R Wahl, and G Kresse. Defect formation and phase stability of Cu_2ZnSnS_4 photovoltaic material. *Physical Review B*, 81(11):113202, 2010.

[51] B B Nariya, A K Dasadia, M K Bhayani, A J Patel, and A R Jani. Growth and transport properties of tin monosulphide and tin monoselenide single crystals. *Chalcogenide Letters*, 6:549–554, 2009.

[52] M M Nassary. Temperature dependence of the electrical conductivity, Hall effect and thermoelectric power of SnS single crystals. *Journal of Alloys and Compounds*, 398:21–25, 2005.

[53] A Niemegeers, M Burgelman, and A De Vos. On the CdS/$CuInSe_2$ conduction band discontinuity. *Applied Physics Letters*, 67:843, 1995.

[54] H Noguchi, A Setiyadi, H Tanamura, T Nagatomo, and O Omoto. Characterization of vacuum-evaporated tin sulfide film for solar cell materials. *Solar Energy Materials and Solar Cells*, 35:325–331, 1994.

[55] H Nozaki, M Onoda, M Sekita, K Kosuda, and T Wada. Variation of lattice dimensions in epitaxial SnS films on MgO (001). *Journal Of Solid State Chemistry*, 78:245–252, 2005.

[56] P A Nwofe, K T Ramakrishna Reddy, K Tan, I Forbes, M Leach, D Y Jang, and R W Miles. Investigating the potential of SnS for use in photovoltaic solar cell applications. In *PVSAT-8: 8th Photovoltaic Science, Applications and Technology Conference. 2-4 April 2012*, pages 89–92, Newcastle upon Tyne, UK, 2012.

[57] O E Ogah, K R Reddy, G Zoppi, I Forbes, and R W Miles. Annealing studies and electrical properties of SnS-based solar cells. *Thin Solid Films*, 519(21):7425–7428, 2011.

[58] J I Pankove. *Optical Processes in Semiconductors*. Prentice-Hall, 1971.

[59] M Parenteau and C Carlone. Influence of temperature and pressure on the electronic transitions in SnS and SnSe semiconductors. *Physical Review B*, 41:5227–5234, 1990.

[60] H H Park, R Heasley, and R G Gordon. Atomic layer deposition of Zn(O,S) thin films with tunable electrical properties by oxygen annealing. *Applied Physics Letters*, 102:132110, 2013.

[61] H H Park, R Heasley, L Sun, V Steinmann, R Jaramillo, K Hartman, R Chakraborty, P Sinsermsuksakul, D Chua, T Buonassisi, and R G Gordon. Co-optimization of SnS absorber and Zn(O,S) buffer materials for improved solar cells. *Progress in Photovoltaics: Research and Applications*, page n/a, May 2014. doi: 10.1002/pip.2504.

[62] Cole Parmer. Chemical Compatibility Database. `http://www.coleparmer.com/Chemical-Resistance`. [Online; accessed March 2012].

[63] D Peckner and I M Bernstein. *Handbook of Stainless Steels*. McGraw-Hill, 1977.

[64] C Persson, C Platzer-Björkman, J Malmström, T Törndahl, and M Edoff. Strong valence-band offset bowing of $ZnO_{1-x}S_x$ enhances p-type nitrogen doping of ZnO-like alloys. *Physical Review Letters*, 97:146403, 2006.

[65] V Piacente, S Foglia, and P Scardala. Sublimation study of the tin sulphides SnS_2 Sn_2S_3 and SnS. *Journal of Alloys and Compounds*, 177:17–30, 1991.

[66] P Pramanik, P K Basu, and S Biswas. Preparation and characterization of chemically deposited tin(II) sulphide thin films. *Thin Solid Films*, 150:269–276, 1987.

[67] L S Price, I P Parkin, T G Hibbert, and K C Molloy. Atmospheric pressure CVD of SnS and SnS_2 on glass. *Chemical Vapor Deposition*, 4(6):222–225, 1998.

[68] MDC Vacuum Products. Quick Disconnect. `http://www.mdcvacuum.com/displayproductcontent.aspx?d=MDC&p=m.1.8.7.1`. [Online; accessed June 2013].

[69] K T Ramakrishna Reddy, P Purandhara Reddy, P K Datta, and R W Miles. Formation of polycrystalline SnS layers by a two-step process. *Thin Solid Films*, 403:116–119, 2002.

[70] K T Ramakrishna Reddy, N Koteswara Reddy, and R Miles. Photovoltaic properties of SnS based solar cells. *Solar Energy Materials and Solar Cells*, 90(18-19):3041–3046, 2006.

[71] H Rau. High temperature equilibrium of atomic disorder in SnS. *Journal of Physics and Chemistry of Solids*, 27:761–769, 1966.

[72] S C Ray, M K Karanjai, and D DasGupta. Structure and photoconductive properties of dip-deposited SnS and SnS_2 thin films and their conversion to tin dioxide by annealing in air. *Thin Solid Films*, 350:72–78, 1999.

[73] G Rey, A Redinger, J Sendler, T P Weiss, M Thevenin, M Guennou, B El Adib, and S Siebentritt. The band gap of $Cu_2ZnSnSe_4$: Effect of order-disorder. *Applied Physics Letters*, 105:112106, 2014.

[74] A Richter, M Hermle, and S W Glunz. Reassessment of the limiting efficiency for crystalline silicon solar cells. *IEEE Journal of Photovoltaics*, 3(4):1184–1191.

[75] Marco Rubber. Marco Markez vs. DuPont Kalrez O-Ring Materials. `http://www.marcorubber.com/markez.htm`. [Online; accessed March 2012].

[76] N Sato, M Ichimura, E Arai, and Y Yamazaki. Characterization of electrical properties and photosensitivity of SnS thin films prepared by the electrochemical deposition method. *Solar Energy Materials and Solar Cells*, 85:153–165, 2005.

[77] J H Scofield, A Duda, D Albin, B L Ballard, and P K Predecki. Sputtered molybdenum bilayer back contact for copper indium diselenide-based polycrystalline thin-film solar cells. *Thin Solid Films*, 260:26–31, 1995.

[78] S Seyrling, A Chirila, D Güttler, P Blösch, F Pianezzi, R Verma, S Bücheler, S Nishiwaki, Y E Romanyuk, P Rossbach, and A N Tiwari. $CuIn_{1-x}Ga_xSe_2$ growth process modifications: Influences on microstructure, Na distribution, and device properties. *Solar Energy Materials and Solar Cells*, 95:1477–1481, 2011.

[79] R C Sharma and Y A Chang. The S-Sn (sulfur-tin) system. *Bulletin of Alloy Phase Diagrams*, 7:269–273, 1986.

[80] M Sharon and K Basavaswaran. Photoelectrochemical behaviour of tin monosulphide. *Solar Cells*, 25:97–107, 1988.

[81] K Shinichi and S Shigetoshi. Production of thin film of tin sulfide. Patent Abstracts of Japan. Publication Number: 08-176814. Application Number: 06-334572. Date Published: July 9, 1996.

[82] W Shockley and H J Queisser. Detailed balance limit of efficiency of *p-n* junction solar cells. *Journal of Applied Physics*, 32(3):510–519, 1961.

[83] S Siebentritt. What limits the efficiency of chalcopyrite solar cells? *Solar Energy Materials and Solar Cells*, pages 1–6, 2011.

[84] O P Singh and V P Gupta. Electronic properties of tin monochalcogenides (SnS, SnSe, SnTe). *physica status solidi (b)*, 136:K41–K44, 1986.

[85] P Sinsermsuksakul, R Chakraborty, S B Kim, S M Heald, T Buonassisi, and R G Gordon. Antimony-doped tin(II) sulfide thin films. *Chemistry of Materials*, 24(23):4556–4562, 2012.

[86] P Sinsermsuksakul, K Hartman, S B Kim, J Heo, L Sun, H H Park, R Chakraborty, T Buonassisi, and R G Gordon. Enhancing the efficiency of SnS solar cells via band-offset engineering with a zinc oxysulfide buffer layer. *Applied Physics Letters*, 102(5):053901, 2013.

[87] P Sinsermsuksakul, J Heo, W Noh, A S Hock, and R G Gordon. Atomic layer deposition of tin monosulfide thin films. *Advanced Energy Materials*, 1(6):1116–1125, 2011.

[88] P Sinsermsuksakul, L Sun, S W Lee, H H Park, S B Kim, C Yang, and R G Gordon. Overcoming efficiency limitations of SnS-based solar cells. *Advanced Energy Materials*, 4:1400496, 2014.

[89] M Steichen, R Djemour, L Gütay, J Guillot, S Siebentritt, and P J Dale. Direct synthesis of single-phase *p*-type SnS by electrodeposition from a dicyanamide ionic liquid at high temperature for thin film solar cells. *The Journal of Physical Chemistry C*, 117(9):4383–4393, 2013.

[90] V Steinmann, R Jaramillo, K Hartman, R Chakraborty, R E Brandt, J R Poindexter, Y S Lee, L Sun, A Polizzotti, H H Park, R G Gordon, and T Buonassisi. 3.88% efficient tin sulfide solar cells using congruent thermal evaporation. *Advanced Materials*, 26:74887492, 2014.

[91] V Stevanović, K Hartman, R Jaramillo, S Ramanathan, T Buonassisi, and P Graf. Variations of ionization potential and electron affinity as a function of surface orientation: The case of orthorhombic SnS. *Applied Physics Letters*, 104:211603, 2014.

[92] M Sugiyama, K Miyauchi, T Minemura, and H Nakanishi. Sulfurization growth of SnS films and fabrication of CdS/SnS heterojunction for solar cells. *Japanese Journal of Applied Physics*, 47(12):8723–8725, 2008.

[93] M Sugiyama, K Miyauchi, T Minemura, K Ohtsuka, K Noguchi, and H Nakanishi. Preparation of SnS films by sulfurization of Sn sheet. *Japanese Journal of Applied Physics*, 47:4494–4495, 2008.

[94] L Sun, R Haight, P Sinsermsuksakul, S B Kim, H H Park, and R G Gordon. Band alignment of SnS/Zn(O,S) heterojunctions in SnS thin film solar cells. *Applied Physics Letters*, 103:181904, 2013.

[95] U.S. Geological Survey. Commodity Statistics and Information. `http://minerals.usgs.gov/minerals/pubs/commodity/`. [Online; accessed 10 Nov 2011].

[96] U.S. Geological Survey. Mineral Commodity Summaries 2014. `http://minerals.usgs.gov/minerals/pubs/mcs/2014/mcs2014.pdf`. [Online; accessed 20 Oct 2014].

[97] K Takeuchi, M Ichimura, E Arai, and Y Yamazaki. SnS thin films fabricated by pulsed and normal electrochemical deposition. *Solar Energy Materials and Solar Cells*, 75:427–432, 2003.

[98] A Tanuševski and D Poelman. Optical and photoconductive properties of SnS thin films prepared by electron beam evaporation. *Solar Energy Materials and Solar Cells*, 80(3):297–303, 2003.

[99] G A Tritsaris, B D Malone, and E Kaxiras. Structural stability and electronic properties of low-index surfaces of SnS. *Journal of Applied Physics*, 115:173702, 2014.

[100] C G Van de Walle. First-principles calculations for defects and impurities: Applications to III-nitrides. *Journal of Applied Physics*, 95:3851, 2004.

[101] J Vidal, S Lany, M d'Avezac, A Zunger, A Zakutayev, J Francis, and J Tate. Band-structure, optical properties, and defect physics of the photovoltaic semiconductor SnS. *Applied Physics Letters*, 100:032104, 2012.

[102] J Werner, J Mattheis, and U Rau. Efficiency limitations of polycrystalline thin film solar cells: Case of Cu(In,Ga)Se_2. *Thin Solid Films*, 480-481:399–409, 2005.

[103] H Wiedermeier and F J Csillag. Equilibrium sublimation and thermodynamic properties of SnS. *Thermochemica Acta*, 34:257–265, 1979.

[104] Y Yan, R Noufi, and M Al-Jassim. Grain-boundary physics in polycrystalline $CuInSe_2$ revisited: Experiment and theory. *Physical Review Letters*, 2006.

[105] F G Yanuar, C Llinares, K Djessas, and G Masse. SnS thin films grown by close-spaced vapor transport. *Journal of Materials Science Letters*, 19:2135–2137, 2000.

[106] G H Yue, W Wang, L S Wang, X Wang, P X Yan, Y Chen, and D L Peng. The effect of anneal temperature on physical properties of SnS films. *Journal of Alloys and Compounds*, 474:445–449, 2009.

[107] Z Zainal, M Z Hussein, and A Ghazali. Cathodic electrodeposition of SnS thin films from aqueous solution. *Solar Energy Materials and Solar Cells*, 40:347–357, 1996.